

REPORT DOCUMENTATION PAGE					Form Approved OMB No. 0704-0188	
<p>The public reporting burden for this collection of information is estimated to average 1 hour per response, including the time for reviewing instructions, searching existing data sources, gathering and maintaining the data needed, and completing and reviewing the collection of information. Send comments regarding this burden estimate or any other aspect of this collection of information, including suggestions for reducing the burden, to Department of Defense, Washington Headquarters Services, Directorate for Information Operations and Reports (0704-0188), 1215 Jefferson Davis Highway, Suite 1204, Arlington, VA 22202-4302. Respondents should be aware that notwithstanding any other provision of law, no person shall be subject to any penalty for failing to comply with a collection of information if it does not display a currently valid OMB control number.</p> <p>PLEASE DO NOT RETURN YOUR FORM TO THE ABOVE ADDRESS.</p>						
1. REPORT DATE (DD-MM-YYYY) 19-10-2004		2. REPORT TYPE Final Report		3. DATES COVERED (From - To) Sep 2001-Oct 2004		
4. TITLE AND SUBTITLE Power Quality Study for the Proposed Integrated Power System			5a. CONTRACT NUMBER 5b. GRANT NUMBER N00014-01-1-1028 5c. PROGRAM ELEMENT NUMBER			
6. AUTHOR(S) Thomas H. Ortmeyer, Pragassen Pillay, Paul McGrath			5d. PROJECT NUMBER 5e. TASK NUMBER 5f. WORK UNIT NUMBER			
7. PERFORMING ORGANIZATION NAME(S) AND ADDRESS(ES) Clarkson University Office of Grants and Contracts Potsdam, NY 13699				8. PERFORMING ORGANIZATION REPORT NUMBER		
9. SPONSORING/MONITORING AGENCY NAME(S) AND ADDRESS(ES) Office of Naval Research Ballston Centre Tower One 800 North Quincy Street Arlington, VA 22217-5660				10. SPONSOR/MONITOR'S ACRONYM(S) ONR 11. SPONSOR/MONITOR'S REPORT NUMBER(S)		
12. DISTRIBUTION/AVAILABILITY STATEMENT No restrictions						
13. SUPPLEMENTARY NOTES Technical Representative: Terry Ericsen, Code ONR 334						
14. ABSTRACT The body of this report consists of seven chapters, each of which describes a principal topic of research into shipboard power quality issues. These topics include: Grounding study for bus connected high impedance grounded generators, the potential of a variable frequency, variable voltage generation system for improved efficiency and pulse loading capability, motor starting capability of fixed frequency inverters, the use of wavelet analysis to detect broken rotor bars in induction motors, motor surge characteristics, the use of wavelet analysis to monitor shipboard power system faults, and the investigation of partial discharge in motor windings. This work provides the framework for improvements in the quality and performance of shipboard power systems.						
15. SUBJECT TERMS Shipboard power systems, power quality						
16. SECURITY CLASSIFICATION OF: a. REPORT UU		17. LIMITATION OF ABSTRACT b. ABSTRACT UU		18. NUMBER OF PAGES c. THIS PAGE UU	19a. NAME OF RESPONSIBLE PERSON Thomas Ortmeyer 19b. TELEPHONE NUMBER (Include area code) (315) 268-6511	

DISTRIBUTION STATEMENT A
Approved for Public Release
Distribution Unlimited

BEST AVAILABLE COPY

Standard Form 298 (Rev. 8/98)
Prescribed by ANSI Std. Z39-18

**Power Quality Study
for the Proposed
Integrated Power System**

Thomas H. Ortmeyer, PI
Pragasen Pillay, Paul McGrath, Co-PI's
Clarkson University
Electrical and Computer Engineering Department
Potsdam, NY 13699-5720
(315)-268-6511
(315) 268-7600 (FAX)
ortmeyer@clarkson.edu

Grant #N00014-01-1-1028
ONR Program Officer: Terry S. Ericson
703-696-7741

Table of Contents

Page Number	Chapter	Title
3	1	Introduction
5	2	Generator Grounding Study
28	3	Novel electric drive with power-regenerating capability: modeling and simulation
43	4	Improved Motor Starting Capability of Three Phase UPS Inverters
51	5	The Application of Wavelets to the Detection of Broken Rotor Bars in Induction Machines
67	6	Measurement of Surge Propagation in Induction Machines
85	7	The Application Of Wavelets to Shipboard Power System Protection
103	8	Investigation of Partial Discharge in Motor Windings
111	9	Project Overview and Conclusions

Chapter 1

Introduction

1.1. Project Description

This is the final report for the research project “Power Quality Study for the Proposed Integrated Power System”, ONR project **N00014-01-1-1028**, performed at Clarkson University by Principal Investigators Thomas Ortmeyer, Pragasen Pillay, and Paul McGrath. The investigation involved a number of quality issues associated with shipboard power systems and their loads.

1.2. Key Findings

The body of this report consists of seven chapters, each of which describes a principal topic of research into shipboard power quality issues. These topics include:

- Grounding study for bus connected high impedance grounded generators
- The potential of a variable frequency, variable voltage generation system for improved efficiency and pulse loading capability
- Motor starting capability of fixed frequency inverters
- The use of wavelet analysis to detect broken rotor bars in induction motors
- Motor surge characteristics
- The use of wavelet analysis to monitor shipboard power system faults
- The investigation of partial discharge in motor windings

This work provides the framework for improvements in the quality and performance of shipboard power systems. The following paragraphs describe key results from this research.

The generator grounding study investigated the performance of two parallel connected generators in a high impedance grounding configuration. The study concluded that it is preferable to operate this system with both units grounded. While it is feasible to operate the system with only one of the units grounded, this leads to needless complexity in the system in order to accommodate both parallel and stand alone operation. It is shown that, with careful design, both units can be permanently grounded through high impedance, which can be in place regardless of the operating configuration of the system. It is further shown that this can be done without significant increase in the stator damage profile during ground faults. Finally, a scheme to determine if a ground fault is on a generator stator winding is proposed and simulations are included which indicate that this could be an effective approach to the problem.

The variable voltage variable frequency generator study investigates both the efficiency of the proposed propulsion scheme and its capability to serve pulse loads. The proposed scheme involves the direct

connection of synchronous generator to drive motor, without any electronic conversion. Ship service load is fed from this same bus, through an ac-dc boost converter. Thus propulsion power is not converted electronically, providing significant savings in space and cost, for the two power converters plus associated filtering. The study analyzed the efficiency, dynamic performance, and pulse load performance of this system, and concludes that this approach offers an attractive alternative to the present generation of electric propulsion systems.

The inverter study analyzes fixed frequency inverters feeding general system loads, such as would be found on shipboards served by dc distribution or advanced energy systems. An algorithm is proposed which would reduce inverter current requirements during induction motor starting by introducing voltage sags on the inverter bus during the motor acceleration. The study shows that the motor starting capability of these inverters can be significantly increased through this approach, providing the inverter to start larger motors without affecting the adjacent load fed by the inverter.

Wavelet analysis of power system events formed a significant part of this project. Variations on wavelet analysis techniques were used in studies involving the detection of broken rotor bars in induction motors, power system fault detection, and partial discharge detection. Wavelet analysis has proven to hold promise in each of these areas, as described in Chapters 5, 6, and 8.

Chapter 7 presents a contribution to the measurement of motor parameters for surge propagation studies. The study includes both model development and detailed measurements of winding inductance and capacitance in order to build a model which will provide insight into winding performance of motors fed by inverters, particularly those which include a significant cable run between the inverter and motor.

The following chapters describe these results in detail. They also provide reference to papers and theses which resulted from this work, and provide still additional details on the projects.

Chapter 2

Generator Grounding Study

2.1. Introduction

Most power systems in operation have unit-connected generators, but lately there has been a shift toward direct connected generation, particularly in stand alone systems and when distributed generation is employed. The grounding of unit-connected generators is widely studied and well documented, and the high impedance grounding strategy generally employed for unit connected generators is effective and widely used.

In the case of unit connected generators, however, the situation is much different, in that it is only recently being studied, the impact of various grounding strategies on the generator is not widely understood, and no there is no standard approach to the issue. In purely stand-alone systems, the designer may have the option of employing an ungrounded or high impedance grounding system. In cases involving distributed generation (DG), on the other hand, the generator may be directly connected to an existing solidly grounded bus, and the unit is required to supply the bus both in the grid connected and stand-alone mode of operation.

Several issues arise in these cases. First, the phase voltages present on the bus during unbalanced faults are of concern. Secondly, the generator currents during a fault are a major concern. Finally, the ability of a protection scheme to identify the location of a ground fault on the bus is of primary importance.

In this study, the ground fault performance of direct connected generators is analyzed. The generators are considered to be high impedance grounded in order to limit the stator iron damage during a fault. A variety of configurations for this grounding are considered. Also, the study considers both stand-alone operation where a pair of generators are directly connected to an ungrounded bus, and grid connected, where the generators are connected to a bus fed by a step down transformer with a variety of grounding configurations. The study considers phase voltages, generators currents and stator damage, and fault sensing.

As synchronous generators form the principal source of electric energy in power systems, the power system stability problem is largely one of keeping interconnected synchronous machines in synchronism. Therefore, an understanding of their characteristics and accurate modeling of their dynamic performance are of fundamental importance to the power industry.

Stable operation also depends on the ability to continuously match the electrical output of generating units to the electrical load on the system. While induction motor is used in a wide variety of applications as a means of converting electric power to mechanical work. Consequently, dynamic modeling and characteristics of the induction motors have important influence on system stability.

Modeling and analysis of the AC machines (generators and motors) has been covered in a number of textbooks. [2.11]. One standard method of modeling a synchronous machine is as follows

1. Calculate stator and rotor flux linkages (refer values to stator and in per unit system)
2. Calculate mathematical equations for voltage and torque
3. Transfer voltage and torque equations into d-q frame
4. Machine controllers design

MATLAB/SIMULINK, PSPICE, EMTP and other commercial software products are available for assisting dynamic machine modeling design.

2.4. System Grounding

This section gives an insight into the system grounding principles, and includes the different grounding strategies used. Grounding of generators has been studied for a long time; an attempt is made towards finding the relation between system grounding strategies with generator stator damage. The grounding theory is well documented in [2.8, 2.13].

System grounding, or the intentional connection of a phase or neutral conductor to earth, is for controlling the voltage to earth, or ground, within predictable limits. It also provides for a flow of current that will allow detection of an unwanted connection between system conductors and ground and which may instigate operation of automatic devices to remove the source of voltage from conductors with such undesired connections to ground. The National Electric Code, (NEC) prescribes certain system grounding connections that must be made to comply with the code. The control of voltage to ground limits the voltage stress on the insulation of conductors so that insulation performance can more readily be predicted. The control of voltage also allows reduction of shock hazard to persons who might come in contact with live conductors.

2.5 Factors Influencing the Choice of Grounded or Ungrounded System

2.5.A Service Continuity For many number of years a large number of industrial distribution plants have been operated ungrounded at one or more voltage levels. This is generally done to obtain a greater degree of service continuity. The fact that any contact occurring between one phase of the system and the ground is unlikely to cause an immediate outage to any load may represent an advantage in many plants, varying in its importance according to the type of the plant.

Grounded systems are designed so that circuit protective devices will operate to remove any faulty circuit from the system regardless of the fault. A phase to ground fault generally results in the immediate isolation of the faulted circuit.

2.5.B Multiple Faults to Ground While a ground fault on one phase of an ungrounded system generally does not cause a service interruption, the occurrence of a second fault on a different phase before the first fault is cleared does result in an outage. If both the faults are on the same feeder, the feeder is opened and if the fault is on a different feeder both the feeders have to be de-energized. The longer a ground fault is allowed to remain on an ungrounded system, the greater the likelihood of a second fault occurring on another phase thereby resulting in an outage.

2.5.C Abnormal Voltage Hazards The possible over-voltages on the ungrounded system may cause more frequent failures of equipment than if the system were grounded. A fault on one phase of an ungrounded system places a sustained increased voltage on the insulation of ungrounded phases in a three-phase system. As this voltage is about 1.73 times the normal voltage, the stress on the insulation also increases proportionately. [2.5] As the ungrounded systems are designed for the possible increased in voltage level, the cost of cables increases.

2.6 Methods of Generator System Neutral Grounding [2.6, 2.8]

Most grounded systems employ some method of grounding the system neutral at one or more points. These methods can be divided into two general categories: Solid grounding and impedance grounding. Impedance grounding may be further divided into several subcategories: Reactance grounding, resistance grounding and ground-fault-neutralizer grounding. Each method, as named, refers to the nature of the external circuit from system neutral to ground rather than to the degree of grounding.

2.6.A Ungrounded Systems (no galvanic ground) Electrical power systems, which are operated with no intentional ground connection to the system conductors, are generally described as ungrounded. In reality, these systems are grounded through the system capacitance to ground.

Two principal advantages are attributed to ungrounded systems.

- The first ground fault on a system causes only a small ground current to flow, so the system may be operated with a ground fault present, improving system continuity.
- No expenditures are required for grounding equipment or grounded system conductors.

Numerous advantages are attributed to grounded systems,

- Greater safety,
- Freedom from excessive system over-voltages that can occur on ungrounded systems, including overvoltages due to multiple restrikes of a fault.
- Easier detection and location of ground faults when they occur.

Grounded systems are now the predominant choice. When an ungrounded system is chosen, a ground detection scheme should be applied to the system, this is done in order to provide for the relaying needs in case of ground faults.

2.6.B Resistance Grounding In resistance grounding, the neutral is connected to ground through one or more resistors. In this method, with the resistor values normally used, and except for transient over-voltages, the line-to-ground voltages that exist during a line-to-ground fault are nearly the same as those for an ungrounded system. A system properly grounded by resistance is not subject to destructive transient over-voltages.

The reasons for limiting the current by resistance grounding may be one or more of the following.

- To reduce burning and melting effects in faulted electric equipment, such as switchgear, transformers, cables, and rotating machines.
- To reduce mechanical stresses in circuits and apparatus carrying fault currents.
- To reduce electric-shock hazards to personnel caused by stray ground-fault currents in the ground return path.
- To reduce the arc blast or flash hazard to personnel who may have accidentally caused or who happen to be in close proximity to the ground fault.
- To reduce the momentary line-voltage dip occasioned by the occurrence and clearing of a ground fault.
- To secure control of transient over-voltages while at the same time avoiding the shutdown of a faulty circuit on the occurrence of the first ground fault (high-resistance grounding).

Resistance grounding may be either of two classes,

- 1) High resistance
- 2) Low resistance

High-resistance grounding typically uses ground-fault current levels of 10 Amperes or less, although some specialized systems at voltages in the 15 kV class may have higher ground-fault current levels. Low-resistance grounding typically uses ground-fault current levels of at least 100 Amperes, with currents in the 200–1000 A or higher being common.

2.6.C Reactance Grounding The term reactance grounding describes the case in which a reactor is connected between the system neutral and ground. Since the ground-fault that may flow in a reactance-grounded system is a function of the neutral reactance, the magnitude of the ground-fault current is often used as a criterion for describing the degree of grounding. In a reactance-grounded system, the available ground-fault current should be at least 25% and preferably 60% of the three-phase fault current to prevent serious transient over-voltages this is provided by having ($X_0 \leq 10X_1$). This is considerably higher than the level of fault current desirable in a resistance-grounded system, and therefore reactance grounding is usually not considered an alternative to resistance grounding.

2.6.D Ground-Fault Neutralizer (Resonant Grounding) A ground-fault neutralizer is a reactor connected between the neutral of a system and ground and having a specially selected, relatively high value of reactance. The reactance is tuned to the system charging current so that the resulting ground fault current is resistive and of a low magnitude. This current is in phase with the line-to-neutral voltage, so that current zero and voltage zero occur simultaneously. This method of grounding is used primarily on systems above 15 kV, consisting largely of overhead transmission or distribution lines. Since systems of such construction are rarely used in industrial or commercial power systems, the ground-fault neutralizer finds little application in these systems.

2.6.E Solid Grounding Solid grounding refers to the connection of the neutral of a generator, power transformer, or grounding transformer directly to the station ground or to the earth.

Because the reactance of the grounded generator or transformer is in series with the neutral circuit, a solid ground connection does not provide a zero-impedance neutral circuit, which means that ideally there cannot be a ground with zero impedance but the ground path will have the reactances of the generator and the transformer. If the reactance of the system zero-sequence circuit is too great with respect to the system positive-sequence reactance, the objectives sought in grounding, principally freedom from transient over-voltages may not be possible.

2.6.F Choice of Grounding: The method of grounding chosen in this research is that of High Resistance neutral grounding. The reasons being as follows:

- It limits the fault current to a fraction of load current
- It can be very effectively applied to drive systems as studied [2.10].
- This configuration is suitable in detection of faults [2.10].
- This incorporates the advantages of both an ungrounded system and a grounded system, namely service continuity and fault detection. [2.8, 2.12]

2.7 Characteristics of High Resistance Grounded Systems

The characteristics of this system are as follows

1. For a no fault case, the system neutral is held at ground potential. Assuming the same phase-to-ground distributed capacitances, the current returning through the neutral resistor is

$$I_a + I_b + I_c = 0$$

2. In a balanced symmetrical three-phase system, the phase capacitances to ground are a summation of the capacitances to ground cables, buses, and transformers and surge arresters. The capacitive charging current is limited in the range of 3-25 A, in most of the medium and low voltage systems. [2.1, 2.13]

3. On the occurrence of a ground fault, the voltage to ground on the unfaulted phase rises to line-to-line voltage imposing insulation stresses on cables and motors. The line-to-line phases do not change in magnitude and are balanced.

4. The current through the grounding resistor I_r , should be equal to greater than the distributed capacitive current to prevent any transient over-voltages [2.1, 2.8, 2.13].

For the above reasons the popular choice of grounding for the generator is of "High Resistance Grounding". This can be achieved by the insertion of a resistance between the generator neutral and the ground. In many cases distribution transformer and a loading resistor also does this task. The primary of the distribution transformer is connected between the generator neutral and the ground; the loading resistor is connected across the secondary winding of the transformer. This has the effects of reducing its insulation requirements. [2.1]

2.7.A Generator Stator Ground Fault Protection and Generator Relaying The method of grounding affects the degree of protection afforded by differential relays, the higher the grounding impedance, the less the fault current magnitude and more difficult it is to detect high impedance faults. With the high impedance grounding, the differential relays will not respond to single- phase-to-ground faults [2.13, 2.16]. A separate relay in the grounded neutral will provide sensitive protection, since it can be set without regard to the load current. This has to be set with a time delay such that it will not operate for faults beyond the generator

In the scheme shown above the protection provided for the winding is 95% and this is known as the 95% scheme of protection. As shown a 59G low pickup over voltage relay is used for the protection purposes. This scheme has good sensitivity for ground faults. The voltage appearing across the neutral is dependent on the location of the ground fault and more sensitive the ground relay the more percentage of the winding is protected.

The neutral to ground fault goes undetected by this scheme and another device has to be used for this purpose. For detecting the neutral to ground faults and thereby offering a 100% winding protection a third harmonic relay or a neutral relay 59N can be used in parallel with the 59G. [2.13]

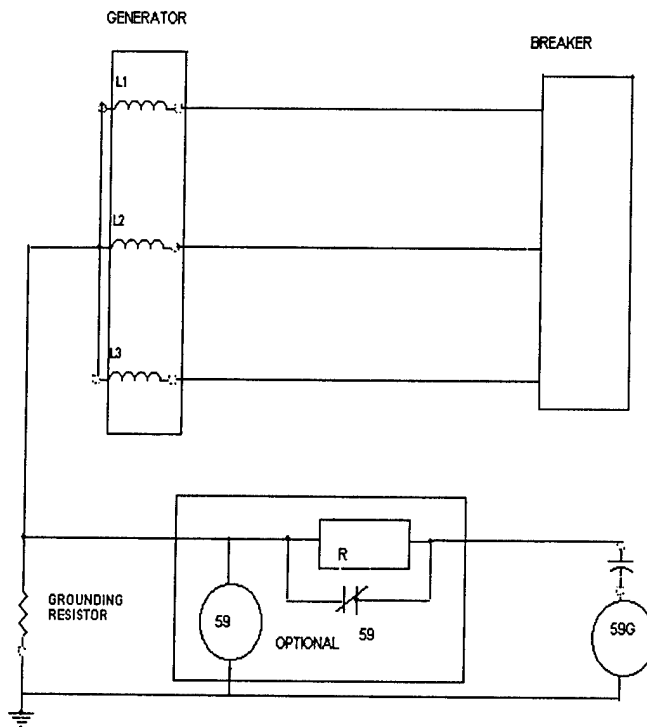


Figure 2.2 Schematic of a Generator with high resistance ground for ground fault protection

2.7.B Generator Stator Damage The grounding strategy of the generator plays an important part in the damage sustained by the generator during the fault. This has been observed in a number of bus connected industrial generators that have experienced a severe damage due to stator ground faults. However, as of now the units that are being used for distributed generation are also increasing in size and rating, therefore the problem of stator iron damage is being seen on these units too.

In most cases, the generators have to be returned to the manufacturers for extensive repairs to the winding. Since the markets have become more competitive this "down time" of the generator is not just the cost of repairs, it also includes the loss of production for the "down-time".

It is known that the damage is initiated by a ground fault and is caused by the abnormal flow of current. This current can be limited by the use of resistance grounding of the generators.

As stated in [2.6, 2.7] this is true in the case of unit connected generators [2.6] and also as it will be seen later in the case of stand alone DG these references do not mention the effect of grounding the utility transformer on the damage sustained by the generator when operating in parallel with the grid. In addition, these references cover the aspects of generators operating with a solidly grounded neutral. The indices of

damage with respect to the current contribution from the utility source can change with respect to the type of grounding used.

For the estimation of damage indices, only the faults occurring at the stator terminals are studied and the faults at the neutral and within the stator windings are not considered.

This is justified because for a inter stator fault the magnitude of the fault current will be lesser than for the fault at the terminal of the generator.

The technology of stator ground fault has improved and can detect and isolate faults to the neutral end of the winding [2.6]. It is reasonable to assume that the fault will be detected and tripping will be triggered with no intentional time delay. It has also known that the damage to the stator is proportional to the energy [2.6, 2.7, 2.9].

$$\text{Damage} \propto \text{energy} = \int i^k dt \quad [2.1]$$

The value of k is taken as 2 for resistive heating. It should also be noted that the above equation yields a number that can be assigned the units of energy but as the interest, here is the damage and the constant of proportionality is not of importance.

2.8 System Configuration

Both stand-alone and grid connected generator systems are studied. For both the types of distribution systems two configurations are studied. They are as follows.

- 1) Configuration 1: One of the generators high resistance grounded and the other left ungrounded.
- 2) Configuration 2: Both the generators high resistance grounded.

For the grid connected distributed generation, a utility transformer will be operating in parallel with the above generator systems.

These distributed generation systems provide us with reasonably good and complex systems to study and very closely represent distributed generation systems operating in the real world. In addition, using two generators gives us an option of increased reliability if one generator is disconnected in the case of a fault. In the following study the stand alone generation is studied first.

2.8.A. Configuration 1: Only One Generator Grounded

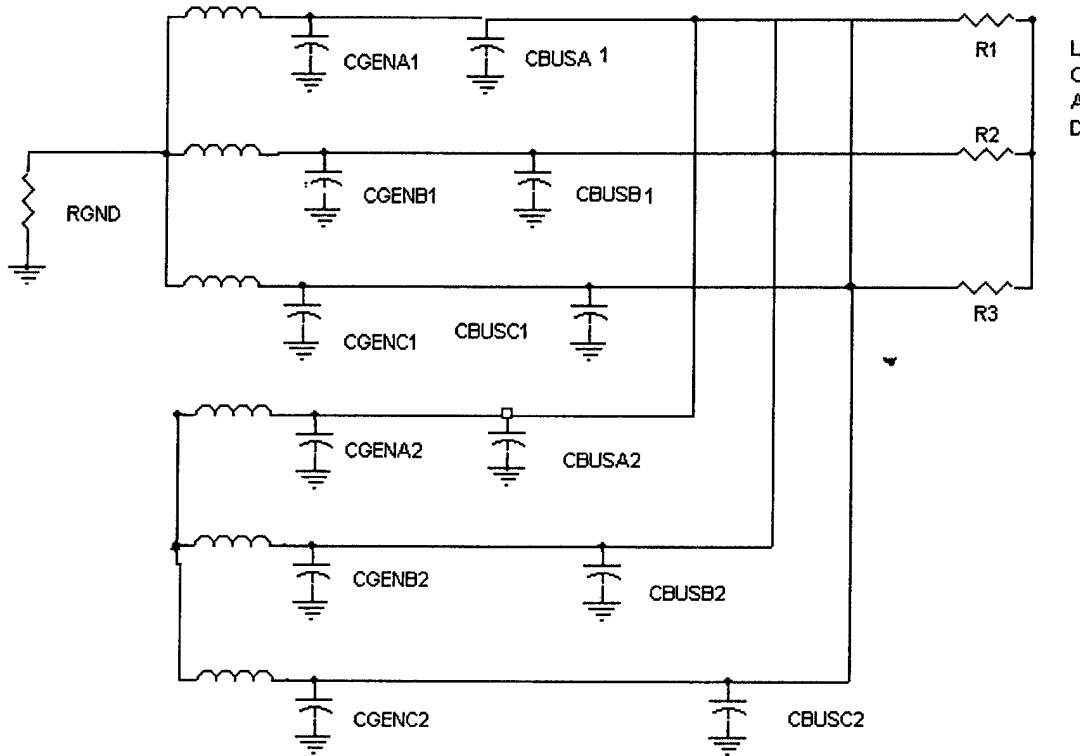


Figure 2.3. Schematic of Configuration 1

As shown in Figure 2.3 in this study both the generators are grounded. The various components are as follows:

CGEN1, CGENB1 and CGENC1 are the stator inter-winding and the generator surge capacitances for the *generator 1*.

CBUSA1, CBUSB1 and CBUSC1 are the bus to ground capacitances of the cables connecting the *generator 1* to the bus.

CGEN2, CGENB2 and CGEN2 are the stator inter-winding and the generator surge capacitances for the *generator 2*.

CBUSA2, CBUSB2 and CBUSC2 are the bus to ground capacitances of the cables connecting the *generator 2* to the bus.

R1, R2 and *R3* comprises the load (resistive model)

RGND – the grounding resistor for the first generator

2.8.B. Configuration: 2 Both Generators Grounded

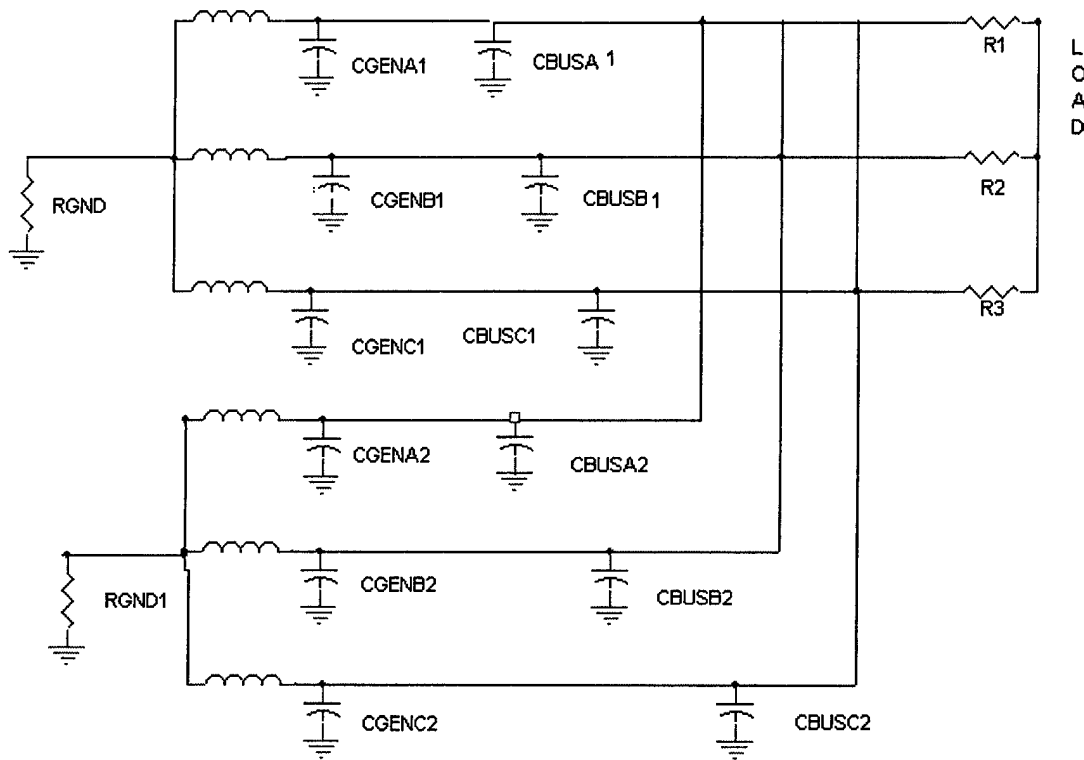


Figure 2.4 Schematic of the Configuration 2

In this study, both the generators are grounded. As seen from Figure 2.4, the generator 1 is grounded with the grounding resistor $RGND$ and the generator2 is grounded with resistor $RGND1$.

2.8.C Grid Connected Distributed Generation Configurations The above configurations are also studied when connected with a utility transformer in parallel. The utility transformer is a Delta –Wye connected transformer. Here the configuration 2 is shown.

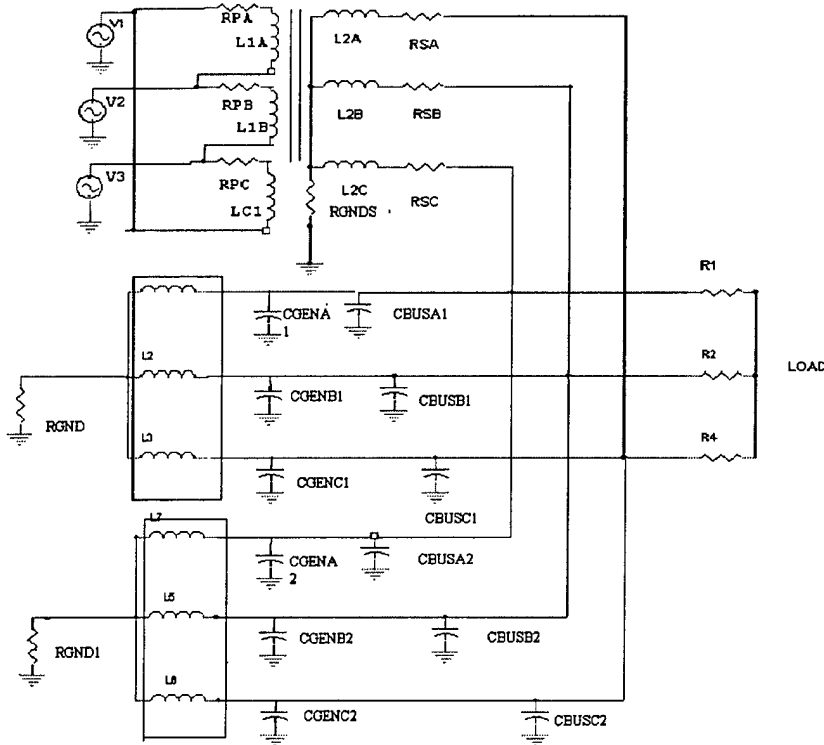


Figure 2.5 Grid Connected Distributed Generation set up for configuration 2

2.8.D Calculation of the value of the grounding resistor 2.4, 2 Ideally, the neutral resistance is to be as large as possible to minimize the line to fault ground current. However, the capacitive charging currents of the electrical system connected to the generator dictate the maximum resistance size. To avoid the build up of destructive over-voltage caused by re-striking phenomena during single phase –to-ground fault, the resistive fault current shall be larger than the capacitive charging current. [2.1,5, 2.8]. Therefore, the equivalent neutral grounding resistance R_N shall be less than the system relevant capacitive reactance. In a three-phase system(*R*, *Y* and *B*) grounded at the neutral, the total charging current

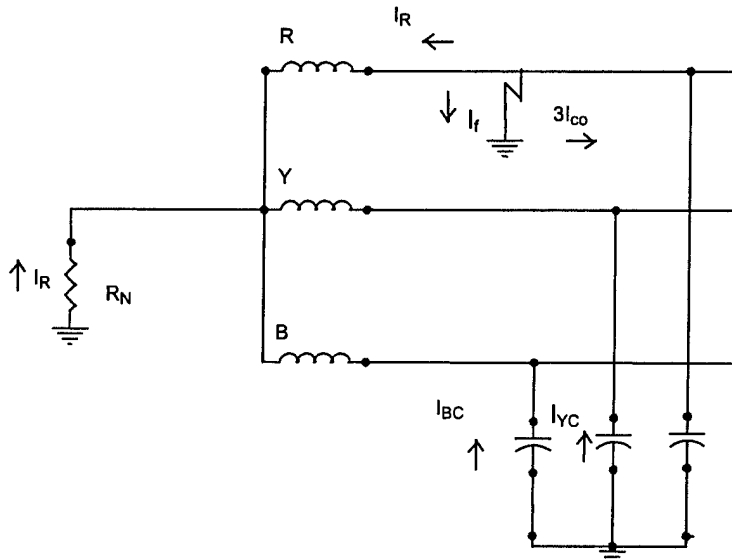


Figure 2.6 Fault current distribution

$$\text{Charging current} = |I_{BC} + I_{YC}| = \left| \frac{E_{LL}}{X_{CO}} + \frac{E_{LG} \angle 120}{X_{CO}} \right| \quad [2.2]$$

$$= \sqrt{3} \frac{E_{LL}}{X_{CO}} = 3 \frac{E_{LG}}{X_{CO}} = 3I_{CO} \quad [2.3]$$

where

I_{BC} *B*-phase capacitive charging current;

I_{YC} *Y*-phase capacitive charging current;

E_{LL} line-to-line voltage;

E_{LG} line-to-ground voltage;

X_{CO} line-to-ground charging capacitive reactance;

I_{CO} line-to-ground charging current

$$\text{As} \quad I_R > 3I_{CO} \quad [2.4]$$

$$I_R = \frac{E_{LN}}{R} \quad [2.5]$$

$$\text{and} \quad 3I_{CO} = \frac{E_{LN}}{\frac{X_{CO}}{3}} \quad [2.6]$$

Hence, it follows that

$$R_N < \frac{X_{CO}}{3} \quad [2.7]$$

To calculate X_{CO} , the charging capacitances should be identified these include: the stator inter-winding capacitance, generator surge capacitor and the cable capacitance. The generator surge capacitance and the stator inter-winding capacitance are represented as a single lumped parameter.

Based on the above principles the grounding resistor for a single generator was designed taking the generator capacitance per phase as 0.49uF and the bus capacitance as 0.03uF. This results in a capacitive reactance of 5101 and as the grounding resistor's maximum value has to be a third of the capacitive reactance it is calculated as 1700 ohms.

A value of 1400 ohms was chosen for the purpose grounding of the generators when it is only one of the generator is grounded. When both the generators are to be grounded a grounding resistance of 700 ohms each is used to ground the generators as this will tend to keep the fault current lower.

Initially this value of the grounding resistor was tested on a stand alone two-generator system. This was done with a single line to ground fault. The results were analyzed for the charging current. This result is presented in Figure 2.7.

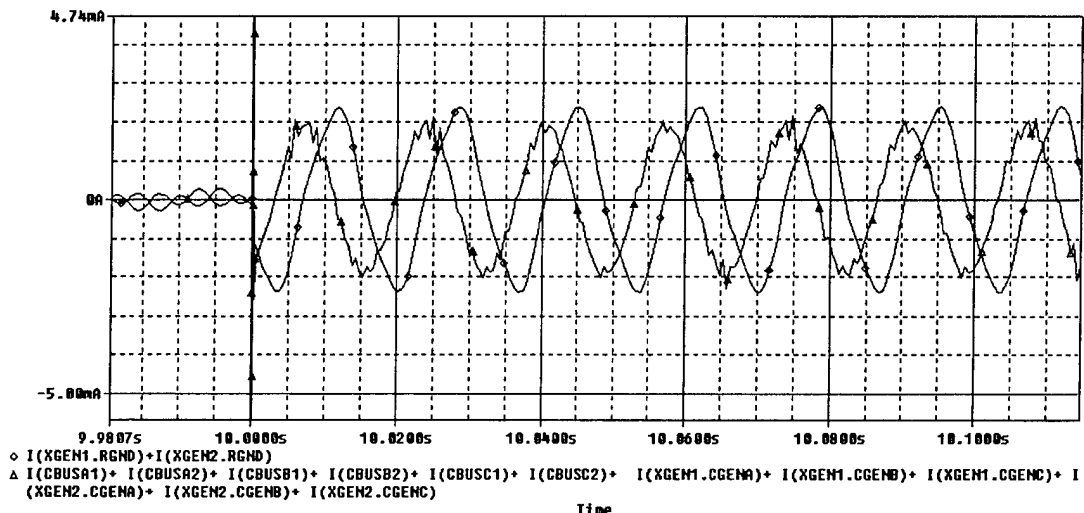


Figure 2.7 Capacitive Charging Currents and System Ground Current for a single phase to ground fault

As seen from the figure the resistive current is greater than the system capacitive current, which is an indication that the grounding has been designed correctly, this is an essential requirement of the high-resistance grounded system.

For the configuration 1 it is all right if the grounding resistor is 1400 ohms, it accounts for the full system capacitance. This value can also be used for grounding of generator 2 in configuration 2. This will cause the capacitance to be overcompensated and hence it will allow a higher value of fault current. Hence, to avoid this when configuration 2 is simulated both the generators are grounded using resistance of 2800 ohms.

2.9 Simulation Results

This section provides simulation results for the single phase to ground faults on the the systems under consideration. The parameters for the capacitances and the inductances of the line are givenin Table 2.1.

Table 2.1 Critical System Parameters

CGENA, CGENB and CGENC=0.49UF	LBUS=0.007 H
CBUS=0.03UF	
RGND CALCULATED= 1700 ohms	

2.9.A. Fault Studies on Configuration 1: One generator grounded The fault is set to occur on the bus on 'phase-a', which corresponds to the voltage V_1 the voltages of phases 'b' and 'c' are V_2 and V_3 respectively. The fault is initiated at 10 seconds, which gives sufficient time for the system to come to steady state. As seen from Figure 2.7 the plot the voltage of the faulted phase goes to '0' at the incidence of the fault and the voltages of the healthy phases rise to 1.732 or $\sqrt{3}$ times the normal value.

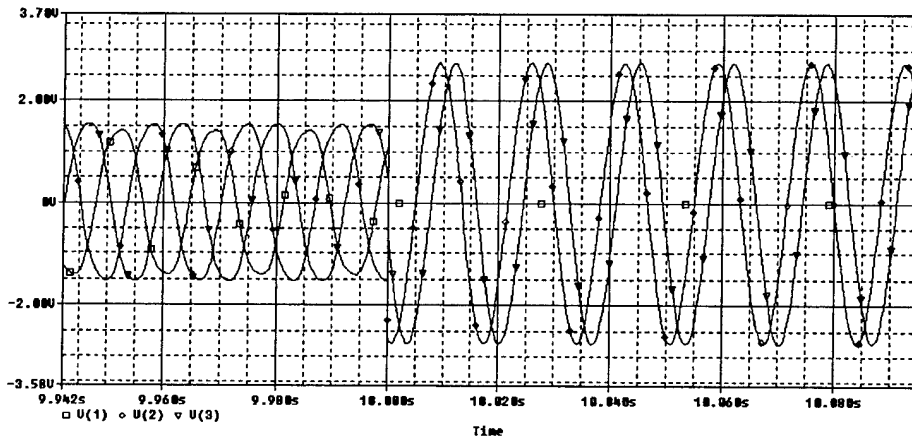


Figure 2.7 Terminal Voltages for a bus fault

Similarly, Figure 2.8 shows the neutral voltage rising to the predicted line-neutral voltage level. There are minimal transient effects on either the neutral or phase voltages.

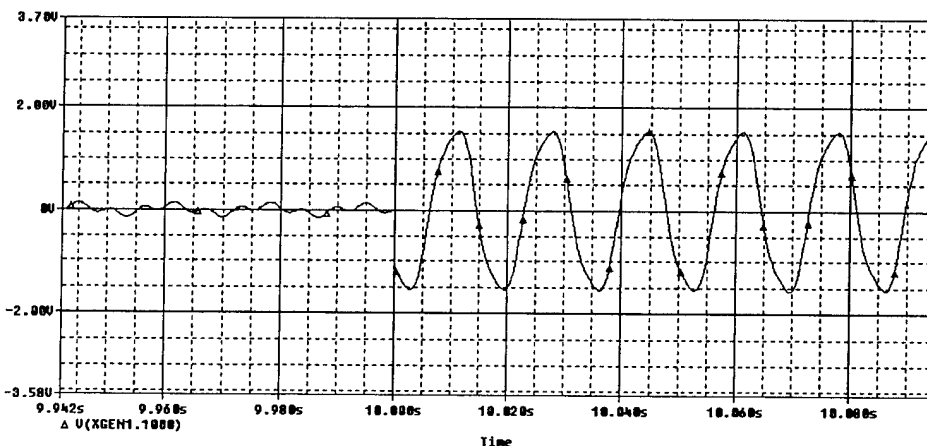


Figure 2.8 Voltage across the neutral grounding resistor

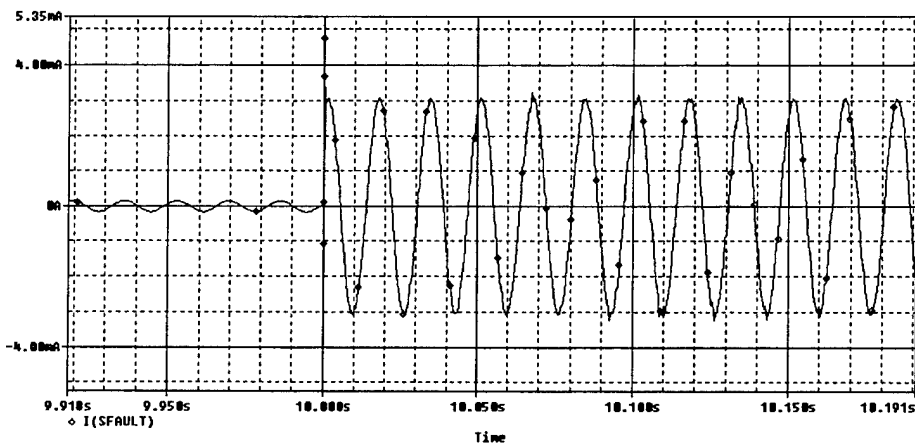


Figure 2.9 Fault Current for a bus fault.

The plot of fault current, Figure 2.9, shows that the peak value of the fault current is 0.0307 p.u., which corresponds to an actual value of 9.8 amps. This is an acceptable value of the fault current when high resistance grounding of a generator is used.

2.9.B Fault studies on Configuration 2: Both generators grounded With both generators grounded, the single phase to ground fault is virtually identical to the previous case. The grounding resistors were chosen to obtain the same fault current as with a single generator grounded, and this level was achieved.

2.10 Location of Faults Based on the Power Signals

The previous section has shown that a single phase to ground fault on the high impedance grounded system causes significant changes in the phase to ground and neutral to ground voltages. These are readily detected. It is generally difficult, however, to determine the location of the ground fault.

Power flow direction is one parameter that is readily measured. The use of power flow direction to determine the location of single phase to ground faults is investigated in this section. If the currents flowing out through the terminals of the wye connected generator are I_a , I_b and I_c and the voltage at the neutral of the generator is V_{gnd} ; then the faults can be isolated on the basis of the power function $P(t)$ where $P(t)$ is defined as

$$P(t) = (I_a + I_b + I_c) * V_{gnd} \quad [2.8]$$

This measurement can be readily made. Where practical, the summation of the generator terminal current could be performed with a single window type current transformer, which would provide a highly accurate measure of the summation of these currents. Where this is not practical due to physical or reliability

constraints, the current transformer secondary currents can be added to obtain the sum. As the current transformer duty is low in this case, sufficient accuracy should be obtainable.

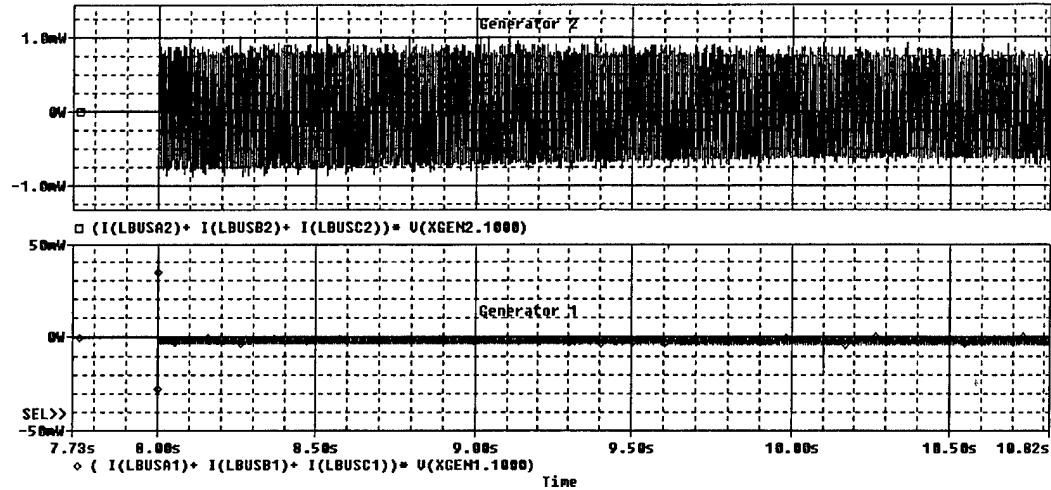


Figure 2.10 Power Function Plot for a bus fault, one generator grounded.

2.10.A. Configuration 1: Generator 1 grounded. Figure 2.10 shows a plot of the instantaneous power for both generator 1 and 2, for a bus fault. Recall that in this configuration, the generator 1 neutral is connected to a grounding resistor, while the generator 2 neutral is floating. As seen from the figure we see that for a bus fault the average power sensed at generator 1 is negative and the average power sensed at generator 2 is '0'.

Figure 2.11 shows a similar fault located on the generator 1 terminals, within it's zone of protection. In this case, both generators 1 and 2 show no average power. This is expected, as the zero sequence power flow in this case is entirely within the generator 1 zone of protection.

The situation for a generator 2 terminal fault is shown in Figure 2.13. In this case, the zero sequence power flows from the fault point, out the generator 2 terminals (resulting in a positive power flow on generator 2), and in the generator 1 terminals to the grounding resistor (or a negative power flow out of generator 1).

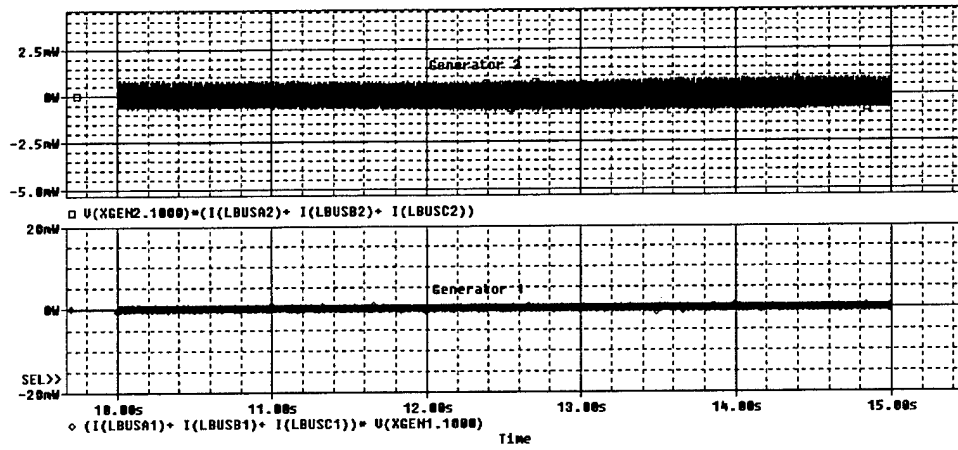


Figure 2.11 Power Function Plot for Generator 1 terminal fault.

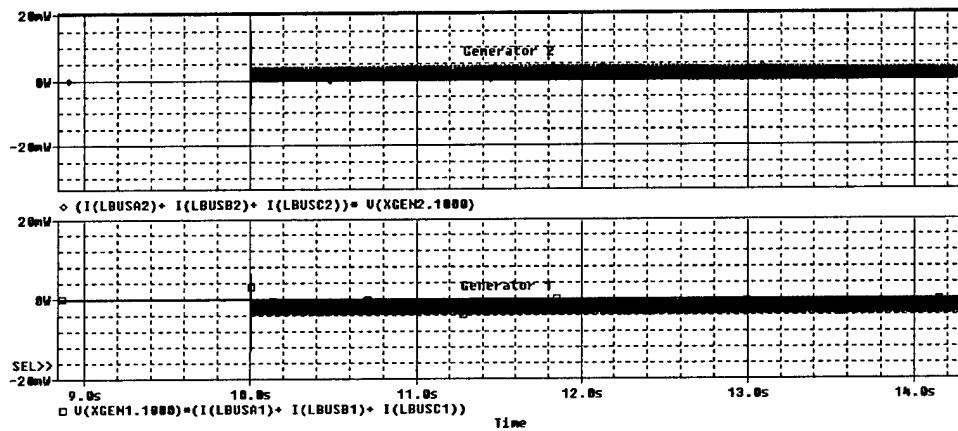


Figure 2.12 Power Function Plot for Generator 2 terminal fault.

Table 2.2 Summary for power function plots for stand-alone DG configuration 1.

Fault Location	Average Power at Gen 1	Average Power at Gen. 2
Bus fault	Negative	Zero
Generator 1	Zero	Zero
Generator 2	Negative	Positive

2.10.B. Configuration 2: Both generators grounded. A similar logic applies when both generators are grounded. The sensing algorithm senses zero sequence power flow.

Table 2.3 Summary of the zero sequence power flow for single phase to ground faults when both generators are grounded.

Fault Location	Average Zero Sequence Power flow OUT OF Generator 1	Average Zero Sequence Power flow OUT OF Generator 2
Bus fault	Negative	Negative
Generator 1	Positive	Negative
Generator 2	Negative	Positive

This flow is generated at the point of the fault, and flows toward the grounding resistor(s). Table 2.3 shows that for a fault outside of a given generator zone of protection, power will flow toward the grounding resistors in all cases, providing a ready method of detecting the presence of a fault within a given generator zone of protection.

2.11. Estimation of Stator Damage due to Single Phase to Ground Faults

Generator damage can result during winding faults, depending on the magnitude and duration of the fault current. In particular, it is important to avoid or minimize damage to the stator core following an insulation failure on the winding. the fault current.

All the faults are initiated on the terminals of the generator 1 in this study. The circuit breaker can be modeled as a switch that has a low resistance when it is closed, about 0.01 p.u. This is small when compared to the resistance of the load and therefore does not effect the operation of the system in any way. When the switch is opened it has a resistance which is very high in our case it has a resistance of 1000 p.u. The circuit breaker operation is simulated after the fault has been on the system for 5-6 cycles as this is approximately the time, which circuit breakers operate in most power systems. This time includes the time to sense the fault and the time for the operation of the breaker [2.12]. Equation 2.1 describes the level damage which can be expected from a given fault. In cases where the fault transient small, Eq. 2.1 can be evalated as the product I^2t . Figure 2.13 shows the damage parameter for configuration 1, which involves one generator being high impedance grounded and the second one being ungrounded. The fault is initiated on the system and the

faulted generator is disconnected after the fault is on the system for 6 cycles. This I^2t level is consistent with unit connected generators which employ a high impedance grounding system, and is known to minimize the level of stator damage.

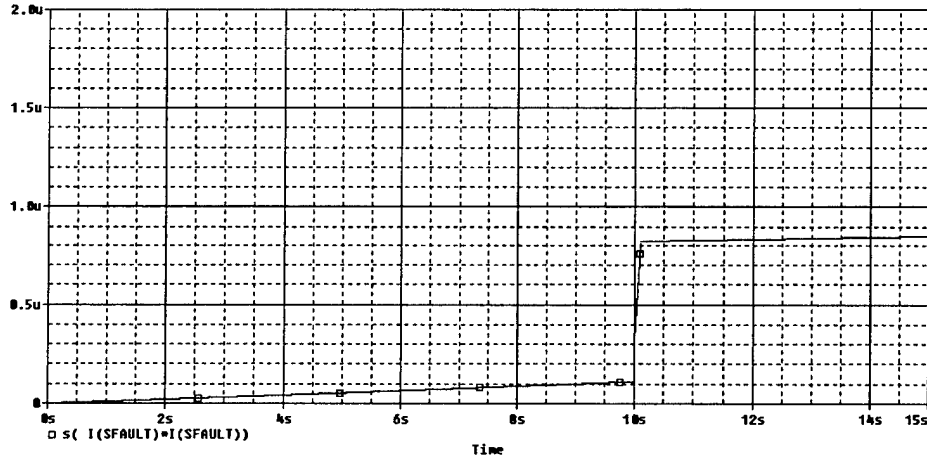


Figure 2.13 Plot of Damage Configuration 1 without the utility source.

Figure 2.14 shows the same fault conditions for the configuration 2, where both generators employ a high impedance grounding system:

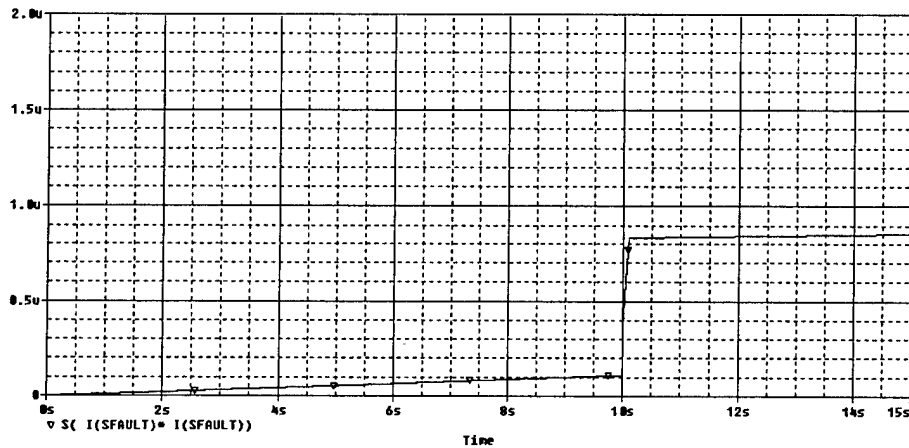


Figure 2.14 Plot of damage for configuration 2 without the utility source.

The damage index for both the configurations is identical at $0.865e-6$ p.u, from this we can draw two conclusions: that if we are high resistance grounding the generators and they are feeding a load on a stand alone basis, the damage associated with them is the same and it does not depend on the number of grounds on the system, it was said in [2.7] that the damage increases with the number of grounds on the system, but this is shown to be a design feature.

2.13 Conclusions

This study explores high impedance grounding systems for a pair of direct connected generators. Two configurations are considered—a grounding resistor used on a single generator neutral, with the other neutral floating, and a grounding resistor deployed on both generator neutrals. The study suggests that both options are technically feasible.

There are a number of practical reasons that employing a high impedance ground on both generators is preferable, however. The power system must be built to function both with the generators paralleled and the generators operating separately (or with one generator supplying the entire load). This dictates that a grounding resistor must be present on both generator neutrals. Operating in configuration 1, with only one generator grounded, would require that the other generator neutral resistor be switched out during parallel operation.

When the system is designed so that both generators have a neutral resistor when operating in parallel, there is no need to provide for switching the generator neutral resistor. In this case, the grounding resistor for each generator can be sized appropriately with respect to the stray capacitance of that unit.

Secondly, fault sensing is more straightforward when both generators are grounded. Table 2.3 shows that zero sequence power flows into the generator terminals only when the fault is within that generators zone of protection. Table 2.2 shows a more complex situation for Configuration 1.

Finally, it is believed that the advantages of having a suitable high impedance grounding system on every generator will become more pronounced in cases where more than 2 generators are directly connected to a common bus. With proper design of the grounding resistors, this need not lead to increased stator damage.

REFERENCES:

- [2.1] Considerations for Generator Ground Fault Protection in Midsize Cogeneration Plants, Rasheek M. Rifaat, IEEE Transactions on Industry Applications, Vol.33.No3, pp. May/June 1997.Page(s) 628-634.
- [2.2] The Effects of Very High Resistance Grounding on the Selectivity of Ground Fault relaying in High Voltage Longwall Power Systems, Thomas Novak IEEE Transactions on Industry Applications, Vol.37.No2, March/April 2001, Page(s) 398-406.
- [2.3] Analysis of Very High Resistance Grounding in High Voltage Longwall Power Systems, Thomas Novak IEEE Transactions on Industry Applications Vol.37.No1, January/February 2001.Page(s) 104-111
- [2.4] High Resistance Grounding of Low-Voltage Systems: A Standard for the Petroleum and Chemical Industry, John P. Nelson and Pankaj K. Sen., IEEE Transactions on Industry Applications Vol.35.No4, July/August 1999, Page(s) 941-648.

- [2.5] Grounding Concerns in Cogeneration Frank A. Woodbury, IEEE Transactions on Industry Applications Vol.IA-21.No6, pp. 1523-1532, November/December 1985.
- [2.6] The Impact of Generator Grounding Practices on Generator Fault Damage, Louie J. Powell, IEEE Transactions on Industry Applications Vol.34, No5, September/October 1998. Page(s) 923-927.
- [2.7] Stator Fault Damage Considerations for Generators on Solidly Grounded Systems, Louie J. Powell, IEEE Transactions on Industry Applications Vol.37, No1, January/February 2001. Page(s) 218-222.
- [2.8] IEEE Recommended Practice For Grounding of Industrial and Commercial Power Systems IEEE Standard 142-1991 (The Green Book)

Chapter 3

Novel electric drive with power-regenerating capability: modeling and simulation

3.1 Introduction.

Recently, electric drives play an important role in marine, rail and other transportation systems. There are many advantages of using electric propulsion in seagoing vessel, as compared with the traditional shaft driven propellers. A great amount of work has already been done not only concerning the individual components ([3.1], [3.2], [3.3], [3.4]), but also focusing on power quality [3.5]. However, all these studies deal with the most common electric propulsion option, which includes a constant speed generator supplying a fixed voltage/fixed frequency three-phase bus. A PWM drive is used to control the propeller shaft speed.

An alternate electric propulsion system was recently proposed [3.6], which employs a variable voltage variable frequency system (VVVF) as shown in Figure 3.1. The proposed system utilizes a direct connection between the variable speed generator and the propulsion motor, thereby avoiding both the ac-dc and dc-ac conversion required by previous schemes. This provides significant potential advantages in efficiency, space required, and cost.

This paper presents an in depth analysis of the proposed VVVF system, including detailed modeling of the gas turbine and propeller. Additionally, the ability of this VVVF system to respond to pulse loads is investigated. Results clearly show that the proposed system has power regenerating capability and good stability under large pulse load conditions. During pulse conditions, the VVVF drive is able to draw kinetic energy from the turbine-generator, the propulsion motor and propeller, and the hydrodynamic propeller load.

Based on the conceptual diagram of Figure 3.1, the system is divided into three parts for analysis and modeling convenience: the gas turbine/generator unit (A), the propeller motor and its hydrodynamic load (B) and the AC/DC converter for ship service load (C). The propeller speed is controlled by the turbine. The drive motor will operate at the same speed as the turbine, in the case of a synchronous motor, or at a slight slip, in the case of an induction motor. The generator and motor will be electromagnetically compatible, so that an essentially fixed field current in the generator will result in appropriate voltage and flux levels in both the generator and the motor.

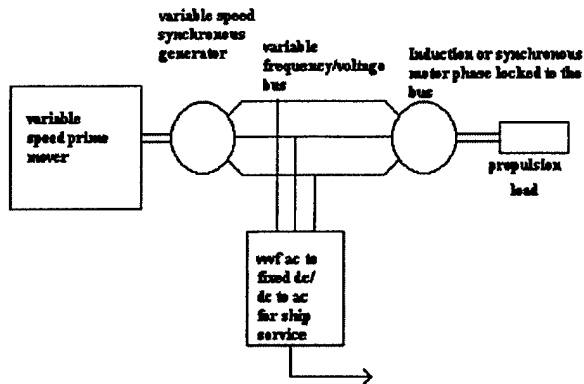


Figure 3.1 Conceptual Diagram VVVF

3.2. Analysis and Modeling

3.2.A Gas Turbine/Generator Unit. Figure 3.2 shows the variable voltage/frequency turbine/generator unit. The masked “Governor” block consists of the typical excitation system, turbine speed governor system and some necessary standard SimPowerSystems measurement blocks. The synchronous generator is based on sixth-order state-space model and rated 3.125MVA, 2.4KV, 60 Hz, 3600 rpm. The generator rating is taken as VVVF system base for per unit calculation. The generator terminal voltage (pu) is proportional to the turbine speed, or system frequency. This is the essential feature of variable voltage variable frequency (VVVF) system.

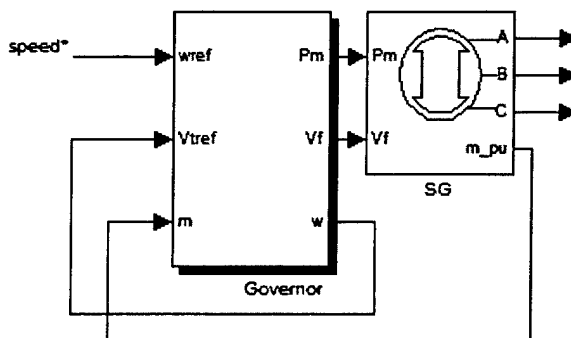


Figure 3.2 Generator/Diesel Engine Unit

Table 3.1. Synchronous Generator parameters in pu

Rotor type	Salient-pole
d-axis synchronous reactance X_d	1.56
d-axis transient reactance X_d'	0.296
d-axis subtransient reactance X_d''	0.177
q-axis synchronous reactance X_q	1.06
q-axis subtransient reactance X_q''	0.177
Leakage reactance X_l	0.052
d-axis transient short circuit time constant T_d' (sec.)	3.7
d-axis subtran. short circuit time constant T_d'' (sec.)	0.05
q-axis subtran. open circuit time constant T_q'' (sec.)	0.05
Stator resistance R_s	0.0036
Coefficient of inertia H	1.07
Friction factor F	0
Pole pairs p	2
Initial speed deviation $\Delta\omega$ (%)	-99.99
Initial electrical angle of the rotor θ_e	0
Initial line current magnitude i_a, i_b, i_c	0, 0, 0
Initial phase angles ph_a, ph_b, ph_c	0, 0, 0
Initial field voltage V_f	1.0

Table 3.2. Excitation System Parameters

Low-pass filter time constant T_r (sec.)	20e-3
Regulator gain and time constant K_o (pu), T_o (sec.)	200, 0.02
Exciter gain and time constant K_e (pu), T_e (sec.)	1, 0
Transient gain reduction time constants T_b, T_c (sec.)	0, 0
Damping filter gain and time constant K_f (pu), T_f (sec.),	0.001, 0.1
Regulator output limits $E_{f\min}$ (pu), $E_{f\max}$ (pu), K_p (pu)	0, 6, 0
Initial terminal voltage and field voltage V_{r0}, V_{f0} (pu)	1, 1

Table 3.3. Turbine Governor System Parameters

Regulator gain K (pu)	40
Regulator time constants T_1 , T_2 , T_3 (sec.)	0.01, 0.02, 0.2
Actuator time constants T_4 , T_5 , T_6	0.25, 0.009, 0.0384
Torque limits T_{\min} , T_{\max} (pu)	0, 1.1
Turbine time delay T_d (sec.)	0.024
Initial value of mechanical power P_{m0} (pu)	0.000270

The parameters of synchronous generator, excitation system and turbine speed governor system are directly from [3.7], and given in Tables 3.1, 3.2, 3.3, respectively. Per unit values are to the generator base.

3.2.B Propeller Motor and its Hydrodynamic Load. The electrical part of the propeller motor is represented by a fourth-order state-space model and the mechanical part by a second-order system. All stator and rotor quantities are in the arbitrary two-axis reference frame (dq frame). The propeller load is designed to draw the system power of 0.9 p.u. at rated shaft speed. The parameters of induction motor are converted into per unit with reasonable enlarged inertia constant corresponding to higher rating in our case study.

In this research, the propulsion model is based on a simplified dynamic thruster model discussed in Reference [3.8]. This model includes the dynamic flow effects that occur during increase or decrease of the thruster shaft torque. This model has been validated under standstill conditions. It is somewhat less accurate under more general conditions, but still provides sufficient information for the purposes of this study.

The propulsion model is:

$$\begin{aligned}\dot{v}_p &= (\rho a \gamma)^{-1} T - (\rho a \gamma)^{-1} (\Delta \beta \rho a) v_p |v_p| \\ T &= L \cos(\theta) - D \sin(\theta) \\ Q &= 0.7 r L \sin(\theta) + D \cos(\theta)\end{aligned}\tag{3.1}$$

Where:

$$v_t = 0.7 r \Omega$$

$$\theta = \tan^{-1} \left(\frac{v_p}{v_t} \right)$$

$$\alpha = p - \theta$$

$$v = \sqrt{v_p^2 + (0.7r\Omega)^2} \quad (3.2)$$

The lift and drag forces L and D in Eq. 3.1 are computed by employing a truncated Fourier approximation as:

$$L = \frac{1}{2} \rho v^2 a C_{L_{\max}} \sin(2\alpha) \quad (3.3)$$

$$D = \frac{1}{2} \rho v^2 a C_{D_{\max}} (1 - \cos(2\alpha))$$

Parameters of the propeller motor and propeller system are given in Tables 3.4 and 3.5, respectively:

Table 3.4. Propeller Motor Parameters

Stator resistance R_s	15.7e-3
Stator leakage inductance L_{ls}	0.123
Rotor resistance R_r	11.9e-3
Rotor leakage inductance L_{lr}	0.123
Mutual inductance L_m	7.07
Inertia constant H	0.5
Friction factor F	0
Pair of poles p	2
Initial slip s	1
Initial electrical angle θ_e	0
Initial stator current magnitude i_{as}, i_{bs}, i_{cs}	0, 0, 0
Initial phase angles ph_a, ph_b, ph_c	0, 0, 0

Table 3.5. Propeller System Parameters

Density of water ρ	998
Duct (axial flow) length l	1.0
Added mass coefficient γ	2.0
Flux coefficient $\Delta\beta$	1.86
Radius of propeller r	1.1
Thruster duct area a	3.85
Propeller blade average pitch p	0.39
Max. Lift coefficient $C_{L_{\max}}$	0.542
Max. Drag coefficient $C_{D_{\max}}$	1.25

The input to the propulsion model is the propeller shaft angular velocity Ω , and the output is the propeller shaft torque Q . This quantity is converted to per unit on the system base, for input to the induction motor

model. Notice that the propeller angular velocity at full load is assumed to be 9.84 rad/sec or 94 rpm when neglecting the gear losses. Finally, the propeller motor and hydrodynamic load system is shown in Figure 3.3.

3.2.C AC/DC Ship Service Load Converter. For our case study, the ship service power is fed by an AC/DC converter. The steady ship service load is assumed to be constant at 0.1 p.u. power throughout this study.

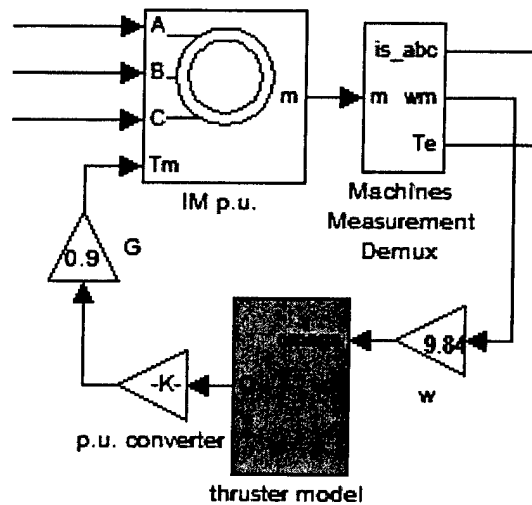


Figure 3.3 Propeller Motor/Hydrodynamic Load

Figure 3.4 shows the simplified converter topology.

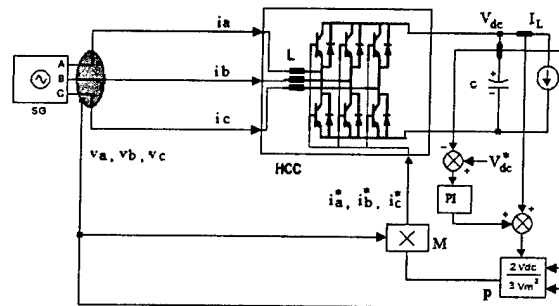


Figure 3.4 Three-phase PWM AC/DC Converter Topology

The DC bus voltage V_{dc} is sensed and compared with a reference value V_{dc}^* which is the desired DC bus voltage (1.0 pu). The voltage error is processed by a PI controller. The limited output of the PI controller is considered as one magnitude component of three-phase reference input currents i_a^*, i_b^*, i_c^* which keeps the actual DC bus voltage V_{dc} close to the given value V_{dc}^* . Another magnitude component of i_a^*, i_b^*, i_c^* is the DC load current I_L which balances the AC power flow in and DC power flow out. The sinusoidal phase reference is obtained from sensed three-phase voltage v_a, v_b, v_c to ensure the reference input three-phase currents i_a, i_b, i_c are in phase with the three-phase voltage. Since this converter topology ensures that the three-phase current injected into the hysteresis current controller (HCC) is sinusoidal and in phase with system voltage, the system can be essentially treated as three-phase balanced system.

The processor P and multiplier M implement algorithm to develop the three-phase reference currents i_a^*, i_b^*, i_c^* . The voltage magnitude V_m is calculated base on the three-phase balanced voltage equation:

$$V_m = \sqrt{\frac{2}{3}(v_a^2 + v_b^2 + v_c^2)} \quad (3.4)$$

An initial study showed the ability of the hysteresis controller to regulate the dc bus voltage. This study also showed that the filtering was sufficient to reduce the high frequency impact to acceptable levels. For the subsequent system studies, this model was overly complex, and a fast simulation model of the PWM was developed which has sufficient accuracy for the purposes of this study. It is known that the switching frequency quantities do not have an impact on the system dynamic performance, particularly when the instantaneous output voltage ripple is made small by design. What we are really concerned about is the continuous-time dynamic behavior of the system. Thus a continuous-time state space model, or state-space averaged model, can be employed to represent the PWM converter while reasonably neglecting the switching frequency response.

Reference [3.9] presents a circuit averaging model for a DC converter. The averaging model for the HCC controlled converter of this study is shown in Figure. 3.5.

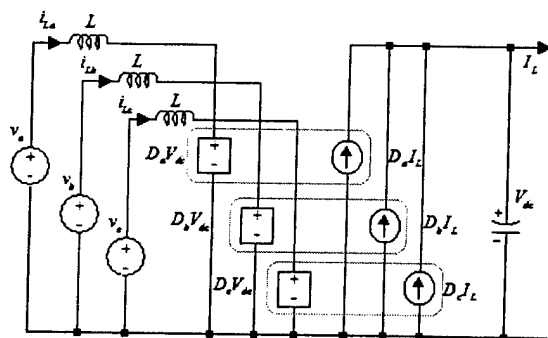


Figure 3.5 Fast Simulation Model of HCC

In Figure 3.5:

$$\begin{aligned} D_a' &= 1 - D_a \\ D_b' &= 1 - D_b \\ D_c' &= 1 - D_c \end{aligned} \quad (3.5)$$

Where D_a, D_b, D_c are the controller averaged duty ratios of phase a, b and c.

According to KVL:

$$\begin{aligned} L \frac{di_a}{dt} &= v_a - D_a' V_{dc} \\ L \frac{di_b}{dt} &= v_b - D_b' V_{dc} \\ L \frac{di_c}{dt} &= v_c - D_c' V_{dc} \end{aligned} \quad (3.6)$$

According to KCL:

$$C \frac{dV_{dc}}{dt} = D_a' i_a + D_b' i_b + D_c' i_c - I_L \quad (3.7)$$

The input is three-phase voltage and current supply as follows:

$$\begin{aligned} v_a &= V_m \cos(\omega t) \\ v_b &= V_m \cos(\omega t - \frac{2}{3}\pi) \\ v_c &= V_m \cos(\omega t + \frac{2}{3}\pi) \end{aligned} \quad (3.8)$$

$$\begin{aligned} i_a &= I_m \cos(\omega t) \\ i_b &= I_m \cos(\omega t - \frac{2}{3}\pi) \\ i_c &= I_m \cos(\omega t + \frac{2}{3}\pi) \end{aligned} \quad (3.9)$$

Combining Equations (3.6) and (3.7) with (3.8), (3.9), eliminating D_a', D_b', D_c' and employing trigonometric conversion, we obtain:

$$C \frac{dV_{dc}}{dt} = \frac{3V_m I_m}{2V_{dc}} - I_L \quad (3.10)$$

Equation 3.10 reveals the state-space averaged relationship between three inputs state variables: the bus voltage magnitude V_m , injected current magnitude I_m and converter output DC current I_L , and an output state variable: converter output DC voltage V_{dc} . Although the three-phase HCC topology is complex, the averaged expression is valid for dynamic studies, and is greatly simplified.

The HCC fast simulation model (3.10) is implemented in Simulink as shown in Figure 3.6. The current injected into the HCC is implemented using a controlled current source regulated by the reference currents i_a^* , i_b^* , i_c^* as shown in Figure 3.5.

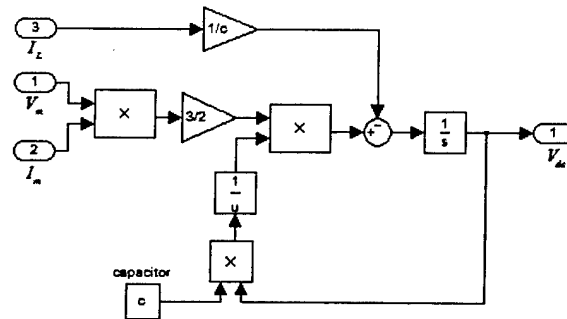


Figure 3.6 Implementation of Fast

3.3. Simulation Results

3.3.A. Fixed Pitch Propeller There are two critical aspects of the proposed VVVF system—the ability of the propulsion system to accelerate the propulsion load, and its ability to serve pulse loads. Figures 3.7 through 3.10 present the results of a typical study which includes both of these events. Beginning at time zero, the system accelerates to rated speed. At some point as the drive accelerates, the HCC controller is able to regulate the dc bus voltage. Following this, at a simulation time of 2 seconds in these cases, the ship service load of 0.1 per unit is applied. A pulse load of magnitude 1.67 per unit and duration of 1 second is applied at 10.5 seconds. The propulsion steady ship service load models are as described in the previous sections. The pulse load is fed from the same dc bus as the steady ship service load. This particular case shows a pulse load which is the maximum pulse that the system can support under this operating condition.

Figure 3.7 shows the induction motor current throughout this period. There is a brief startup transient with low frequency currents, followed by a period when the current magnitude (and frequency) increase as the propeller speed and load increase. The drive takes about 6 seconds to accelerate to a steady state load. The

pulse load results in a significant reduction in motor current draw, and a short period of high current as the motor reaccelerates after the pulse load is removed.

Figure 3.8 shows the generator and motor speeds (in per unit) over the same time period. Following a brief high slip period at time 0, the generator and motor accelerate together to the steady state. They decelerate together during the period when the pulse load is on (10.5 to 11.5 seconds) with a short period of negative slip at the end of this period. During this period, the motor operates as a generator, providing energy to the pulse load. This in turn allows the system to support a larger pulse load than would otherwise be the case. Once the pulse load is off, there is again a brief period of high slip as the motor accelerates, followed by a low slip acceleration back to the steady state speed.

The generator and motor electrical torques are shown in Figure 3.9. The initial acceleration is apparent in this plot, as is the point at $t=2$ seconds, where the ship service load is turned on with minimal transient. When the pulse load is initiated at 10.5 seconds, the response of both the generator and motor torques is nearly instantaneous, with the generator picking up torque, and the motor dropping torque. These torques then vary slowly as the system decelerates, with a negative torque starting at about 11 seconds. At the conclusion of the pulse load, the system reaccelerates, in a similar fashion to the initial acceleration.

Figure 3.10 shows the dc bus of the ship service load. At very low speeds, this bus cannot be regulated. In actual practice, the ship propulsion would be started with the turbine generator operating at some point above this minimum speed, by switching in the propulsion motor. The switching in of the 0.1 pu steady ship service power creates a minimal transient at 2.0 seconds. The pulse load, however, does create a significant transient at 10.5 seconds. This is a dual effect of the drop in frequency and the loading of the dc bus by the pulse load. This particular case shows a significant drop in voltage during the pulse, and is the limiting parameter of this case.

Regardless of initial speed and loading, the power system will collapse at some level of pulse load due to the large transient currents. This is referred to as the critical pulse load. A simulation on the pulse load response of the VVVF system was done with parameters given in Section 3.2. Two cases were evaluated in this study, to determine the critical pulse load for the system with the drive motor on, and the critical pulse load when the ship is at standstill and the drive motor is switched off. Table 3.6 shows the results of this study, over the speed range of 0.4 to 1.0 per unit. Table 6 shows that this system has significant pulse load capability in both operating modes. With the propulsion system off-line, the pulse load capability ranges from 0.4 to 1.5 per unit, depending on the generator speed/frequency. Table 3.6 also shows that the pulse load capability actually increases when the propulsion motor is on. This is due to the ability of the propulsion system to feed energy to the pulse load during this period.

3.3.B. Variable Pitch Propeller The study also considered cases involving variable pitch propellers, in order to determine if the potential impact of this technology on the ship's ability to serve pulsed loads. This phase of the study assumed that the propeller pitch could be changed with an 0.5 second time constant. Figures 3.11 through 3.14 plot the motor current, generator/motor speeds, corresponding electrical torque and AC/DC converter output voltage curves showing the response to a pulse load of 2.09 pu. In steady-state, the system operates at some speed with 0.1 p.u. constant DC load connected. These figures show the critical pulse load for an initial generator speed of 1.0 pu and an initial ship service load of 0.1 pu. A change in pitch is initiated 0.5 seconds before the pulse load comes on. At $t=10.5$ s, a pulse load lasts for 1 second. The pitch is changed back to its steady state setting when the pulse load goes off. These plots show a similar response to the fixed pitch plots, with minor exceptions. The primary change in the nature of the plots is in response to the change in pitch initiated at 10.0 seconds. The pitch change does, however, result in a significant improvement in the magnitude of the pulse load that can be served. The critical pulse load values for the variable pitch case are shown in Table 3.6, along with the previous results for the fixed pitch case, and for the standstill case.

As Table 3.6 shows, over the full range of speeds considered, there is approximately 10% critical pulse load improvement with FPP system, and 35% with VPP system at higher speed. In any case, this drive system has significant pulse power capability under all of these scenarios, and it can serve this load with very little impact on the propulsion system.

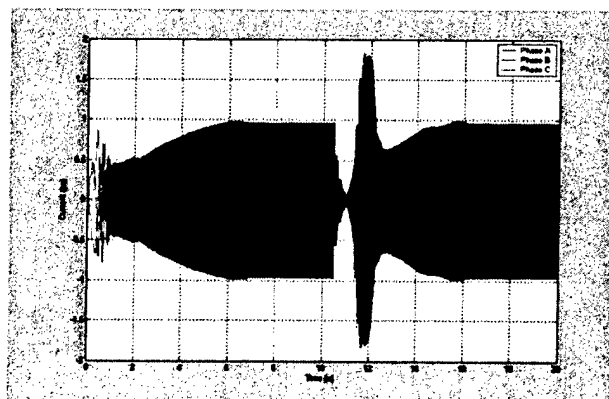


Figure 3.7 Propeller motor current at critical pulse load case (FPP)

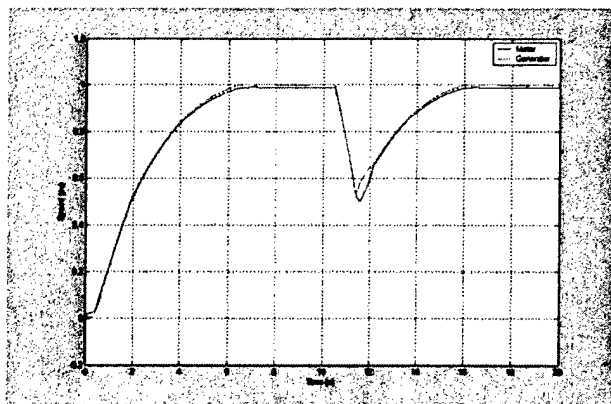


Figure 3.8 Generator and motor speed at critical pulse load (FPP)



Figure 3.9. Generator/motor electric torques at critical pulse load (FPP)

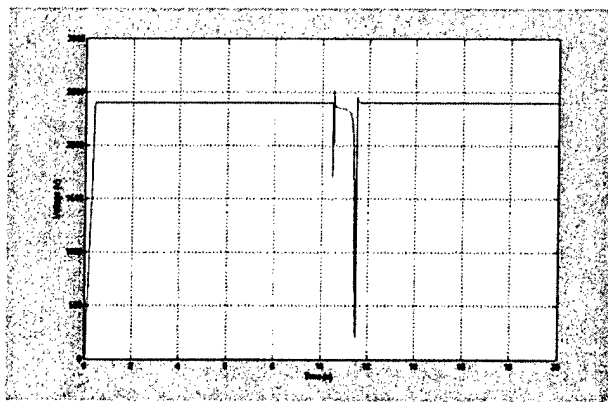


Figure 3.10. Converter output DC voltage at critical pulse load (FPP)

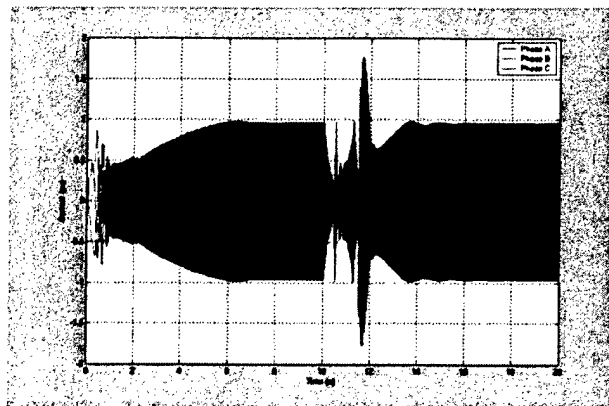


Figure 3.11. Propeller motor current at critical pulse load case (CPP)

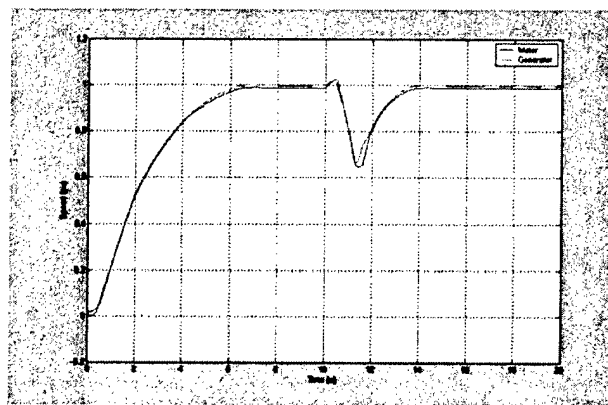


Figure 3.12 Generator and motor speed at critical pulse load (CPP)

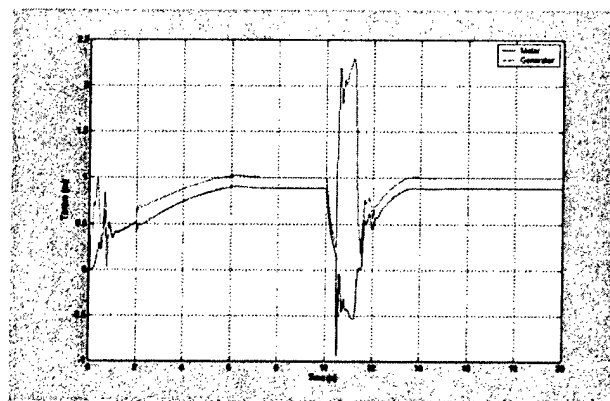


Figure 3.13 Generator/motor electric torques at critical pulse load (CPP)

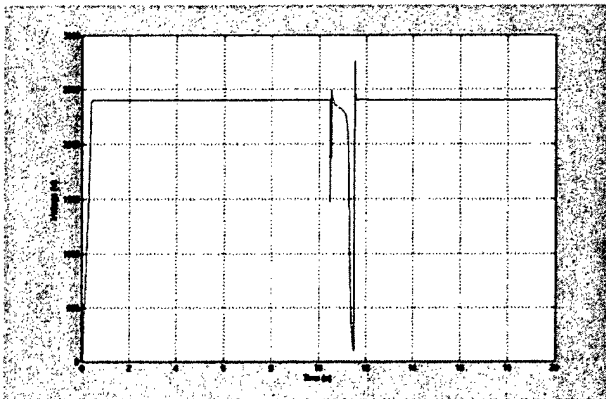


Figure 3.14. Converter output DC voltage at critical pulse load (CPP)

Table 3.6. Comparison of Critical Pulse Load with/without Propeller Motor

Speed (pu)	Critical pulse load without propulsion motor (pu)	Critical pulse load with propulsion motor (pu)
0.4	0.34	0.42
0.6	0.67	0.86
0.8	1.05	1.40
0.9	1.26	1.73
1.0	1.49	2.09

3.4. Conclusion

This chapter focuses on the dynamic performance of a variable voltage, variable frequency (VVVF) ship propulsion system. In particular, the ability of this system to serve significant pulse loads is investigated. The VVVF system operates with a direct electrical connection between the generator and propulsion motor, reducing size, cost, and losses of this system. The system employs an ac-dc converter to serve the ship service load. The ability of this system to provide propulsion power and ship service power has been investigated. It is shown that the steady state ship service load can be served improvement as long as the turbine-generator speed is maintained above a certain value. The ability for the VVVF scheme to serve large pulse loads has been investigated, with the study model based on a 3.1 MVA generator. The study suggests that the VVVF has the capability of serving large 1 second pulse loads under a variety of propulsion considerations, up to a value of twice rated generator power. The study suggests that the critical pulse load increases when the ship is underway, due to the regeneration of power by the drive motor. We summarize and conclude the advantage of variable voltage/frequency drive system (VVVF) here:

1. VVVF can reduce system cost, size and complexity by eliminating the high power derive rectifier/converter system and auxiliary system.

2. VVVF has improved efficiency at steady-state over common fixed voltage/frequency system.
3. The VVVF system will have the ability to serve significant pulse loads over a wide variety of operating conditions.

These study results indicate that there are significant advantages to VVVF ship propulsion. Large scale tests of this type of system should be pursued, particularly as regards to the pulse load capability of the system.

References

- [3.1] C.G. Hodge, D.J. Mattick, "The Electric Warship I", Transactions of International Marine Engineering, Vol. .108, Part 2 (1996), pp. 102-114.
- [3.2] C.G. Hodge, D.J. Mattick, "The Electric Warship II", Transactions of International Marine Engineering, Vol. .109, Part 2 (1997), pp. 127-144.
- [3.3] C.G. Hodge, D.J. Mattick, "The Electric Warship III", Transactions of International Marine Engineering, Vol. .110, Part 2 (1998), pp. 119-134.
- [3.4] D. Parker, M. Bolton: "The Electric Warship", Proceedings of International Conference on the Naval Technology for the 21st Century, Hellenic Naval Academy, pp. 43-48, 29-30 June 1998, Piraeus (Greece).
- [3.5] J.M. Prousalidis, N.D. Hatzigyriou, B.C. Papadias, "On Studying Ship Electric Propulsion Motor Driving Schemes", 4th International Conference on Power System Transients (IPST 2001), Rio de Janeiro, Brazil, June 24-28, 2001.
- [3.6] T. Ortmeyer, L. Ban, K. Joshi, and X. Yan, "Novel Variable Voltage Variable Frequency Electric Drive." Conference Proceedings, 2003 Large Engineering Systems Conference on Power Engineering, Montreal, May, 2003. pp. 44-49.
- [3.7] "Three-Phase Systems and Machines", The Mathworks, Inc.
<http://www.mathworks.com/access/helpdesk/help/toolbox/physmod/powersys/powersys.shtml>.
- [3.8] L. L. Whitcomb and D. R. Yoerger. "Comparative experiments in the dynamics and model-based control of marine thrusters", In Proceedings of IEEE/MTS OCEANS'95, volume 2, pages 1019{1028, October 1995.
- [3.9] D.Maksimovic, A.M.Stankovic, V.J.Thottuveilil, G.C.Verghese, "Modeling and simulation of power electronic converters," invited paper, Proceedings of the IEEE, Vol.89, No.6, June 2001.
- [3.10] Michael Kasten, "some notes on controllable pitch propellers",
<http://www.kastenmarine.com/CPprops.htm>, Kasten Marine Design, Inc.
- [3.11] Xia Yan and Thomas H. Ortmeyer. "Novel electric drive with power-regenerating capability: modeling and simulation." Conference Proceedings, 11th International Conference on Harmonics and Quality of Power. Paper hqp 158. Sept. 2004, Lake Placid, NY.

Chapter 4

Improved Motor Starting Capability of Three Phase UPS Inverters

4.1. Introduction

Induction motors form a considerable portion of industrial loads; accounting for as much as 75% of the system load[4.3]. Increasingly in specialized power systems, fixed frequency inverters are supplying general loads, which include induction motors. These applications include stand large uninterruptible power supplies (UPS), as well as installations where advanced generation technologies, such as fuel cells, photovoltaics, and microturbines, are operating in the stand-alone mode. These inverters have sharply reduced overload capability as compared to standard grid fed distribution systems. Induction motor starting current can easily overload such an inverter, if the system is not properly planned. In many cases, the size of the largest motor that can be fed by the inverter is limited, and the inverter must be derated to allow for motor starting. This paper investigates the development of a current limiting strategy to overcome this effect. In the following sections, two current limiting algorithms are introduced. The effectiveness of these algorithms is investigated through simulation, and their relative merits are discussed. It is concluded that either method would provide improvements in motor starting capability in these situations, and would reduce the level of inverter derating that is required.

4.2 System Description

4.2.A. System Model In the case of stand-alone distributed generation systems and large uninterruptible power system (UPS) installations, a PWM inverter feeds a set of general loads with standard frequency and voltage magnitude requirements. This application is quite different from motor drive applications, where a single induction motor is directly connected to the inverter, and no parallel load is permitted.

When fed by a source with fixed frequency and voltage magnitude, the starting current of three phase induction motors is typically about 6 to 7 times of the rated motor current. This level of inrush current will definitely overload the inverter when the motor rating is a significant fraction of the inverter rating. In a simplified example, for a 100 KVA inverter, a 1 KVA induction motor would have a starting value of 6 KVA, so the maximum parallel load in this case is approximately 94 KVA in order to avoid overloading the inverter during motor starting. The total load rating include parallel load and induction motor in normal running condition is 95 KVA as 95% of the inverter rating. With the same inverter but increasing the motor

size to 10 KVA, the maximum parallel load rating in this case to avoid overloading the inverter is approximately 40 KVA, to allow 60 kva inrush current. The steady state loading of this inverter would then be limited to the maximum parallel load plus the motor load—in this case around 50% of the inverter rating.

This study proposes a new inverter control method that will improve the large motor starting capability of these inverters. The proposed controller introduces a current limiter into the inverter control algorithm. With its control, the inverter output voltage is decreased as the inverter current approaches the limit level of current limiter. A simplified block diagram of the system is shown in Figure 4.1. The controller reduces the total inverter current during motor inrush by introducing a voltage sag at the inverter terminals. The controller must be designed so that these voltage sags allow successful motor starting, and do not affect the parallel load.

Another possible control strategy would be to adjust the inverter frequency during motor starting, within the standard limits. A preliminary study of this frequency modulation indicated that voltage reduction was the more effective approach.

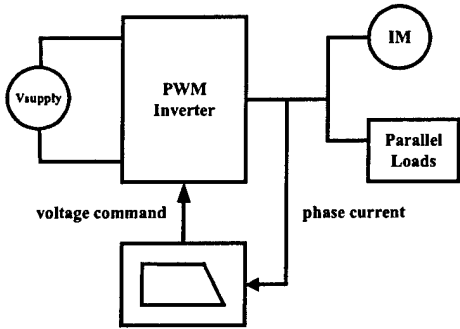


Figure 4.1. Inverter Control Block Diagram

inverter fundamental output frequency.

The induction motor in this study is simulated with a flux linkage based dq axis model, with 4 electrical states[4.1, 4.3]. The model study was conducted using Pspice circuit simulation package.

An idealized inverter model is used in this study. The model is based on the state space average theory [4.4-4.5], which neglects the PWM frequency effects of the inverter. In this model, the inverter is considered to instantaneously implement the controller command voltage on a short term average basis. This model is accurate for three phase voltage source inverters, without regard to their topology and PWM strategy, when the inverter switching frequency is at least 20 times the

4.2.B. Control Methods Power electronic inverters have limited short term overload capability. As a result, there are many applications where an inverter must be derated, in order to allow sufficient margin

during motor starting. In this study, a method of avoiding overcurrent situations is investigated which involves reducing the inverter output voltage as the current limit is approached.

Two methods of implementing the current limiter were investigated in this research.

1) **Method 1:** Method 1 uses the rms current magnitude as the controlling variable and controls the rms voltage.

This method results in balanced, sinusoidal voltages during overload conditions.

2) **Method 2:** Method 2 uses the instantaneous phase currents as the controlling variable in the limiter and controls the instantaneous voltage of each phase independently.

This method results in distorted voltages which could have a slight imbalance during motor starting.

4.2.C. Controller Settings For the purposes of this study, the following parameters have been defined:

A: inverter rating, in per unit to the motor base;

C: parallel load rating, in per unit to the motor base;

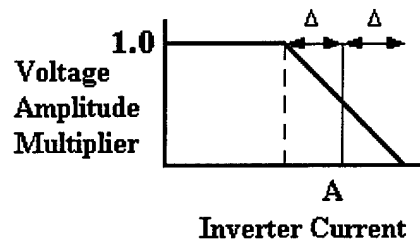


Figure 4.2. Limiter Table Settings.

TABLE 4.1.
COMPARISON OF METHOD 1 AND 2 FOR A=3

Method	R	V_{rms} (per unit.)	I_{rms} (per unit)	T_{acl} (second)	VTHD
1	0.33	0.53	1.19	0.84	0
2	0.33	0.66	1.40	0.59	29.5%
1	0.67	0.48	1.21	1.17	0
2	0.67	0.60	1.45	0.77	31.3%

I_{rms} is per unit value to the inverter base. The motor rating is 1/3 of inverter rating. Parallel load rating is R of the inverter base. VTHD is total voltage harmonic distortion rate. T_{acl} is motor accelerating time.

TABLE 4.2.
COMPARISON OF METHODS 1 AND METHOD 2 FOR A =5

Method	R	V_{rms} (per unit)	V_{rms} (per unit)	T_{acl} (second)	VTHD
1	0.20	0.87	1.12	0.32	0
2	0.20	0.94	1.19	0.29	6.93%
1	0.40	0.77	1.14	0.39	0
2	0.40	0.87	1.26	0.33	11.90%
1	0.60	0.70	1.16	0.49	0
2	0.60	0.81	1.32	0.39	16.70%
1	0.80	0.63	1.17	0.62	0
2	0.80	0.75	1.36	0.46	20.20%

I_{rms} is per unit value to inverter base. Motor rating is 1/5 of inverter rating. Parallel load rating is R of inverter base. VTHD is total voltage harmonic distortion rate. T_{acl} is motor accelerating time.

R: parallel load rating, in per unit to the inverter base (equals C/A);

m: motor rating to inverter base (equals 1/A);

As mentioned in Section 4.2.A, the limiter design is a function of the inverter rating. In other words, limiter settings will be proportional to the inverter rating A, the value of A is used to define phase current at the midpoint of the limiter table height; the corner points of the limiter table are obtained by the middle point value plus or minus a small deviation Δ .

The current at the midpoint of the voltage reduction is

$$X_2 = 1.2 \times \sqrt{2} \times A \quad [4.1]$$

The factor 1.2 allows for the short term overload capability of the inverter.

Fig. 4.2 shows settings of the limiter table. Preliminary results showed that a value of $\Delta = 0.75$ per unit to

the inverter base was reasonable, and that the results were not particularly sensitive to this value.

4.2.D. Comparison Results of Limiter Test results for method 1 and method 2 are shown in Table 4.1, for the case of inverter rating of $A=3$, which corresponds to the motor rating being $1/3$ of the inverter rating. Without either limiting method in place, the starting current of this motor would be approximately twice the inverter rated current, which is not acceptable.

The method 1 algorithm, however, successfully limits this current to an overload of approximately 20%, even with parallel loads of one to two times the motor rating. In order to accomplish this, the inverter output voltages are reduced to approximately half of the rated value.

The acceleration time for unloaded motors is shown in the column labeled as T_{acl} . The acceleration time is increased due to the lower voltage and higher starting current. Also, motors starting with large shaft loads may not be able to start under these conditions. This was not investigated during this study. On the other hand, it is clear that this motor could not start without a limiter, even when no other load is present on the inverter.

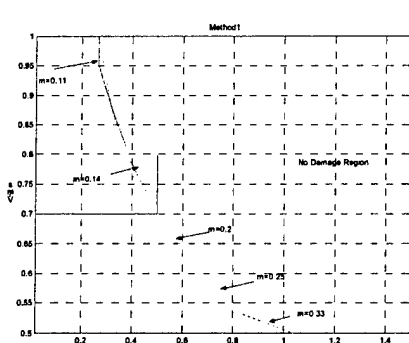


Figure 4.3. Comparison of Voltage Sags with the ITIC Curve, Control Method 1

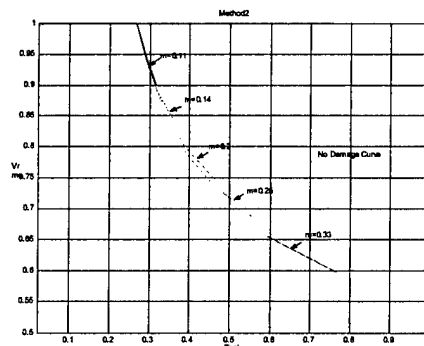


Figure 4.4. Comparison of Voltage Sags with the ITIC Curve, Control

Compared to method 1, method 2 provides higher voltage levels and faster acceleration time. For the parallel load of $R=0.33$ pu, the rms voltage is increased from 53.1 % to 65.5% of rated voltage. In a similar fashion, the acceleration time of an unloaded motor is reduced. To achieve this, however, method 2 creates significant harmonic distortion levels—VTHDs of around 30%.

Table 4.2 presents the corresponding study results for the case of the inverter rating equal $A=5$, which corresponds to the motor rating being 20% of the inverter rating. Table 4.2 shows similar trends to Table 4.1 with generally lesser sag levels and VTHDs, as could be expected.

Tables 4.1 and 4.2 show that method 2 tends to have higher rms currents than method 1. The two methods, however, have the same peak values regarding the inverter currents. Therefore, the comparisons between method 1 and method 2 are reasonable although they have different inverter current rms values.

The study involved inverter ratings ranging from three to nine times the motor rating. In the following sections, the range of effects of the two control methods is examined.

4.3. Effects of Limiter Implementation

In order to assess the impact of the voltage sag, the ITIC curve [8] was used. This curve was developed by the Information Technology Industry Council, and was recently revised from the more familiar CBEMA curve, which was cited by numerous IEEE standards and other documents. The ITIC curve allows voltage sags to 70% of the rated values for up to 0.5 seconds, and voltage sags to 80% of rated values for up to 10 seconds. Fig. 4.3 and Fig. 4.4 record the voltage sag levels for the various levels of motor size considered in this study for method 1 and method 2 respectively. The scale of the vertical axis is the inverter output rms voltage; the scale of the horizontal axis is the motor accelerating time. The locus of points plotted for a given m value result from increasing levels of parallel loads. The step curves in both Fig. 4.3 and Fig. 4.4 are part of the ITIC curves. That is for a given case of m the motor has a “good start” with the voltage sag curves above the ITIC curve and has a “bad start” with the voltage sag curves below the ITIC curve with limiting methods in place.

Fig. 4.3 shows that motor sizes corresponding to $m=0.11$ and $m=0.14$ will not violate the ITIC curve limits for any loading levels up to the inverter rating. For motor sizes of $m=0.25$ and $m=0.33$, the voltage sag will violate ITIC constraints for any starting situation. In the case of $m=0.2$, the motor could be started without violating these criteria as long as the parallel connected load is below a certain level.

Fig. 4.4 shows that method 2 allows for the $m=0.2$ motor to be started without violations, and the $m=0.25$ motor to be started without violation for most of the range of inverter loading. Comparing method 1 and method 2 considering sag levels and acceleration time, method 2 produces less severe voltage sags and faster acceleration than method 1 does. However, method 2 has high distortion rates. It is unclear how parallel loads would tolerate these distortion rates for short periods of time.

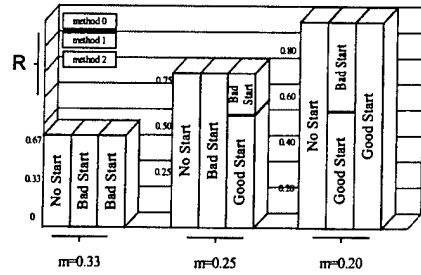


Figure 4.5. Starting Performance Comparison of the 3 methods: No start= inverter overload shutdown, Bad start=ITIC Curve violation, Good

Fig. 4.5 presents a summarized comparison among method 1, method 2 and method 0 (no control applied) for the large motor cases. Method 0 is considered to fail if the motor starting current plus parallel load current is greater than the inverter rating, when the inverter output voltage is at its rated value. This bar diagram shows that motor starting performance has been improved by using both proposed control methods and the instantaneous method is better than the average rms method for attaining a larger good start range

The scale of the vertical axis in Fig. 4.5 is the parallel connected load rating in per unit to the inverter base. From the bar comparison, method 0 (no control applied) never allows starting for motors rated greater than 20% of the inverter rating, under any parallel loading conditions. With the inverter voltage controlled through either method 1 or method 2, the unloaded motor is able to start for motor sizes ranging up to 33% of the inverter rating. When the motor rating is 0.33 per unit to inverter base in both method 1 and method 2, however, the motor is in the “bad start” situation as it violates the voltage sag constraints of the ITIC curve. When motor rating is 0.25 per unit to inverter base, the motor starting always causes an excessive sag in method 1 but has the “good start” in method 2 when the connected load rating is less than 0.60 per unit to the inverter base. When the motor rating is 0.20 per unit to inverter base, the motor has “good start” in method 2 for the full range of possible parallel loads, and has “good start” in method 1 when other load is above 0.58 per unit to the inverter base.

4.4 Conclusions

In this study, two alternate methods have been introduced which allow for increased motor starting capability for fixed frequency inverters feeding general power system loads. Through extensive simulations, both of these methods have been shown to provide substantial improvements to the loading serving capability of these inverters. When operating the inverter in its standard mode, the inverter would be limited to approximately 50% of the steady state full load capability for a motor sized at 10% of inverter

rating, and would fail to allow any motor to start which is over 20% of the inverter rating, even with no other load rating. When these alternate methods are implemented, however, the inverter is able to support full steady state loading when the load mix includes individual motors as large as 20% of the inverter rating. With the method 2 implementation, this can be done without violating the ITIC curve voltage sag limits, while this limit would be violated at higher inverter parallel loading with the method 1 implementation. Larger motors can be started at light loads or with ITIC curve violations allowed.

Method 2 provides superior voltage sag performance. This method, however, creates significant levels of harmonic distortion in the inverter output, with VTHD levels up to 30% in test cases. These levels are above steady state VTHD limits, but persist only for short times, which correspond to the motor starting times. The effect of these short duration high VTHD levels is unknown.

REFERENCES

- [4.1] Chee-Mun Ong, *Dynamic Simulation of Electric Machinery Using MATLAB/SIMULINK*, Prentice Hall PTR, 1997, pp. 167-243
- [4.2] T. H. Ortmeyer, C. L Bradley, "Inverter Performance and Derating for General Three Phase Loads," *IEEE Power Engineering Society Summer Meeting*, Vol.2, pp. 1041 –1046, 2000
- [4.3] Prabha Kundur, *Power System Stability and Control*, McGraw-Hill, Inc, 1994, pp. 271-300
- [4.4] Mohan, Undeland, Robbins, *Power Electronics Converters, Applications and Design*, John Wiley & SONS, INC.1995, pp. 323-331
- [4.5] Muhammad H. Rashid, *Power Electronics, Circuits, Devices, and Applications*, 2nd, Prentice Hall, 1993.
- [4.6] Mohammed Akherraz, *Pspice-Assisted Dynamic Modeling and Simulation of Induction Motor Drive*, IEEE International Electric Machine and Drives Conference, IEMDC, 1st 1997, C-7803-3948-0/97, pMBI 8.1-8.3
- [4.7] Thorsen, O. V., Dalva, M., *Models for Simulation of Induction Motors with Parameter Determination Examples of Application*, IEEE International Electric Machines and Drives Conference, IEMDC, 1st 1997, pMBI 3.1-3.3
- [4.8] ITIC (CBEMA) Curve, Information Industry Council, [Http://www.itic.org](http://www.itic.org)
- [4.9]. Liang Ban and Thomas Ortmeyer. "Improved Motor Starting Capability of Three Phase UPS Inverters." Conference Proceedings, 11th International Conference on Harmonics and Quality of Power, Paper hqp137. Sept. 2004, Lake Placid, NY.

Chapter 5

The Application Of Wavelets To the Detection Of Broken Rotor Bars in Induction Machines

5.1 Introduction

The induction machine is essential in many industrial applications. It is therefore desirable to reduce downtime by employing methods of machine condition monitoring. A widely used method of induction machine condition monitoring utilizes the steady-state spectral components of stator quantities. These spectral components can include voltage, current and power and can be used to detect broken rotor bars, bearing failures, air gap eccentricity etc. Traditionally these techniques have focused on the detection of faults during steady-state machine operation [5.1], [5.2]. The accuracy of these techniques depend on the loading of the machine, the assumption that the machine speed is constant, as well as the signal to noise ratio of the spectral components being examined. The rotor bar frequencies are determined by

$$f_{rotorbar} = f_s \left[k \left(\frac{1-s}{p} \right) \pm s \right], \quad (5.1)$$

where, $k/p = 1, 5, 7, 11, 13\dots$

f_s is the supply frequency,

s is the machine slip,

p is the number of poles.

These frequencies form the stator current spectrum shown in Fig. 5.1 and are present irrespective of the machine's condition. The presence of broken rotor bars is indicated by the difference in amplitude between the fundamental and the left sideband. A difference less than 50dB is an indication of broken rotor bars [5.3]-[5.7]. The amplitude of the left sideband frequency component of the fundamental frequency is proportional to the number of broken rotor bars present [5.8]. The right sideband component, $f_s(1+2s)$, could also be used in monitoring fault severity. The importance of the stator current frequency components is well documented in [5.9]-[5.14].

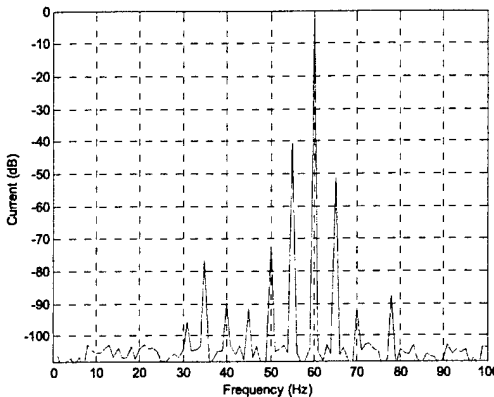


Fig. 5.1. A typical current spectrum of a fully loaded induction motor with broken rotor bars.

From (5.1) it is evident that the rotor bar frequencies are a function of the machine slip. If the machine is unloaded, the slip will be almost zero. The rotor bar frequencies will be masked by the fundamental frequency and thus make detection difficult. The only solution is therefore to heavily load the machine in order to separate the frequencies. Overloading a machine is undesirable since it reduces the machine's operating lifetime and is not generally under control of the operator. Accurate detection therefore is difficult at light loading conditions. In addition many machines spend substantial periods at light loading conditions.

A fundamental disadvantage of the assumption of steady-state speed in condition monitoring is that there are many applications where constant speed operation is not achieved for example in wind generation or motor operated valves. In addition, the steady state algorithms focus only on low slips, while improved detection can be accomplished at high slips.

An alternate approach to the detection of broken rotor bars would be to examine the starting transient of an induction machine. The advantages would be that the transient has a high slip and high signal to noise ratio, which implies that the spectral components can be more easily separated. Loading does not affect the amplitude of the transient during startup. The load only affects the duration time of the startup transient. This implies that the detection can be done at low loading conditions unlike steady-state techniques.

In [5.15] a method for the detection of broken rotor bars and end ring faults, by examining the starting transient, is proposed. The detection algorithm is based on steady-state detection techniques by monitoring the sidebands of the current fundamental. Instead of using the Fourier transform to monitor the sideband frequencies, a Phase Vocoder [5.16] based on the Short-Time Fourier Transform is used to produce a time-frequency representation of the starting current. The shortcoming of the Short-Time Fourier Transform is the fact that it analyses all the frequencies in a signal with the same window and causes resolution problems. The wavelet transform was introduced to overcome the resolution problems encountered when

analyzing transient signals using Fourier analysis. A detailed explanation of wavelets applied to power engineering applications can be found in [5.17]-[5.26].

A challenge of transient analysis is the difficulty in trying to analyze the complex transient startup current signal. This comprises a non-stationary fundamental frequency as well as non-stationary frequencies associated with the rotor bars. The rotor bar frequencies are a function of the machine speed slip and change as the machine runs up.

It is therefore desirable to be able to separate the fundamental frequency from the rotor bar frequencies. Using a high order notch filter will not accomplish this goal because the fundamental frequency is not constant. A filter that actively tracks the changing amplitude, phase and frequency is needed to extract the fundamental from the transient. Once the fundamental frequency has been removed, the residual current can be examined using wavelets because the entire analysis is done in the transient.

5.2 Description Of the Algorithm

Let $u(t)$ denote a signal comprising a sinusoidal component and some undesired components:

$$u(t) = u_o(t) + u_1(t), \quad (5.2)$$

in which

$$u_o(t) = A_o \sin(\omega_o t + \delta_o) \quad (5.3)$$

is the sinusoidal component of interest and $u_1(t)$ is the totality of the undesired components. The latter may in general be comprised of noise, transient disturbances, and sinusoidal components at frequencies other than ω_o . It is desired to obtain an estimate of $u_o(t)$, denoted by $y(t)$, out of the input signal $u(t)$. Least squares error between the input signal $u(t)$ and the estimated sinusoidal signal embedded in $u(t)$, i.e. $y(t)$, is minimized by the method of gradient descent. The cost function is defined as

$$J(t, \theta) = \frac{1}{2} [u(t) - y(t, \theta)]^2 \stackrel{\Delta}{=} \frac{1}{2} e^2(t, \theta), \quad (5.4)$$

where $\theta \in \mathbb{R}^n$ is the vector of parameters, e.g. the amplitude, phase angle and frequency, and is used to define the output (sinusoidal) signal. The gradient descent algorithm provides a method of adjusting the unknown parameter θ so that the cost function J tends to its minimum point. This method is based on the idea of starting from an initial point and moving any unknown parameter to the opposite direction of the variations of the cost function with respect to that parameter. If $n \times n$ matrix μ is defined as $\text{diag}\{\mu_1, \dots, \mu_n\}$ in which $\mu_i, i = 1 \dots n$ are real positive constants, then the gradient descent method can be written as

$$\frac{d\theta(t)}{dt} = -\mu \frac{\partial[J(t, \theta(t))]}{\partial \theta(t)}. \quad (5.5)$$

Fig. 5.2 illustrates the minimization process when achieved using the method of gradient descent in a simple case of one parameter and a quadratic cost function. This method is guaranteed to yield the desired solution if the cost function is globally quadratic in parameters. Otherwise, i.e. if the form of the cost function is not quadratic, as is the case here, or not clearly described, a mathematical proof should be given to guarantee the convergence of the solutions of the gradient descent method (5.5) to the minimum point of the cost function (5.4).

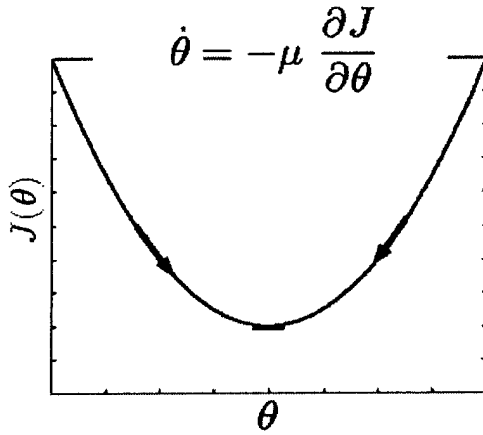


Fig. 5.2. Illustration of the convergence mechanism of the gradient descent method employed to minimize a quadratic cost function.

The output signal is defined as

$$y(t) = A(t) \sin\left(\int_0^t \omega(\tau) d\tau + \delta(t)\right).$$

Formulating the algorithm accordingly using the parameter vector $\theta = [A, \delta, \omega]$, i.e. the amplitude, phase angle and frequency of the desired component, results in the following set of equations [5.27] which governs the dynamics of the algorithm¹:

¹ Strictly following the least squares error minimization using the method of gradient descent results in a time-varying set of equations in which the time variable t is explicitly present in the equations. In the equations presented here, the time variable t is replaced by a constant number. This replacement converts the time-varying system into a time-invariant system. The apparently arbitrary formulation of the algorithm calls for mathematically rigorous justification which is presented in [5.28].

$$\begin{cases} \dot{A}(t) = \mu_1 e(t) \sin \phi(t), \\ \dot{\omega}(t) = \mu_2 e(t) \cos \phi(t), \\ \dot{\phi}(t) = \mu_2 \mu_3 e(t) \cos \phi(t) + \omega(t), \\ y(t) = A(t) \sin \phi(t). \end{cases} \quad (5.6)$$

The dot on top represents the differentiation with respect to time and the error signal $e(t)$ is $u(t) - y(t)$.

The state variables $A(t)$, $\phi(t)$ and $\omega(t)$ directly provide instantaneous estimates of the amplitude, phase angle and frequency of the extracted sinusoid, respectively. The totality of the undesired components and noise imposed on the sinusoidal component of interest is provided by $e(t)$. The parameters μ_1 , μ_2 and μ_3 are positive numbers which determine the behavior of the algorithm in terms of convergence speed versus accuracy. This dynamics presents an algorithm, which is capable of extracting a specified sinusoidal signal, estimating its amplitude, frequency and phase, and accommodating variations in the amplitude, frequency and phase of such a sinusoidal component. In practice, the frequency ω has a nominal value ω_0 and varies around this nominal value. The second and third equations in (5.6) may be rearranged in terms of the deviation element $\Delta\omega = \omega - \omega_0$. An implementation of this system is shown in Fig. 5.3 with three integrators for three state variables.

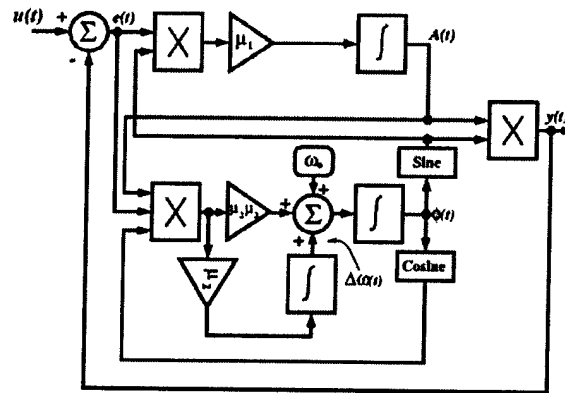


Fig. 5.3. Block diagram representation of the algorithm.

Fig. 5.3 shows implementation of the algorithm in the form of the composition of simple blocks suitable for schematic software development tools. Numerically, a possible way of writing the set of equations governing the present algorithm in discrete form, which can be readily used in any programming language, is

$$\begin{cases} A[n+1] = A[n] + T_s \mu_1 e[n] \sin \phi[n], \\ \omega[n+1] = \omega[n] + T_s \mu_2 e[n] \cos \phi[n], \\ \phi[n+1] = \phi[n] + T_s \mu_2 \mu_3 e[n] \cos \phi[n] + T_s \omega[n], \\ y[n] = A[n] \sin \phi[n], \end{cases}$$

where $e[n] = u[n] - y[n]$. First order approximation for derivatives is assumed in deriving these equations; in other words, the time-derivative of a generic quantity X is approximated by $(X[n+1] - X[n]) / T_s$ in discrete form. T_s is the sampling time and n is the time index. It has been observed that using higher order approximations does not present much improvement over the first order discretization presented here. This may be attributed to the high robustness of the dynamics of the algorithm.

The state variables of the system of (5.6) can be envisaged in the spherical coordinate system of (A, ω, ϕ) . They can be rewritten as

$$\frac{dA}{dt} = -\mu_1 A \sin^2 \phi + 2\mu_1 \sin \phi u(t), \quad (5.7)$$

$$\frac{d\omega}{dt} = -\mu_2 A \sin(2\phi) + 2\mu_2 \cos \phi u(t), \quad (5.8)$$

$$\frac{d\phi}{dt} = \omega + \mu_3 \frac{d\omega}{dt}. \quad (5.9)$$

Let $u(t) = u_o(t) + u_1(t)$ where $u_o(t) = A_o \sin \phi_o(t)$ and $\phi_o(t) = \omega_o t + \delta_o$. The following theorem deals with the existence, uniqueness and stability of a periodic orbit for this dynamical system. The proofs are based on the Poincaré theorem and are presented in [5.28]. According to the Poincaré theorem, the behavior of the dynamical system near its periodic orbit can be investigated using a discrete map. The fixed points of this map correspond to the periodic orbits of the main dynamics and their stability types are equivalent.

Theorem 1. Let $u(t) = A_o \sin(\omega_o t + \delta_o) + u_1(t)$ where A_o , ω_o , and δ_o are real constants and $u_1(t)$ is an arbitrary T_o -periodic bounded continuous function, which has no frequency component at ω_o . With a proper choice of parameters $\{\mu_i, i = 1, 2, 3\}$, the dynamics described by equations (5.7) to (5.9) has a unique periodic orbit $\gamma(t)$ in (A, ω, ϕ) space in a neighborhood of $u_o(t) = A_o \sin(\omega_o t + \delta_o)$. This neighborhood is determined by the function $u_1(t)$ and the parameters μ_1 to μ_3 . Moreover, this periodic orbit is asymptotically stable. The periodic orbit coincides with $u_o(t)$ when $u_1(t)$ is not present.

The theorem indicates that there is a unique periodic orbit to which the system converges. This periodic orbit is located in a neighborhood of the ideal desired component. The tighter this neighborhood is, the more accurately the desired component is estimated. The extent of this neighborhood is determined by the level of “pollution” $u_1(t)$ and the step sizes μ_1 , μ_2 and μ_3 .

The small values for step sizes μ_1 and μ_2 result in a refined periodic orbit in a tight neighborhood. On the other hand, the step-sizes determine the speed of the convergence to the solution of the differential equations. As well, if the parameters in the input function (including amplitude and phase angle) vary with time, the desired solution will follow those variations provided that the speed of the convergence to the solution, determined by the step sizes, is sufficiently high. A trade-off, therefore, exists between the transient convergence speed and the steady state accuracy.

The dynamics of the algorithm presents a notch filter in the sense that it extracts (i.e. lets pass through) one specific sinusoidal component and rejects all other components including noise. It is adaptive in the sense that the notch filter accommodates variations of the characteristics of the desired output over time. The center frequency of such an adaptive notch filter is specified by the initial condition of frequency ω . In Fig. 5.4 this initial value, ω_0 , is explicitly shown for easy visualization.

In terms of the engineering performance of the system, this indicates that the output of the system will approach a sinusoidal component of the input signal $u(t)$. Moreover, time variations of parameters in $u(t)$ are tolerated by the system. Fig. 5.5 shows a snapshot of the performance of the algorithm when the frequency and amplitude of the input signal jump from 50 Hz to 100 Hz and 1 to 2, respectively. Initially, the periodic orbit is a circle with unit radius which lies on the horizontal plane of $f = 50$ Hz, then it flows to another circle with radius 2 which lies on the plane of $f = 100$ Hz.

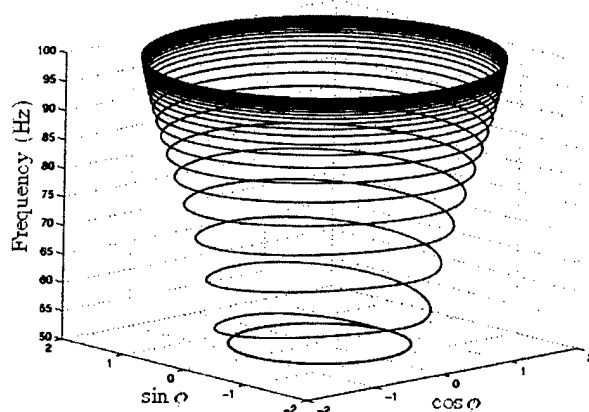


Fig. 5.4. Illustration of the performance of the algorithm when both the amplitude and frequency of the input signal undergo a jump of 100%.

One of the issues that need to be considered when using the algorithm is setting of its parameters μ_1 , μ_2 , and μ_3 . The values of the parameters μ_1 , μ_2 , and μ_3 determine the convergence speed versus error compromise. Specifically, parameter μ_1 controls the speed of the transient response of the algorithm

with respect to variations in the amplitude of the extracted sinusoid. Speed is traded off by the steady state error. As long as the frequency of the input signal is close to its nominal value (e.g. 60 Hz), this trade-off does not introduce a significant constraint. As the frequency of the input signal deviates from its nominal value, the algorithm introduces more significant trade-off between the speed and steady state error; for example, within a range of ± 2 Hz variations off nominal frequency, the algorithm can be adjusted to catch up a 100% step change in the amplitude of the desired sinusoid within 3 cycles with less than 2% steady state error. Parameters μ_2 and μ_3 mutually control the speed of the transient response of the algorithm with respect to variations in the frequency of the extracted sinusoid.

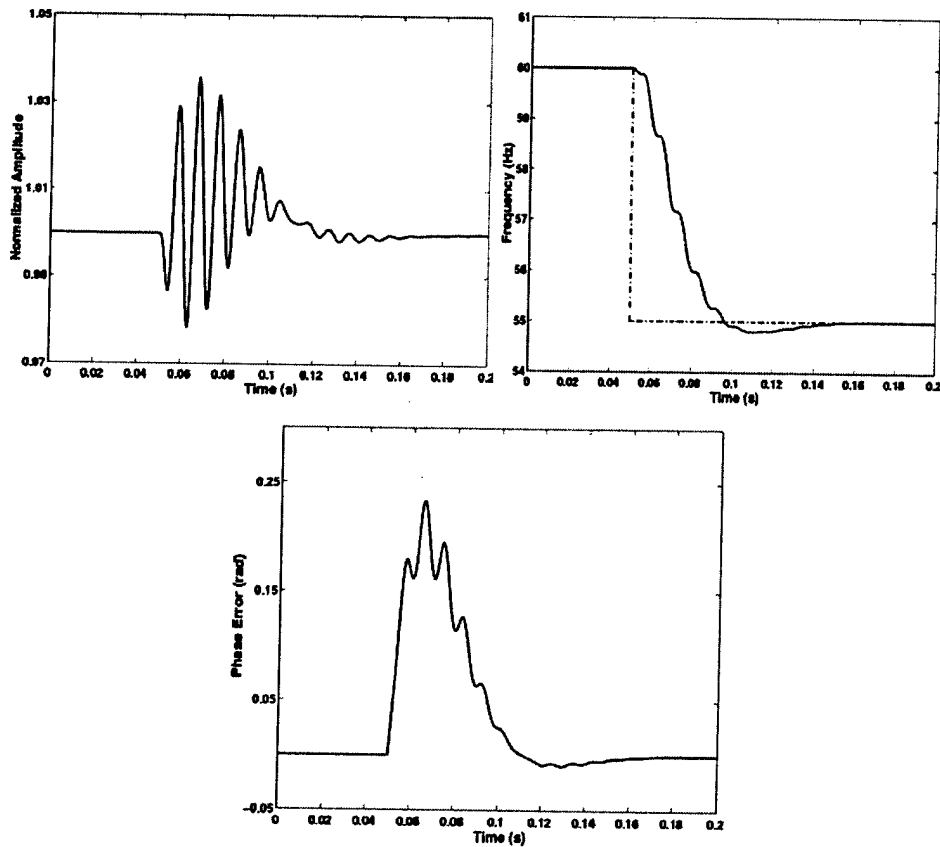


Fig. 5.5. Response of the algorithm to a step change in the frequency of the input signal. The sinusoidal component and all its parameters are tracked adaptively over time.

The larger the value of parameter μ_2 is chosen, the faster the convergence is achieved in tracking the phase (or frequency) variations over time. The cost is higher steady state error. Adjustment of the third tuning parameter, μ_3 , is interdependent on the adjustment of μ_2 . As a simple rule of thumb, one may pick a value for parameter μ_2 based on the potential frequency drift in the input signal (hence, the desired frequency tracking speed) first, and choose the value of μ_3 such that the product $\mu_2\mu_3$ becomes of the same order of

μ_1 for a balanced speed in terms of tracking the amplitude and total phase (or frequency).

In the simulations presented in this section, Matlab Simulink™ computational software is used as the main computational tool. Fig. 5.5 shows the performance of the algorithm for an example in which the frequency of the input signal undergoes a step change of 10%. It is observed that the variations are effectively tracked with a transient lasting just a few cycles. Values of the parameters are chosen to be $\mu_1 = 100$, $\mu_2 = 10000$ and $\mu_3 = 0.02$ for this simulation.

The algorithm is particularly efficient for real-time applications. To illustrate the real-time nature of the algorithm, an example having a distorted sinusoid as the input signal is considered. Fig. 5.6 shows the performance of the algorithm in the extraction of the amplitude and phase of the fundamental component of this distorted sinusoid. The distortion in this case is of a harmonic form with 30% of the third and 10% of the tenth harmonic. It is observed that the amplitude and phase of the fundamental component are estimated almost within two cycles. Unlike the Fourier-based techniques in which only estimates of the amplitude and constant phase are computed, the fundamental component itself is instantly generated and is available in real-time. This is due to the fact that the algorithm instantly generates the total phase ϕ rather than δ .

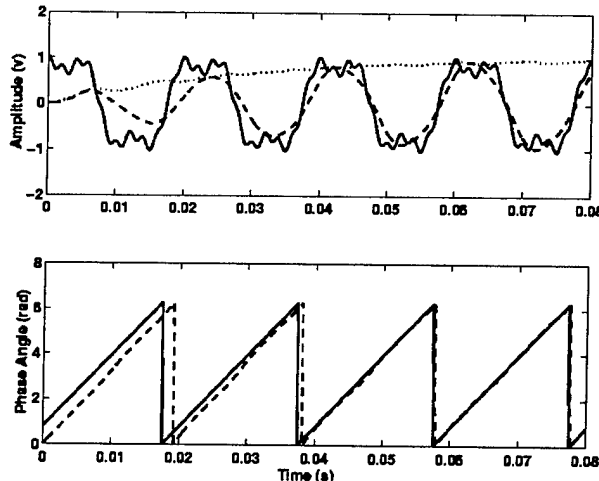


Fig. 5.6. Illustration of the performance of the algorithm in the extraction of the amplitude and phase of the fundamental component of a distorted sinusoid. Top: input signal (solid), extracted fundamental (dashed), and its amplitude (dotted). Bottom: actual (solid) and extracted (dashed) phase angles.

5.3 Application Of the Algorithm

The measured startup current transient of an 11kW induction motor is shown in Fig.5.7. Before implementing the algorithm, the individual measured line currents are transformed into a single rotating

current vector as shown in Fig. 5.8 [5.29]-[5.30]. The reason for combining the three line currents is that no two starting transients are exactly the same. The individual line currents will differ depending on instantaneous value of the line voltages at startup. When comparing the three line currents under different machine health conditions, it will be easier to compare a single rotating vector than three line currents that are not similar.

The vector is then transformed into the time domain and used as an input to the extraction algorithm. The algorithm estimates the frequency, amplitude and phase of the nonstationary fundamental as shown in Figs 5.38, 5.39 and 5.40. The fundamental component (which varies with magnitude, frequency and phase) can be extracted with this algorithm. This estimate is then subtracted from the input. The resulting waveform shown in Fig. 5.41 has information relating to the health of the machine including bad bearings, broken rotor bars etc.

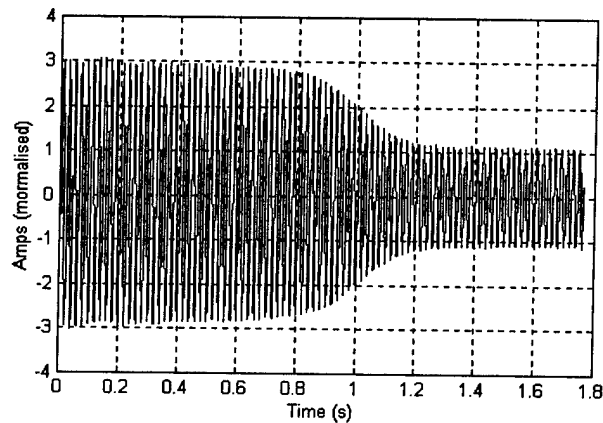


Fig. 5.7. The Startup current transient.

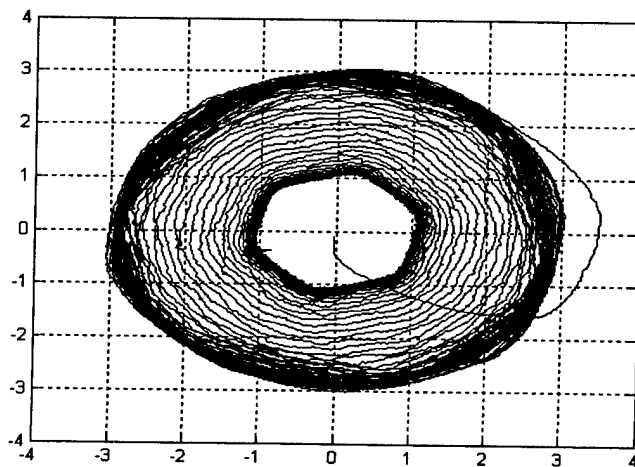


Fig. 5.8. A plot of the current vector.

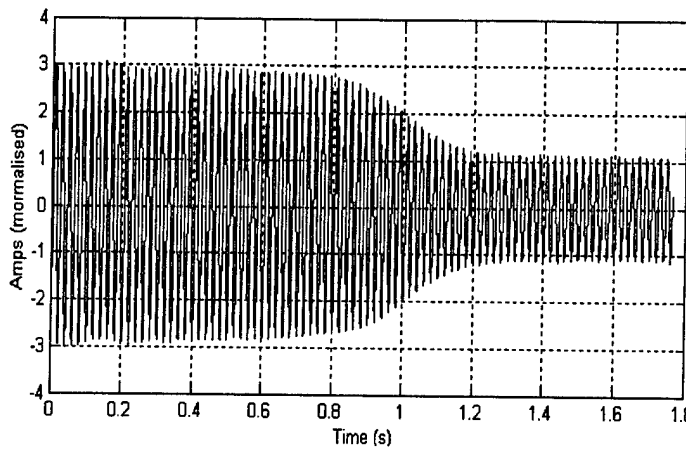


Fig. 5.9. The time domain representation of the current vector.

The algorithm takes a few cycles to converge to the amplitude and frequency of the fundamental. This is shown in Figs 5.10 and 5.12. As a result when the estimated fundamental is subtracted from the original waveform, the algorithm's output between 0 and 0.4 seconds should be discarded to allow for convergence.

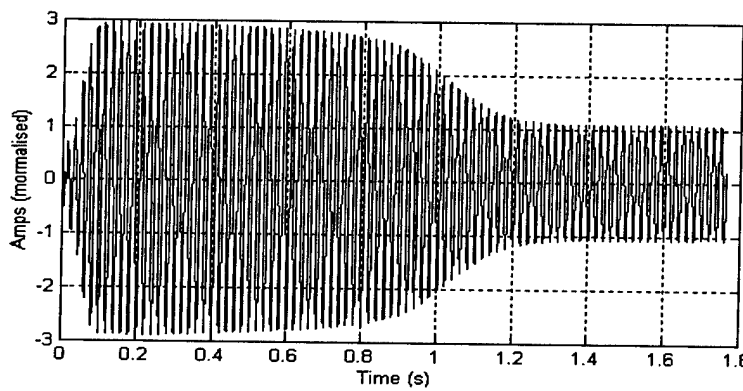


Fig. 5.10. The estimated fundamental startup current of the algorithm.

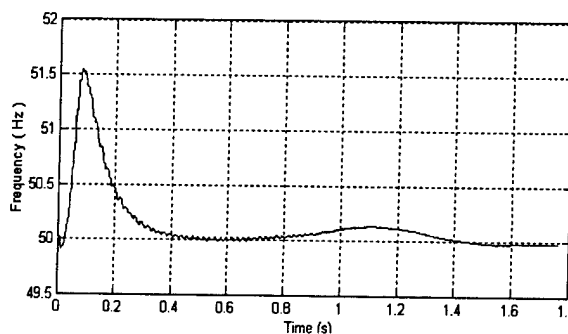


Fig. 5.11. Frequency of the algorithm.

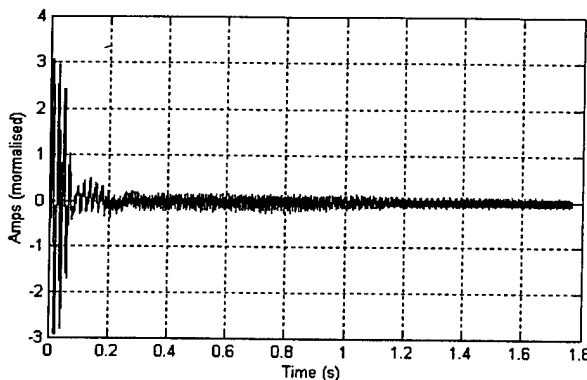


Fig. 5.12. The startup current after extraction of the fundamental.

Fig. 5.12 shows the estimated frequency of the fundamental. An accurate estimate of the frequency is only available after 0.4s.

5.4 The Detection Of Broken Rotor Bars

The algorithm was used to detect broken rotor bars in a $\frac{1}{2}$ hp induction motor. Two identical rotors were used in this experiment except that one had a broken rotor bar. The same bearings and stator was used in order to minimize their influences on the startup transients. The machine was tested under loading conditions varying from 30% to 100% to determine if this method of detection could be successful and independent of the loading conditions.

The current signals were captured using a PC based data acquisition system. The non-stationary fundamental was removed using the system in Fig. 5.3 and implemented using Matlab's Simulink. The residual currents were analyzed using Matlab's Wavelet Toolbox.

The discrete wavelet transform, using Daubechies 8 wavelet, was then applied to the residual current vector. Figs 5.11 and 5.12 show the 9th scale detail coefficients of both healthy and damaged machine under various loads. By inspection of Figs 5.13 and 5.14, two dominant features are present that characterize the condition of the machine. The first feature is found between samples 8 and 13 of all the loading conditions. This feature is present in both the healthy and damaged machine. The second feature found between samples 45 and 53 is only present in the case of the damaged machine. The second feature can be used to discriminate between a healthy and a damaged machine. An automated fault detection analyzer is envisioned based on this algorithm.

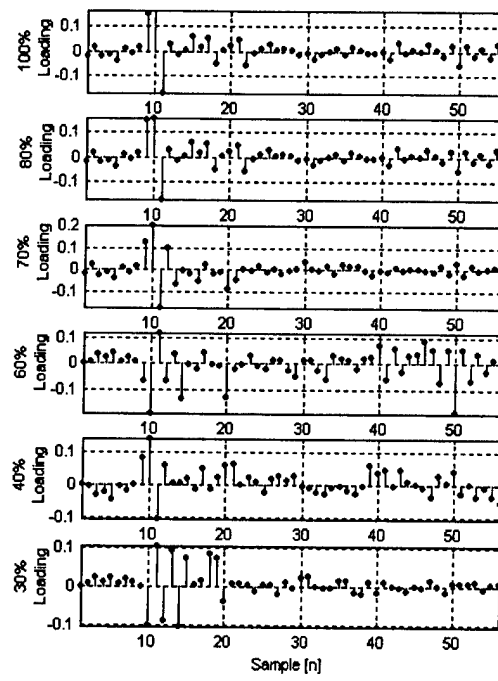


Fig. 5.13. Wavelet decomposition levels D9 of a healthy machine loaded 30% to 100%.

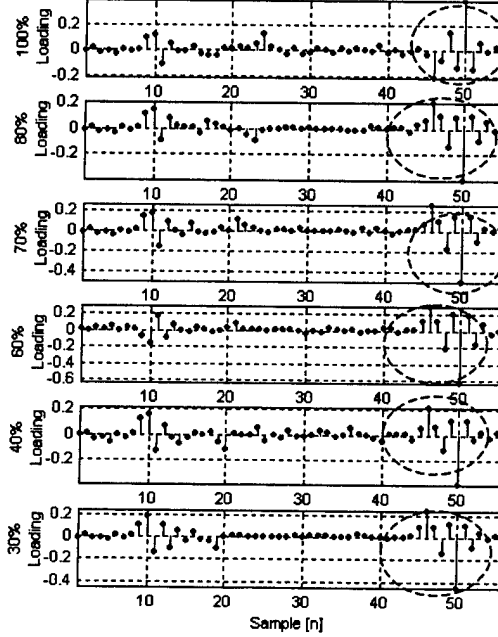


Fig. 5.14. Wavelet decomposition levels D9 of a damaged machine loaded 30% to 100%.

5.5 Conclusions

A new algorithm for use in transient motor current signature analysis has been introduced and applied to the detection of broken rotor bars in induction machines. The algorithm is able to extract a single non-stationary sinusoid embedded within a non-stationary waveform. This is then applied to the transient inrush current of an induction motor and a wavelet analysis is conducted on the balance of the current. Although results presented here are unique to the machine being diagnosed, the methodology applied to extracting the transient fundamental current and analysis of the residual currents is universal and can be applied to any machine.

The analysis clearly shows that the broken rotor bar can be detected using measured transient inrush currents. This method can be used for standard induction motors during startups as well as machines that operate predominantly in the transient like wind generators or motor operated valves.

5.5 References

- [5.1] G. B. Kliman and J. Stein, "Methods of motor current signature analysis," *Electric Machines and Power Systems*, vol. 20, no. 5, pp. 463-474, September, 1992.
- [5.2] W. Deleroi, "Broken bars in squirrel cage rotor of an induction motor—Part1: Description by superimposed fault currents," *Archiv fur Elektrotechnik*, vol. 67, pp. 91-99, 1984.
- [5.3] R. Hirvonen, "On-line condition monitoring of defects in squirrel cage motors," *Proceedings of the International Conference on Electrical Machines*, Paris, France, vol. 2, pp. 301-308, 1994.
- [5.4] M. E. H. Benbouzid and M. Vieira, "Induction motor fault detection and localization using stator current, advanced signal processing techniques," *IEEE Transactions Power Electronics*, vol. 14, no. 1, pp. 14-22, January 1999.
- [5.5] S. L. Ho, W. L. Chan and H. W. Leung, "Application of statistical signal processing for condition monitoring of rotor faults in induction motors," *Proceedings of the International Conference on Electrical Machines*, Oxford, England, pp. 97-102, 1993.
- [5.6] G. B. Kliman, "What stator current processing-based technique to use for induction motor rotor faults diagnosis?" *IEEE Transactions on Energy Conversion*, vol. 18, no. 2, pp. 238-244, June 2003.
- [5.7] W. T. Thomson and I. D. Stewart, "On-line current monitoring for fault diagnosis in inverter fed induction motors," *Proceedings of the Third International Conference on Power Electronics and Variable Speed-Drives*, London, England, pp. 66-73, 1994.
- [5.8] C. Hargis, "The detection of rotor defects in induction motors," *Proceedings of the IEE International Conference on Electrical Machines, Design and Application*, London, England, pp. 216-220, 1982.

- [5.9] M. E. H. Benbouzid, "A review of induction motors signature analysis as a medium for faults detection," *IEEE Transactions on Industrial Electronics*, vol. 47, no. 5, pp. 984-993, October 2000.
- [5.10] W. Deleroi, "Squirrel cage motor with broken bar in the rotor- physical phenomena and their experimental assessment," *Proceedings of International Conference of Electrical Machines*, Budapest, Hungary, pp. 767-770, 1982.
- [5.11] H. A. Toliyat, "Condition monitoring and fault diagnosis of electrical machines - A review," *Proceedings of the International Conference on Industry Applications*, Seattle, WA, vol. 1, pp. 197-204, 1999.
- [5.12] F. Filippetti, "AI techniques in induction machines diagnosis including the speed ripple effect," *IEEE Transactions on Industrial Applications*, vol. 34, pp. 98-108, January 1998.
- [5.13] M. Haji and H. A. Toliyat, "Pattern recognition - A technique for induction machines rotor fault detection," *Proceedings of the IEEE Electric Machines and Drives Conference*, Cambridge, MA, pp. 899-904, 2001.
- [5.14] P. Pillay and Z. Xu, "Motor current signature analysis," *Proceedings of the IEEE Industry Applications Annual Meeting*, San Diego, CA, vol. 1, pp. 587-594, 1996.
- [5.15] J. F. Watson and S. Elder, "Fault detection in induction motors as a result of transient analysis," *Proceedings of the Fourth International Conference on Electrical Machines and Drives*, pp. 182-186, 1989.
- [5.16] R. W. Schafer and L. R. Rabiner, "Design and analysis of a speech analysis-synthesis system based on short time Fourier analysis," *IEEE Transactions on Audio and Electro-acoustics*, vol. - 21, no. 3, pp. 165-174, June 1973.
- [5.17] D. C. Robertson, O. I. Camps, and J. S. Mayer, "Wavelets and power system transients: Feature detection and classification," *International Symposium on Optical Engineering in Aerospace Sensing*, vol. 2, pp. 474-487, 1994.
- [5.18] S. Santoso, E. J. Powers, and W. M. Grady, "Power quality assessment via wavelet transform analysis," *IEEE Transactions on Power Delivery*, pp. 924-930, vol. 11, no. 2, 1996.
- [5.19] P. Pillay and A. Bhattacharjee, "Application of wavelets to model short-term power system disturbances," *IEEE Transactions on Power Systems*, vol. 11, no. 4, pp. 2031-2037, October 1996.
- [5.20] A. W. Galli, G. T. Heydt, and P. F. Riberio, "Exploring the power of wavelet analysis," *IEEE Computer Applications in Power*, vol. 9, no. 4, pp. 37-41, October 1996.
- [5.21] P. Pillay, P. Ribeiro, and Q. Pan, "Power quality modeling using wavelets," *Proceedings of the International Conference on Harmonic and Quality of Power*, pp. 625-631, October 1996.
- [5.22] A. Gaouda and M. Salama, "Wavelet-based signal processing for disturbance classification and measurement," *IEE Proceedings, Generation, Transmission and Distribution*, vol. 149, no. 3, pp. 310-318, May 2002.

- [5.23] P. S. Meliopoulos and C. H. Lee, "Wavelet based transient analysis," *IEEE Transactions on Power Delivery*, pp. 114-121, vol. 15, no. 1. January 2000.
- [5.24] I. Daubechies, "Orthonormal bases of compactly supported wavelets," *Communications on Pure and Applied Mathematics*, vol. 41, pp. 909-996, 1988.
- [5.25] P. F. Ribeiro, "Wavelet transform: An advanced tool for analyzing nonstationary harmonic distortions in power systems," *Proceedings of the IEEE International Conference on Harmonics in Power Systems*, pp. 141-149, Sept. 1994.
- [5.26] S. G. Mallat, "A theory for multiresolution signal decomposition: the wavelet representation," *IEEE Transactions on Pattern Analysis and Machine Intelligence*, pp. 674-693, vol. 7, no. 11, July 1989.
- [5.27] A. K. Ziarani and A. Konrad, "A nonlinear adaptive method of elimination of power line interference in ECG signals," *IEEE Transactions on Biomedical Engineering*, vol. 49, no. 6, pp. 540-547, June 2002.
- [5.28] M. Karimi-Ghartemani and A. K. Ziarani, "Periodic orbit analysis of two dynamical systems for electrical engineering applications," *Journal of Engineering Mathematics*, vol. 45, no. 2, pp. 135-154, 2003.
- [5.29] A. J. M. Cardoso, "Computer-aided detection of airgap eccentricity in operating three-phase induction motors by Park's vector approach," *IEEE Transactions on Industry Applications*, vol. 29, pp. 897-901, September 1993.
- [5.30] M. E. H. Benbouzid, "Monitoring and diagnosis of induction motors electrical faults using a current Park's vector pattern approach," *IEEE Transactions on Industry Applications*, pp. 730-735, vol. 36, no. 3, 2000.

Chapter 6

Measurement of Surge Propagation in Induction Machines

6.1 Introduction

Winding failures in induction machines have been a major concern in the past several years, and more so recently with the addition of variable speed drives (VSDs). Both the introduction of the vacuum breaker, and the introduction of PWM drives, utilizing fast switching IGBT's, have resulted in an increase in winding failures in induction machines.

There are two mechanisms causing winding failures; steep-fronted surges, like those caused during the opening and closing of vacuum breakers, and transient overvoltages caused by impedance mismatch between cable and load during VSD operation. There has been a fair amount of work done to date on the propagation of vacuum breaker induced steep-fronted surges in the windings of large induction machines [6.5,6.6,6.8-6.14,6.16]. The majority of this work has focused on a single event surge entering one winding of a multiphase machine. In addition, the winding parameters have been limited to calculated values. Here the intention is to present a measurement technique for determining the motor parameters in different sections of the coil so that surge studies may be conducted. Attention is also paid to the mutual inductive and capacitance coupling between turns and the dependence of these parameters on frequency.

The machine under study is form-wound, hence parallel plate capacitance theory has been applied by other researchers for capacitance calculations as shown in figure 6.1.

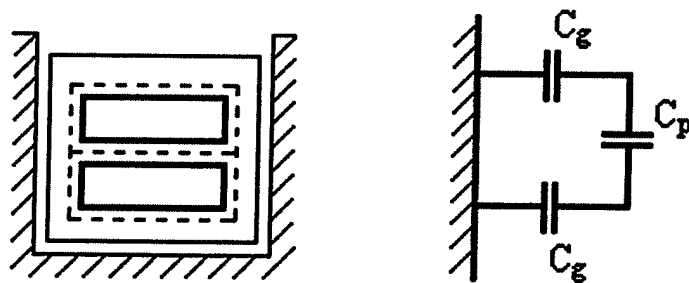


Figure 6.1. Capacitance in a 2-turn coil.

The individual values of C_g and C_p are calculated using parallel plate approximations and the ϵ_r value of the respective insulations. This can give reasonably accurate capacitance values. For inductance values, some have used finite element methods[8], but most have used the equation

$$[L] = [C_0]^{-1} / c^2 \quad (6.1)$$

where $[L]$ is the inductance matrix, $[C_0]$ is the capacitance matrix found as mentioned above with the exception that all $\epsilon_r = 1$, and c is the velocity of propagation [6.6]. This method requires knowledge of the velocity of propagation in the coils. One study [6.6], assumed the wave propagation velocity in the overhang section of the coil is the same as within the slot region. This assumption is not supported by [6.9] which report the velocity of propagation in the slot as been lower than in the overhang.

More recently, work has been progressing on overvoltages at the machine terminals as a result of VSD's operating with long cables connecting drive and machine [6.1-6.4]. The long cables have impedances significantly different from the impedance of the induction machine. When a steep fronted wave traveling along the cable encounters the impedance mismatch a voltage reflection occurs resulting in an overvoltage at the location of the mismatch, i.e. the machine terminals. As switching frequencies increase so do the rise times on the devices, translating into a higher dv/dt pulse/wave traveling down the cable. The higher the dv/dt the steeper the wave front impacting the impedance mismatch. Thus, peak overvoltages increase as the rise time of semiconductor devices reduces [6.1]. The result is that voltage reflections are dependent on VSD output pulse rise time and cable length.

The work further focuses on the measurement of surge propagation differentiating between the impedance of the slot sections and that of the overhang sections, of each turn. Detailed parameter measurements are made of each turn section (slot vs. overhang), which are then used to determine the surge impedance of each section. Reflection and refraction coefficients are calculated, which can then be used to map, via lattice diagrams, the propagation of surges within the turns of one coil.

The paper is divided into seven sections. The first is a review of the problem. Second, discusses the parameter measurements and the method used to obtain the measurements. Third, experimental set up for surge measurements. Fourth, single section lattice diagram simulation and measurement. Fifth, the Bewley lattice diagram is extended to map all sections of a coil within the induction machine. Sixth, PWM pulse tracking within the turns of a coil using a lattice diagram. Finally, the conclusions are presented.

6.2. Parameter Measurements

The stator coils sit in slots, where the coils are surrounded on three sides by iron; in the overhang the coils are surrounded by air only. These two distinctly different environments cause the coils to have different surge impedances. For the slot region, because of the presence of the iron the inductance is much higher than for the overhang region. The effect on the capacitance is also greater in the slot, than in the overhang

where the only coil coupling is to the adjacent coil. These regions become important when steep-fronted surges attempt to pass between them. An incident surge will experience reflections, refractions and cause overvoltages at impedance mismatches.

There are also mismatches at the phase terminals, where the connection from the terminal meets the coil. The coil can be divided into six distinct regions of differing impedances. Since the wave front duration is much shorter than the coil propagation time each turn acts as a separate conductor, even though they are connected to one another. However, this only holds during the transient period of a few microseconds. Because of this, a coil can be modeled like a multiconductor transmission line [6.8-6.10,6.16] with many series segments consisting of slot sections and overhang regions. The theories of wave propagation on multiconductor transmission lines can be applied to the coils of a machine. Figure 6.2 shows a diagram of a three-turn coil segmented into five regions, with slot and overhang regions marked.

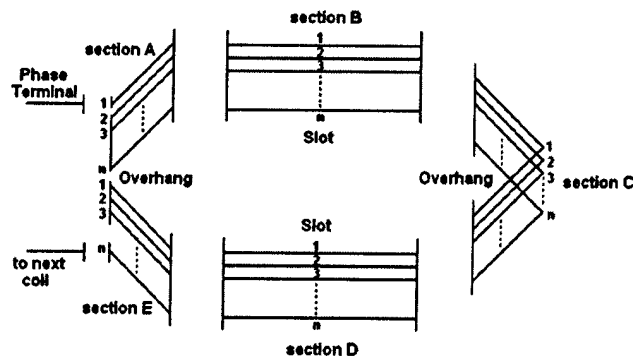


Figure 6.2. Multiconductor transmission model of induction motor coil with series sections.

In previous work done, the capacitance and inductance values for the different regions were calculated. In this work the coil parameters are measured. A 150 hp, 3-phase, form wound induction machine was obtained for use as the test motor. To perform the required measurements the machine was disassembled down to the stator and frame, with only the coils left in place, as shown in figure 6.3. It has been shown in previous work [6.5,6.6,6.8,6.9,6.11] that it is not necessary to have the rotor present when performing experimental research on surges within the stator windings.

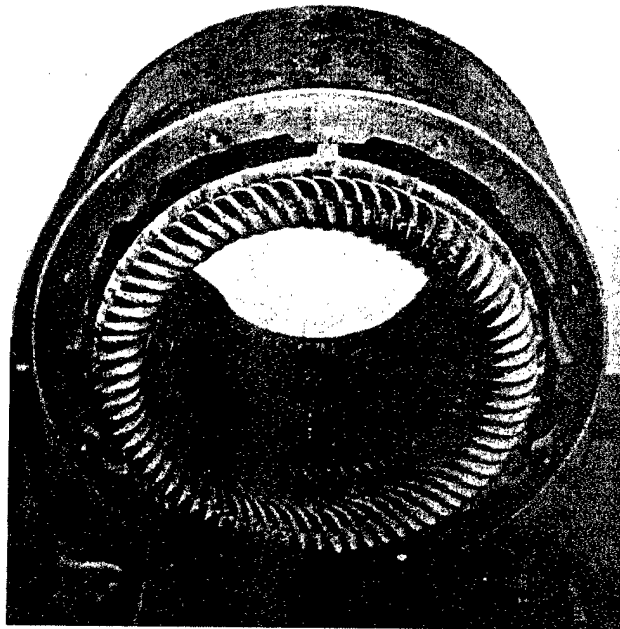


Figure 6.3. 150 HP, 3-phase, form wound induction motor used as test motor.

In addition because of the air gap the effect of the rotor on the parameter measurements is negligible. Several coil sections were removed to gain clear access to the stator core from each end for measurement purposes. Figure 6.4 shows one complete coil as removed from the machine.

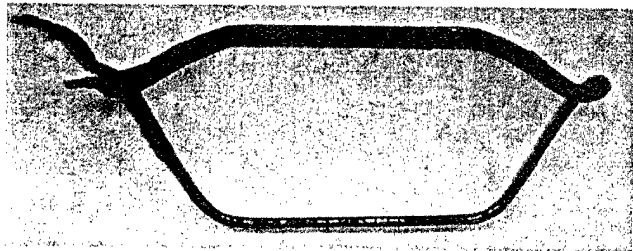


Figure 6.4. Shows one coil after being removed from the stator.

Five regions in each coil are identified as having different impedances from one region to the next. However, this does not necessarily imply that there are five different sets of parameters to measure. The two slot sections (B and D figure 6.2) of each coil will be considered the same, as they are the same size and composed of the same materials. Likewise, overhang sections A and E, figure 6.2, are the same with the exception of their incoming and outgoing connections. To obtain each section's parameters the coil must be cut into the respective regions and each placed back into its working environment. Figure 6.5 shows the actual test machine coil cut into the sections representing the different impedance values as shown in figure 6.2.

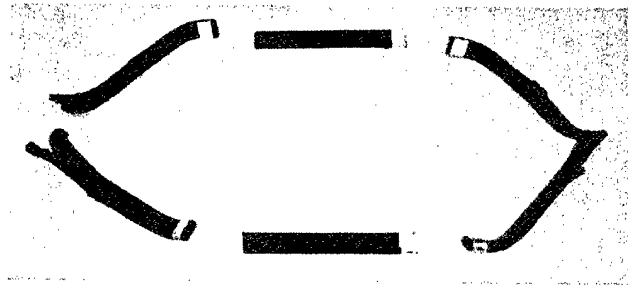


Figure 6.5. Test coil cut into sections representing different zones of impedance.

The parameter values were obtained using a Hewlett Packard (HP) 4284A 20Hz-1MHz Precision LCR Meter. Due to the size of the machine the standard leads for measurement, supplied with the LCR meter, were not able to be used. Even though a custom (non-calibrated) set of test leads were used the LCR meter had a correction capability via open circuit and short circuit tests to remove any errors introduced. A test setup was built to perform the capacitance measurements in the slot sections, which were placed back into the stator core. Figure 6.6 shows the capacitive setup. The capacitive measurements required only two contact points between the LCR meter test leads and the device under test (DUT). For the mutual, turn to turn inductances the test set up was modified to allow for four contact points to obtain the measurements. Also each contact point had to be independently movable to enable the complete set of turns to be measured. The test setup is shown in figure 6.7, while an inductance measurement is shown in figure 6.8.

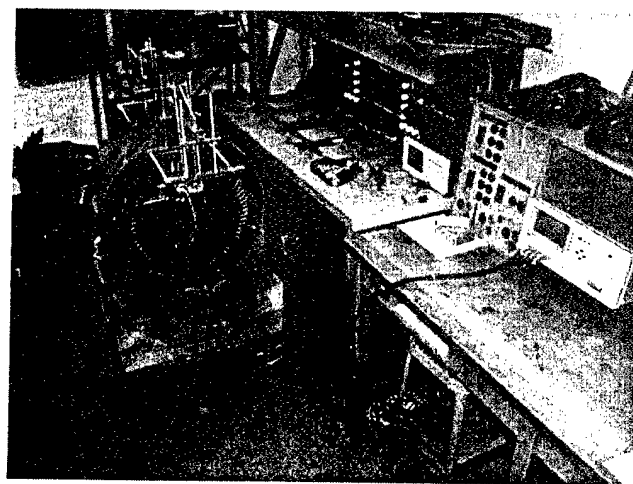


Figure 6.6. Test setup to measure capacitance in slot sections.

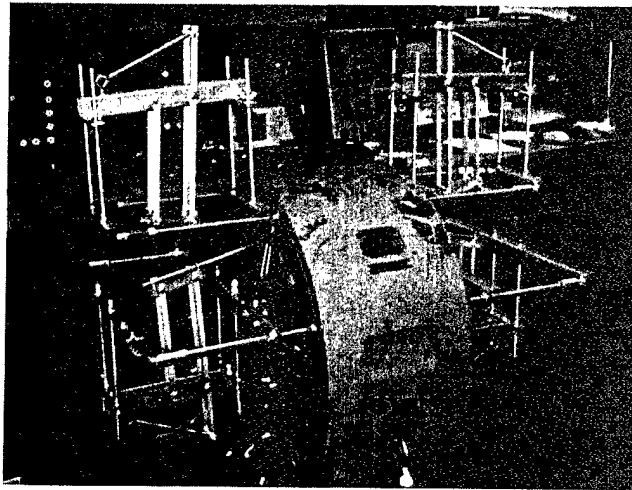


Figure 6.7. Test setup to measure inductance in slot sections.

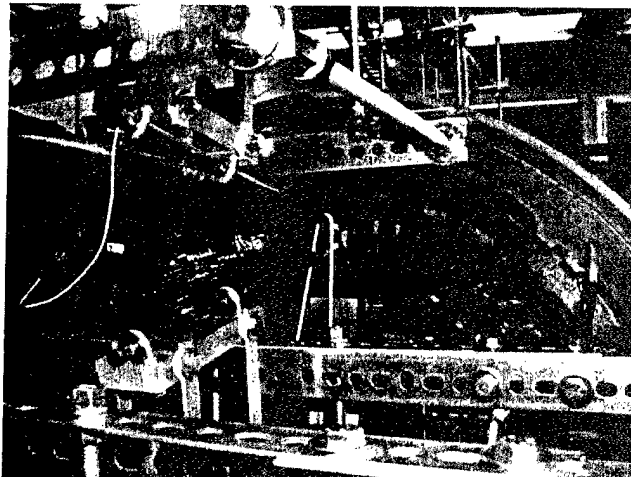


Figure 6.8. Inductance measurement of slot section of coil.

With these two setups, all turn to ground capacitances, turn to turn capacitances, self inductances and mutual inductances were measured for each conductor/turn in both the lower and upper coils in the double layer winding. As frequency plays an important role in impedance values all parameter measurements were taken over a range of frequencies from 60Hz to 1MHz in ten steps, as limited by the LCR meter. The ten frequencies used were 60Hz, 120Hz, 500Hz, 1KHz, 5KHz, 10KHz, 50KHz, 100KHz, 500KHz and 1MHz.

The process was repeated for the overhang sections. A jig was constructed, matching the inside shape of the stator core on to which the overhang sections were mounted. From detailed, full scale drawings, templates were made to hold the coil sections in their proper alignment. The complete jig with coil sections installed is shown in figure 6.9. Adjacent coils need to be in placed to account for mutual coupling as well

as surge propagation from coil to coil and the impedance mismatch between coils. The adjacent phase groups must also remain in place for phase to phase coupling, as the problem occurs during normal operation. Previous research has only examined one phase.

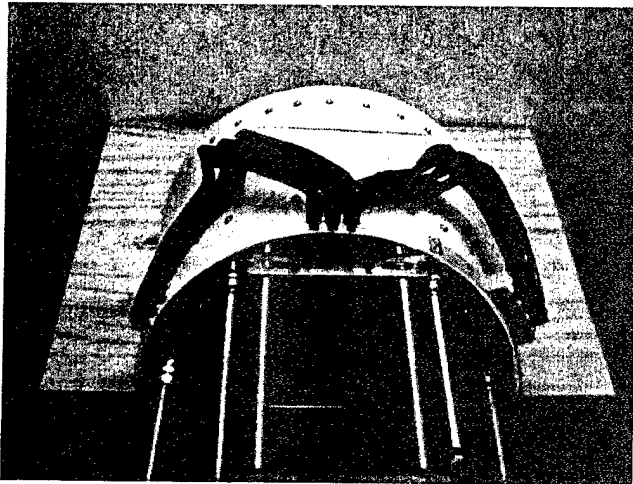


Figure 6.9. Form to hold overhang sections in proper alignment.

As with the slot setup, an additional support structure was needed to hold the test leads in place on the conductors while the measurements were taken. This additional structure needed to be completely and independently adjustable for each of the four contact points from test lead to the conductor being measured. Figure 6.10 shows the complete test setup to perform capacitance and inductance measurements on the overhang sections of the coils. Figure 6.11 shows a mutual inductance measurement being conducted on one of the overhang coil sections. In the slot measurements, only turn to turn and turn to ground couplings associated with the two coils residing in the slot were considered as the stator core acts as a barrier to coupling with coils in adjacent slots. Since the machine used in the experimental tests and measurements is double layer, both upper and lower coils have to be considered. Within the slot region, since both coils are parallel, a significant coupling exists between the two coils. However, in the overhang, due to the nature of the double layer winding, the upper and lower coils do not run parallel they run in opposite directions. There is only minimal overlap at the exit of the slot before turning in opposite directions. This would allow minimal coupling between upper and lower coils, and is supported by the measurements. The measured values show the coupling at a significantly low value as to be neglected.

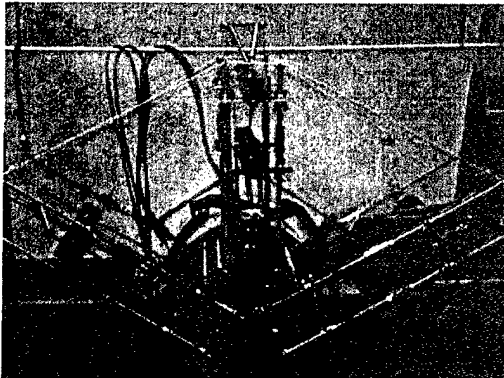


Figure 6.10. Test setup to measure capacitance and inductance in overhang.

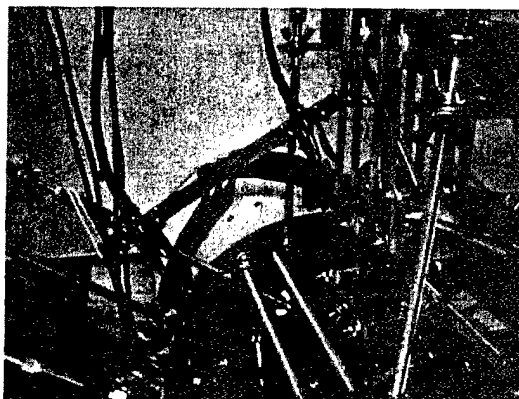


Figure 6.11. Inductance measurement of overhang section of coil.

It is necessary, for determining the characteristic impedance of the turn sections, to have the parameter values in units per meter. Hence, all measured data was divided by its respective conductor length, 0.3842m for the overhang region and 0.1619m for the slot. Figure 6.12 shows the self inductance of all 16 conductors (8 per coil) of the double layer winding for both the overhang and the slot regions in frequencies from 500Hz to 1Mhz. The left half of the figure shows the overhang values 1 to 16 (left to right), while the right half show the slot region, 1 to 16 (left to right). It can be seen in Figure 6.12 that in the overhang section of the coil, where the conductors are surrounded by air, that the self inductance is fairly equal among all turns and is somewhat constant as frequency increases. However, in the slot section of the coil, where the conductors are surrounded by iron, the self inductance varies greatly depending on the position of the conductor in the coil as well as with the frequency.

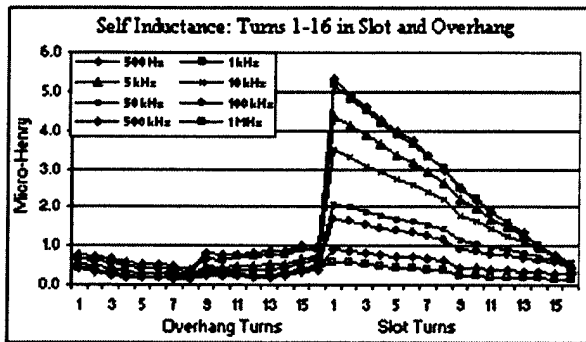


Figure 6.12. Measured self inductance of turns in overhang sections (left half) and in slot sections (right half).

Figure 6.13 shows a comparison of the self inductance in the overhang turns versus that in the slot for a frequency of 500Hz (same data as used in figure 6.12). The slot values show a linear decrease from turn one in the bottom of the slot to turn 16 at the top (nearest to rotor), as expected, while the overhang shows a reasonably constant value. This is for the same reason given above, in the slot the flux couples through the iron and for each turn has more distance to travel in the iron path. Whereas, for the overhang the coupling is through air and the adjacent turn thus the flux path is more uniform among the turns.

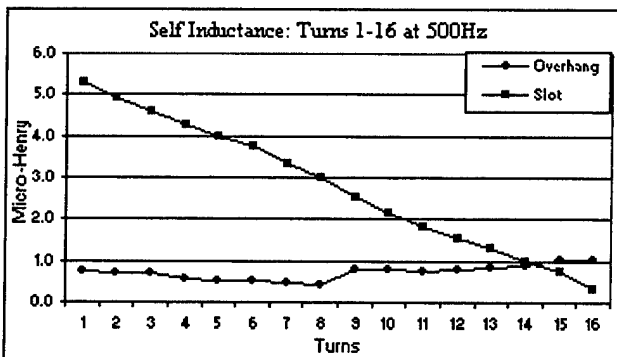


Figure 6.13. Comparison of self inductance in overhang vs. slot at 500Hz.

Figure 6.14 shows that as frequency increases the inductances within the slot regions converge. This is expected, as the frequency increases the flux penetration into the iron becomes less and must travel more within the slot region and the adjacent turns yielding a lower inductance value and a more uniform path among the turns, hence the convergence of the values for each turn.

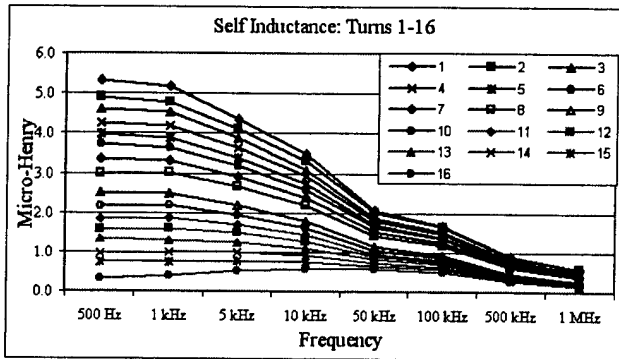


Figure 6.14. Self inductance in slot converging as frequency increases.

Figure 6.15 shows turn to adjacent turn capacitance in both the slot sections and overhang sections, for frequencies of 60 Hz to 1 MHz. The left half shows the slot measurements for both the lower and upper coils. The sharp drop is associated with the last turn of the lower coil and the first turn of the upper coil, where additional insulation is present. The overhang capacitance values (right half) are significantly lower than for the slot at all frequencies. This occurs because in the overhang the turn to turn capacitance only occurs between the parallel “primary” faces of the conductors, whereas in the slot, because of the close proximity of the iron core, the perpendicular faces (sides of the conductors) become part of the turn to turn capacitance as a “secondary” capacitance in parallel with the primary.

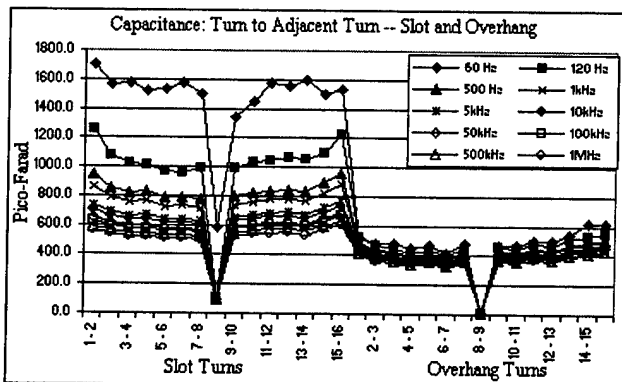


Figure 6.15. Measured turn to adjacent turn capacitance in slot sections (left half) and in overhang sections (right half).

Figure 6.16 shows as frequency is increased the slot capacitance values decrease and trend towards a constant value at high frequency. The turn to ground capacitance in the slot region also decreases as frequency increases but at a lesser rate than for the turn to turn values, as seen in figure 6.17.

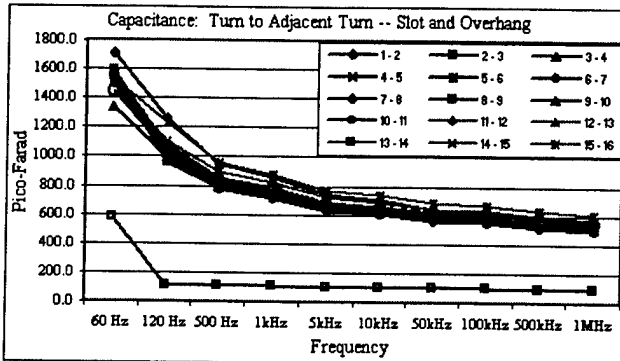


Figure 6.16. Turn to adjacent turn capacitance in slot converging as frequency increases.

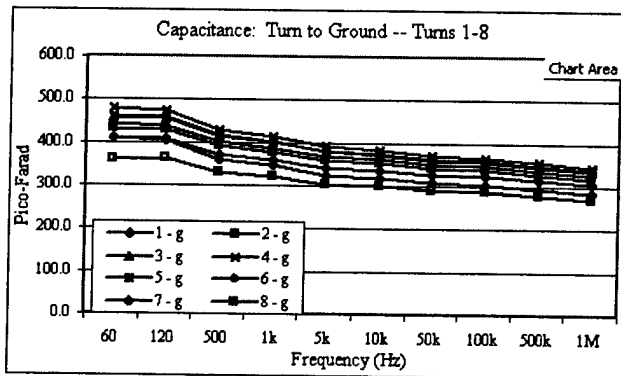


Figure 6.17. Turn to ground capacitance versus frequency in slot.

6.3. Experimental Setup For Surge Measurements

To obtain experimental results a test set up was assembled. The two main components necessary were a source of steep fronted waves and a device to accurately measure the source and the propagating waves. For the source, two choices of function generators were used. A Tektronix FG 503 3MHz function generator, which had a slower rise time of 54 nsec on a pulse train waveform. The second was an Hewlett Packard 3314A function generator, which had a faster rise time of 5.2 nsec. Both generators had internal impedance values of 50Ω .

For waveform measurements two CompuScope 85G waveform digitizers were used. Each device has two input channels having 5 GS/s A/D Sampling simultaneously, with 500 MHz bandwidth and 8 bit resolution. This level of measurement capture was necessary due to the short rise times of the source, as well as the short propagation times of the coil sections. The sampled data was viewed and stored using GageScope Oscilloscope Software.

To obtain measurements of waveforms at impedance boundaries within the coil, modifications were made to allow connections from the digitizers to the coil. At the location of a boundary change, i.e. slot to overhang, the insulation was removed and small leads attached, as seen in figure 6.18.

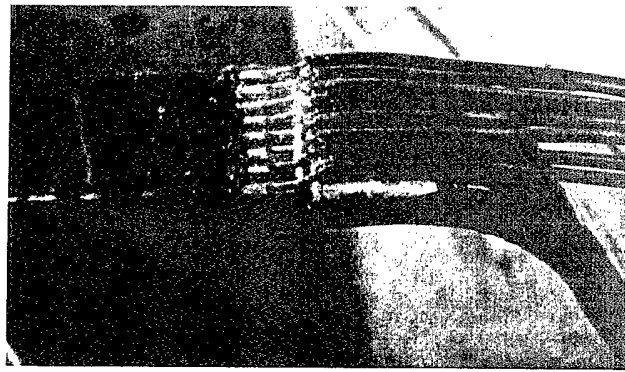


Figure 6.18. Leads attached to coil for waveform measurement.

6.4. Single Section Lattice Diagram

To verify the operation of the experimental setup a simple system with conductors of known impedance values and propagation times was examined, figure 6.19. To the left of point 'A' is the source, with internal impedance, connected to a 50Ω coaxial cable. At point 'A' the cable connects to channel 1 of the digitizer, set to an impedance of 50Ω . A second, longer length, coaxial cable is

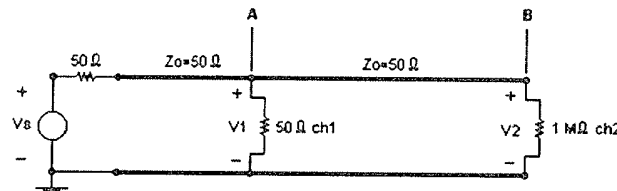


Figure 6.19. Simple experimental system.

connected from channel 1 to channel 2, where channel 2 is set to an impedance of $1 \text{ M}\Omega$, making an impedance mismatch with the cable. There is also a mismatch in impedance with point 'A' and the coaxial cable. Thus points 'A' and 'B' were used as the boundary points for a single section Bewley [6.15] lattice diagram analysis.

Since the rise time of the source is long compared to the propagation time of the cables, a stepped approximation of the rising edge, shown in figure 6.20, is used for evaluation of the wave front at the boundaries. Figure 6.21 shows the lattice diagram of reflections occurring between boundaries 'A' and

'B'. There are several lines, shifted in time, propagating simultaneously as a group representing the stepped edge approximation shown in figure 6.20. Figure 6.22 shows the resulting waveforms at points 'A' and 'B' for a simulated 1.5 per unit generated pulse. The voltage at point 'A' initially rises to 1v per unit and propagates down the cable to point 'B' where it encounters the $1M\Omega$ impedance and reflects the full voltage becoming 2v per unit and propagating back towards point 'A' where it is again reflected but with a lower value. The process repeats approximately five cycles before settling at a steady state value of 1.5v per unit, equal to the initial pulse value.

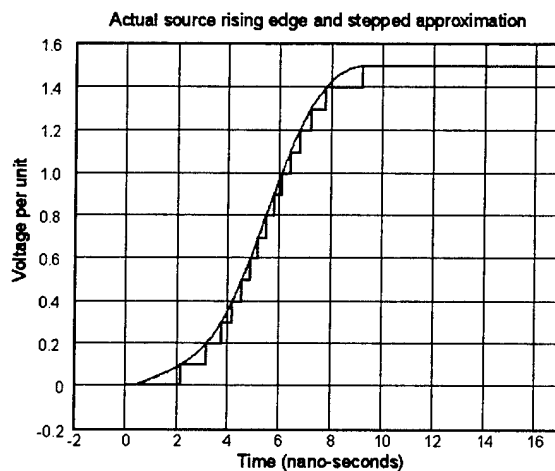


Figure 6.20. Stepped approximation of source rising edge.

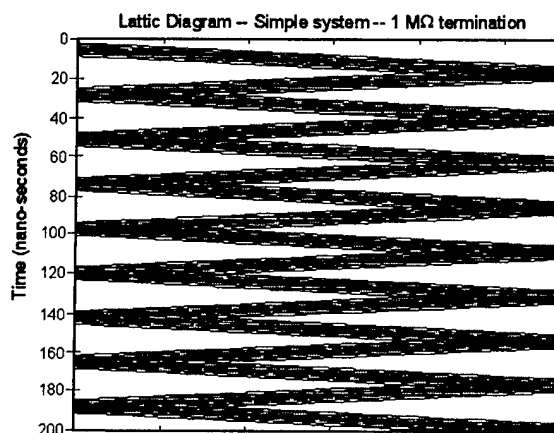


Figure 6.21. Lattice Diagram of simple system.

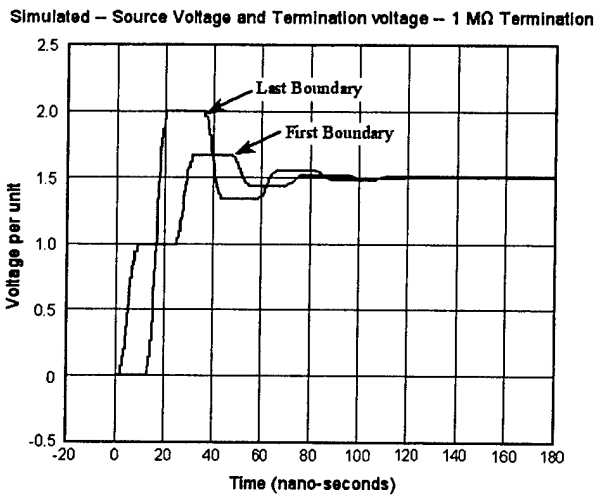


Figure 6.22. Simulation results at points 'A' and 'B'.

Figure 6.23 shows the measured waveforms for the actual 1.5 per unit pulse, where the voltage follows the same pattern as with the simulated system. The simulation results match up accurately to the measured values verifying the functionality of the experimental set up.

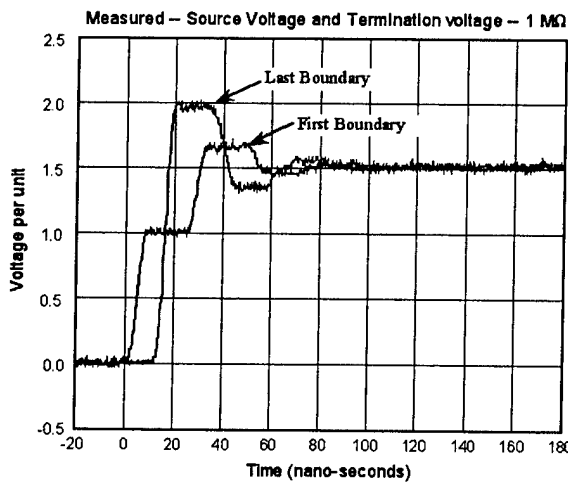


Figure 6.23. Measured results at points 'A' and 'B'.

6.5. Multiple Lattice Diagrams

With the coil parameters obtained, the impedance values associated with the coil sections were determined. These values were then used to determine the reflection and refraction coefficients associated with the boundaries between regions of differing impedance, i.e. slot to overhang. With reflection and refraction coefficients Bewley lattice theory[6.15] is used to map the propagation of a pulse/surge through the turns of a coil.

The machine under test has four turns per coil, with two conductors per turn, a total of 8 conductors per coil. Here the two parallel conductors are modeled into one conductor having the appropriate impedance value. Initially only one coil is examined under surge conditions. With no inter coil connections both overhang sections are modeled having the same impedance values, with the exception of the connection to the source cable which is handled separately. One complete turn includes four regions of impedance mismatch, slot 'A' – overhang 'A' – Slot 'B' – overhang 'B'. Hence, the lattice diagram must have four regions, each representing an impedance region of the coil. As each subsequent turn passes through the same four regions in sequence the lattice is further expanded to have 16 distinct regions. A seventeenth section representing the lead in, half overhang section, at the beginning of the coil is added, which has the same impedance value as a full overhang section. These 17 sections represent the complete coil. As the coil must be connected to a source via a cable, an eighteenth region is added to the front of the lattice. Figure 6.24 shows the multiple lattice diagram to track pulse propagation through the coil as each discontinuity is reached.

A program using MATLAB was written to evaluate the pulse, the boundary conditions, reflections, refractions, traveling waves and voltages occurring at each location of impedance mismatch. Figure 6.24 is the lattice result for a test simulation on a simplified coil model, in which the effects of mutual inductive and mutual capacitive coupling were not included. Figure 6.25 shows the tracking of voltage versus time occurring at the first boundary. Also shown in figure 6.25 is the source voltage as reference. The voltage at all eighteen boundaries are determined and shown in figure 6.26, while only the first and last boundary results are shown in figure 6.27.

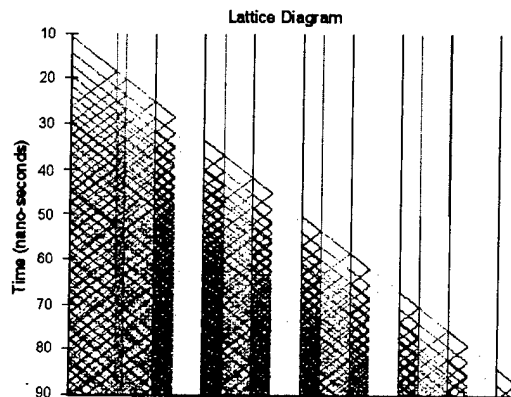


Figure 6.24. Lattice diagram of 4 turn coil differentiating slot sections from overhang sections, with a supply cable section first.

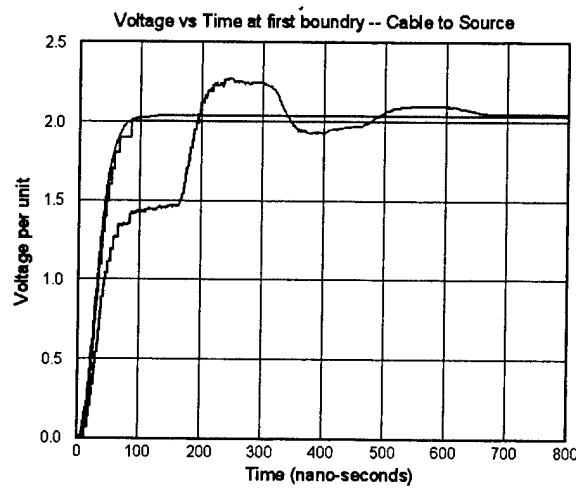


Figure 6.25. Voltage vs. Time diagram for the first boundary condition.

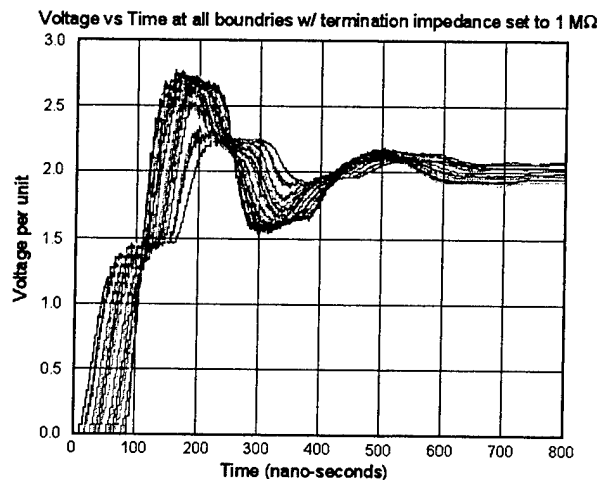


Figure 6.26. Voltage vs. Time diagram for all 18 boundaries.

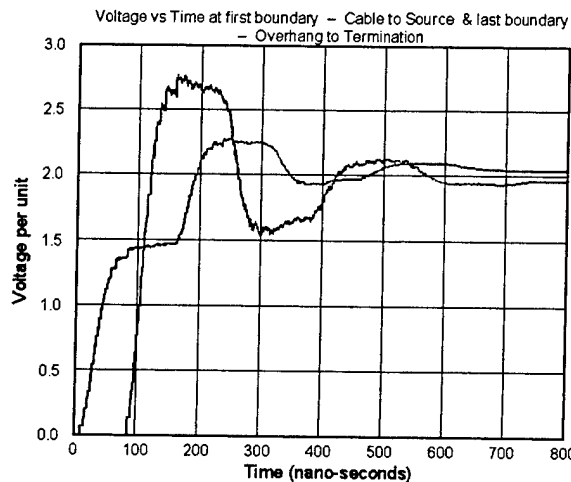


Figure 6.27. First and last boundary voltages.

6.6. PWM Pulse Tracking

With single pulse tracking completed, the MATLAB program will be modified to accept variations in the source. A PWM source is added to supply a train of pulses to the coil. The lattice diagram tracks multiple pulses traveling in time at the impedance boundaries. With several pulses entering the coil and being reflected and refracted along with the variations in velocity of propagation from one turn section to another, there is a much greater chance that several reflections will arrive at a boundary simultaneously causing greater overvoltages than predicted in earlier works.

Further use of the PWM lattice program allows the variation in PWM strategies to be tested, identifying which are most benign to the coil insulation.

6.7. Conclusions

This work makes contributions on the measurement of motor parameters for surge propagation studies. A single coil of the machine is divided into regions of differing impedance namely the slot and the overhang regions. Detailed parameter measurements are made of each turn within each region, to include turn to ground and turn to turn capacitance and self and mutual inductances. This is then used to determine the surge impedance of each section. Bewley lattice theory is extended to track surge propagation within the coil. Boundary voltages located at the impedance mismatch are calculated to determine the magnitude of the overvoltages occurring within each turn of a coil. Future work will focus on PWM interaction inside the windings.

References

- [6.1] Tianting Ren, "Analysis of Voltage Source Inverters Operating With Long Cables", M.S. Thesis, Clarkson University, 1997
- [6.2] R. J. Kerkman, D. Leggate and G. L. Skibinski, "Interaction of Drive Modulation and Cable Parameters on AC Motor Transients", *IEEE Transactions on Industry Applications*, Vol. 33, No. 3, May/June 1997, pp 722-731
- [6.3] A. Von Jouanne, D. A. Rendusare, P. N. Enjeti and J. W. Gray, "Filtering Techniques to Minimize the Effect of Long Motor Leads on PWM Inverter-Fed AC Motor Drive Systems", *IEEE Transactions on Industry Applications*, Vol. 32, No. 4, July/August 1996, pp 919-926
- [6.4] A. H. Bonnett, "Analysis of the Impact of Pulse-Width Modulated Inverter Voltage Waveforms on AC Induction Motors", *IEEE Transactions on Industry Applications*, Vol. 32, No. 2, March/April 1996, pp 386-392
- [6.5] P. G. McLaren and M. H. Abdel-Rahman, "Modeling of Large AC Motor Coils for Steep-Fronted Surge Studies", *IEEE Transactions on Industry Applications*, Vol. 24, No. 3, May/June 1988, pp. 422-426
- [6.6] M. T. Wright, S. J. Yang and K. McLeay, "General theory of fast-fronted interturn voltage distribution in electrical machine windings", *IEE Proceedings*, Vol. 130, Pt. B, No. 4, July 1983, pp. 245-256
- [6.7] L. M. Wedepohl, "Application of matrix methods to the solution of traveling wave phenomena in polyphase systems" *IEEE Proceedings*, Vol. 110, No. 12, December 1963, pp. 2200-2212.
- [6.8] P. G. McLaren and H. Orace, "Surge Voltage Distribution in Line-End Coils of Induction Machines", *IEEE Transactions on Power Apparatus and Systems*, Vol. PAS-104, No. 7, July 1985, pp. 1843-1848

- [6.9] K. J. Cornick and T. R. Thompson, "Steep-Fronted Switching Voltage Transients and Their Distribution in Motor Windings Part 2: Distribution of Steep-Fronted Switching Voltage Transients in Motor Windings", *IEE Proceedings*, Vol. 129, pt. B, No. 2, March 1982, pp. 56-63
- [6.10] K. J. Cornick and T. R. Thompson, "Steep-Fronted Switching Voltage Transients and Their Distribution in Motor Windings Part 1: System Measurements of Steep-Fronted Switching Voltage Transients", *IEE Proceedings*, Vol. 129, pt. B, No. 2, March 1982, pp. 45-55
- [6.11] W. W. L. Keerthipala and P. G. McLaren, "A Multiconductor Transmission Line Model for Surge Propagation Studies in Large A.C. Machine Windings", *Midwest Symposium on Circuits and Systems*, V2, August 12-15, 1990, pp. 629-632
- [6.12] W. W. L. Keerthipala and P. G. McLaren, "The Effects of Laminations on Steep Fronted Surge Propagation in Large A.C. Motor Coils", *IEEE Transactions on Energy Conversion*, Vol. 5, No. 1, March 1990, pp. 84-90
- [6.13] P.G. McLaren and M. H. Abdel-Rahman, "Steep Fronted Surges Applied to Large AC Motors - Effect of Surge Capacitor Value and Lead Length", *IEEE Transactions on Power Delivery*, Vol. 3 No. 3, July 1988, pp. 990-997
- [6.14] J. L. Guardado and K. J. Cornick, "Calculation of Machine Winding Electrical Parameters at High Frequency for Switching Transient Studies", *IEEE Transactions on Energy Conversion*, Vol. 11 No.1 March 1996, pp. 33-40
- [6.15] L. V. Bewley, "Traveling Waves On Transmission Systems", Dover Edition, Dover Publications, Inc. New York, 1963
- [6.16] H. Oraee, "Propagation of Surges in Stator Winding of Large AC Motors", Mediterranean Electrotechnical Conference, 1989 Proceedings: 'Integrating Research, Industry and Education in Energy and Communication Engineering', MELECON '89, Lisbon Portugal, April 11-13, 1989, pp. 138-141

Chapter 7

The Application Of Wavelets to Shipboard Power System Protection

7.1 Introduction

The Integrated Power System (IPS) is ungrounded to allow operation during faults yet cable capacitance and filters provide stray paths to the ship's hull. The fault current is very low for a single line to ground fault in an ungrounded system and the line to line and phase voltages are unchanged. This ensures a high continuity of service which is the Navy's motivation for installing ungrounded systems in ships. These systems are however subject to high transient overvoltages to ground and consequently are a potential hazard to equipment and personnel. These faults also cause insulation stress and lead to failures and more severe faults [7.1-7.5].

In this report the output line to line voltages are used as the medium for fault detection. A line to ground fault is defined as a single connection between an output phase voltage and the ship's hull. PSPICE is used to generate the line to line voltage data for the various faulted conditions. The data is then imported to MATLAB where the fundamental is removed. A wavelet analysis is applied to the residual voltages [7.6-7.15]. The coefficients of the detailed levels are examined for fault detection.

7.2 PSPICE Simulation

The IPS consists of a 3-phase generator, 3phase transformer, bridge rectifier, a one quadrant chopper and a three-phase inverter as well as ungrounded ship loads as shown in figure 7.1. These modules are coupled to the ship's hull through filters and the cables' capacitance.

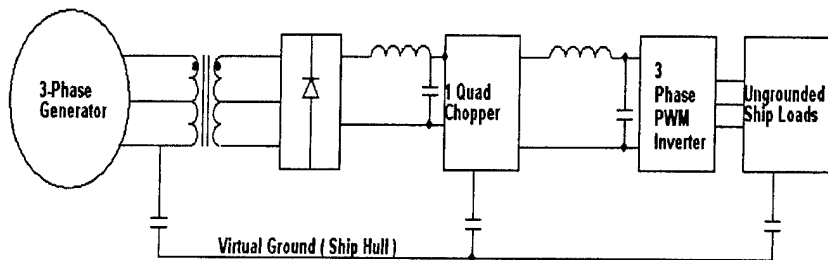


Figure 7.1. A typical integrated power system

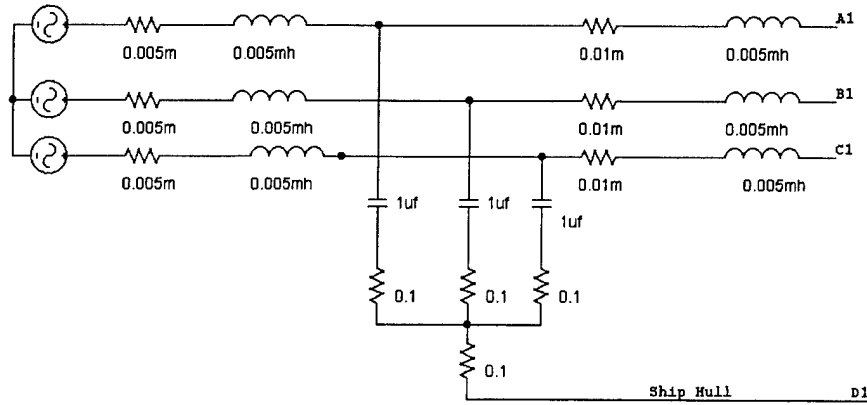


Figure 7.2. Generator and transformer of the IPS

The system is fed by generation rated at 4160V, 3phase 60Hz with capacities ranging from 3.75MW to 21MW. The voltage is stepped down to 430V ac using the transformer modeled in figure 7.2. The transformer is coupled to the ship's hull or ground via a series resistance and capacitance. The transformer's output is connected to a three phase bridge rectifier. This is connected to the smoothing capacitor via the line impedance. The rectified DC voltage across the smoothing capacitor is 1000V. This rectification module module is also capacitively coupled to the ship's hull as shown in figure 7.3.

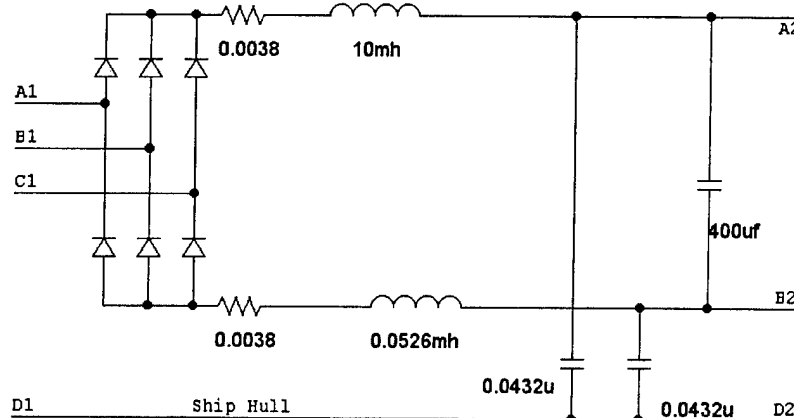


Figure 7.3. The rectifier, line impedance and filter

The 1000V DC voltage is then stepped down to 800V DC by means of the one quadrant chopper shown in figure 7.4. The switching frequency of the chopper is 4kHz with a duty ratio of 0.8 .

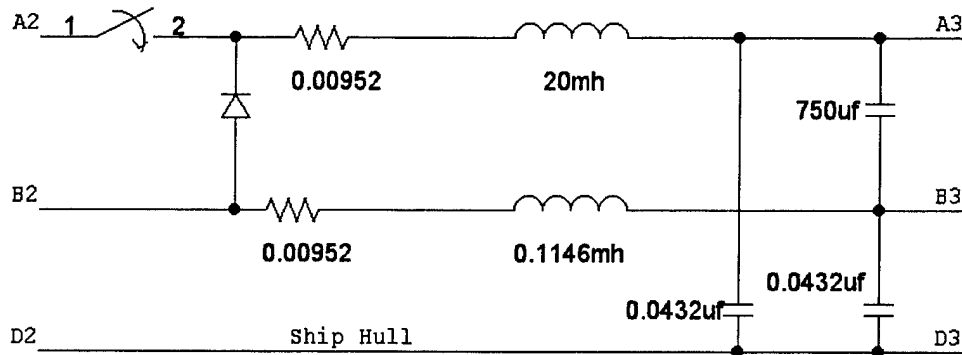


Figure 7.4. The One quadrant chopper

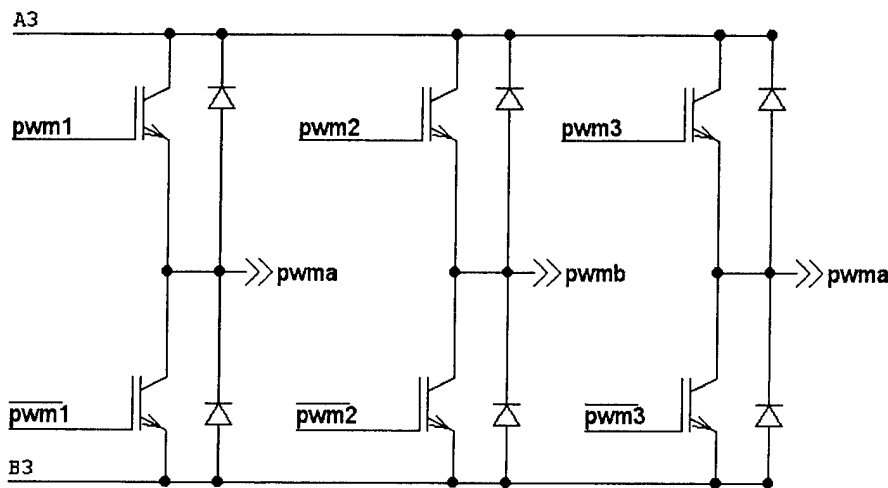


Figure 7.7. The three phase Inverter

The 800V dc link voltage is converted into a three phase PWM waveform using the three phase inverter shown in figure 7.7. The PWM waveform is generated using sinusoidal PWM with a modulation index of 1. The switching frequency is 4.5 KHz and a frequency modulation index of 75 is utilized.

Figure 7.6 shows the line impedance, PWM filters and balanced three phase loads. The filtered output voltages are coupled to the ship's hull through the EMI filters. A single line to ground fault between Phase C and the ships hull is indicated by the dashed line.

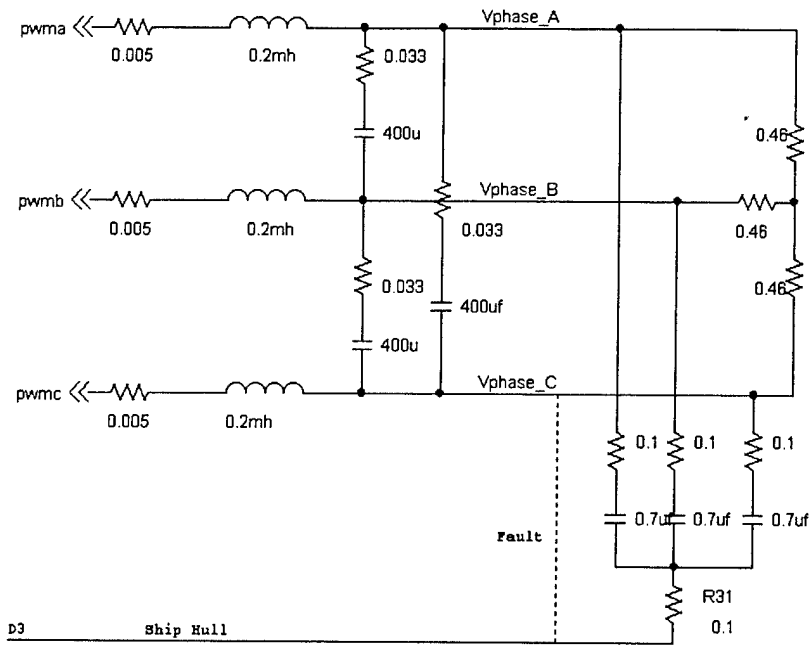


Figure 7. 6. The line impedance, PWM filters and ship loads

7.3 The Detection Algorithm

7.3.1 Single Phase to ground faults

It is desired to be able to detect a line to ground fault by analysing the output line to line voltages. Figure 7.7 shows the line to line voltages for an unfaulted condition. Figure 7.8 shows the three line to line voltages with a 100ms fault on phase A which occurs between 0.32 and 0.42 seconds. By comparing figures 7.7 and 7.8 it is difficult to detect if a fault has occurred as well as which phase is faulted.

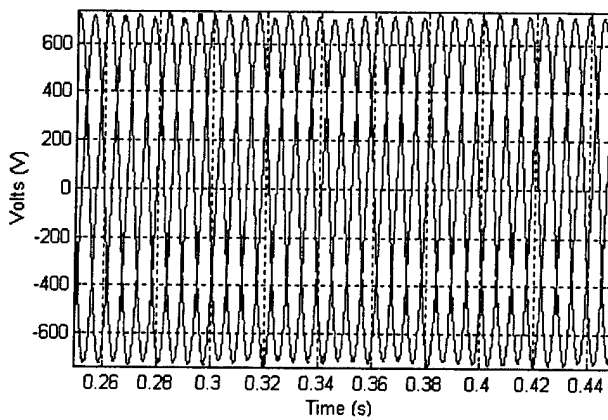


Figure 7.7. The unfaulted line to line voltages

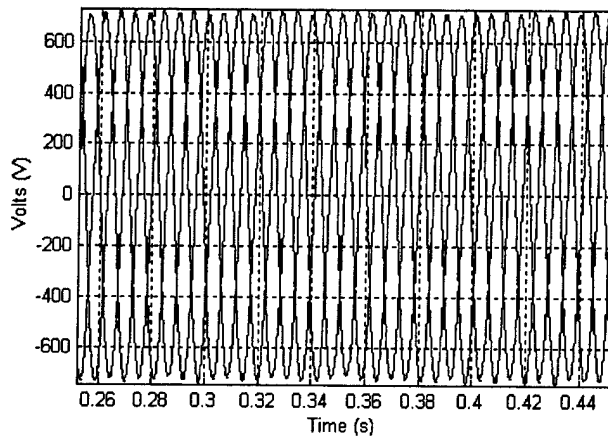


Figure 7.8. The output line to line voltages with a fault on phase A

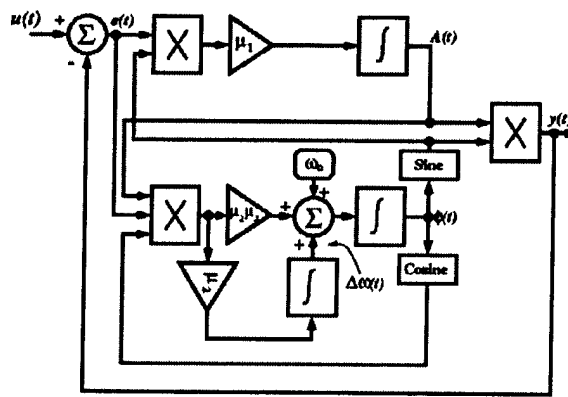


Figure 7.9. Block diagram implementation of the fundamental extraction algorithm [7.16].

It has been found that changes in the high frequency content of the line to line voltages occur when a fault is present. It is therefore desirable to remove the lower frequency fundamental component. The fundamental is extracted using the adaptive notch filter shown in figure 7.9. This filter has been selected to remove the fundamental frequency because it is a zero phase filter. This is advantageous during transient analysis when amplitude, frequency and phase is used to characterize waveforms.

The governing set of equations of this algorithm can be written as

$$\dot{A} = \mu_1 e \sin \phi, \quad (7.1)$$

$$\dot{\omega} = \mu_2 e A \cos \phi, \quad (7.2)$$

$$\dot{\phi} = \mu_3 e \cos \phi + \omega, \quad (7.3)$$

$$y(t) = A \sin \phi, \quad (7.4)$$

$$e(t) = u(t) - y(t), \quad (7.5)$$

in which $u(t)$ and $y(t)$ are the input and output signals to the algorithm, respectively. State variables A , ϕ and ω directly provide estimates of amplitude, phase and frequency of $u(t)$. Parameters μ_1 , μ_2 and μ_3 are positive numbers which determine the behavior of the algorithm in terms of convergence speed and accuracy [7.16].

After removing the fundamental component of the line to line voltage, the residual waveform containing the high frequency content of the original waveform is shown in figure 7.10. The discrete wavelet transform, using Daubechies 4 wavelet, is used to decompose the residual line to line voltages. The lowest scales of the discrete wavelet transform is shown in figures 7.11-7.19.

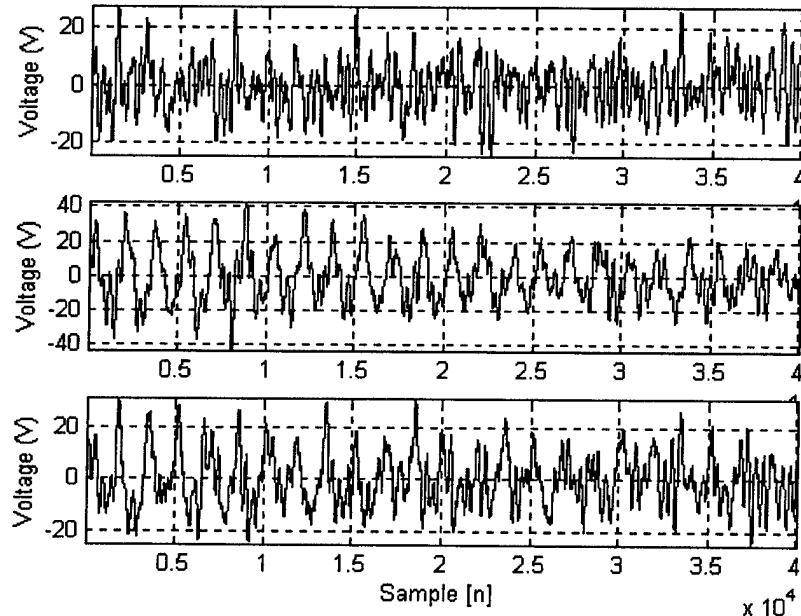


Figure 7.10. The residual line to line voltages after extraction of the fundamental.

7.3.1.1 A single line to ground fault on phase A

A single 100ms line to ground fault is applied to phase A between 0.32 and 0.42 seconds. The resulting wavelet decomposition after filtering is shown in figures 7.11-7.13. Figures 7.11 and 7.13 show similar coefficients throughout the detailed scale levels 1 to 4. These represent the coefficients for line voltages AB and CA respectively. The 3rd and 4th detail levels of these line voltages clearly indicate that a disturbance has occurred.

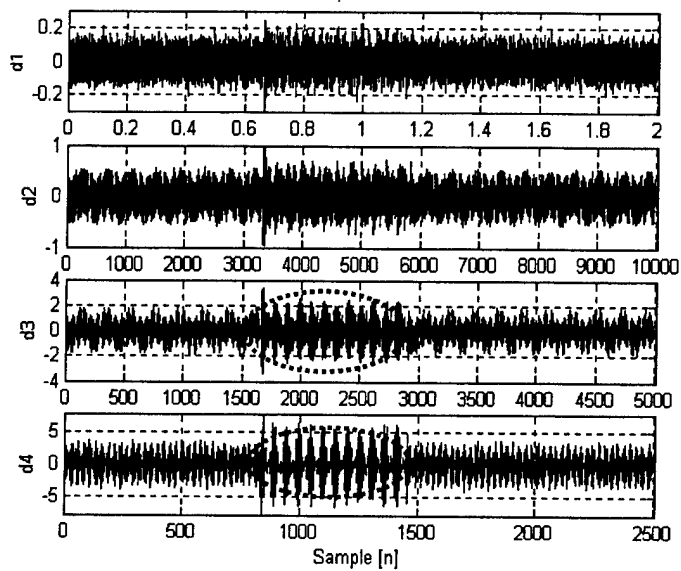


Figure 7.11. Wavelet Decomposition of Phase AB

Figure 7.12, shows that the decomposition of line voltage BC does not have any significant changes in the coefficients during the fault. This fact can be used to unambiguously detect the faulted phase.

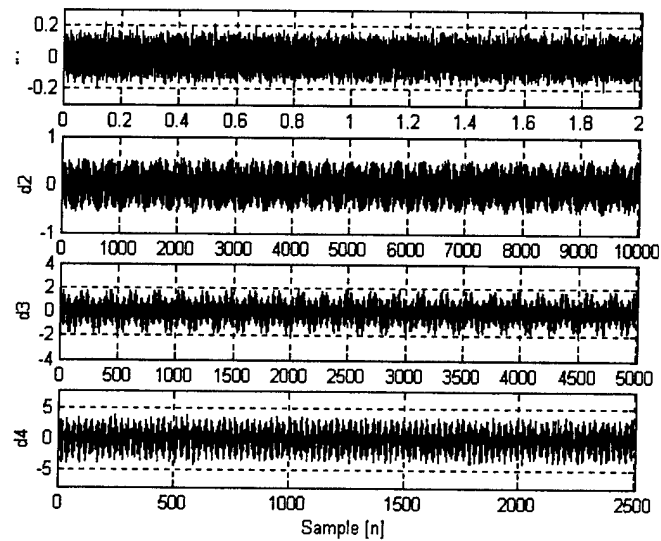


Figure 7.12. Wavelet Decomposition of Phase BC

Figure 7.13 shows the wavelet decomposition of line voltage CA. Similarly to figure 7.11, the presence of a disturbance is detected as shown encircled. The faulted phase can be detected by identifying the line to neutral phase which is common to the two line voltages that show a change in the coefficients during the

fault. Since disturbances only occur in the decompositions of phases AB and CA, the common line to neutral phase is phase A.

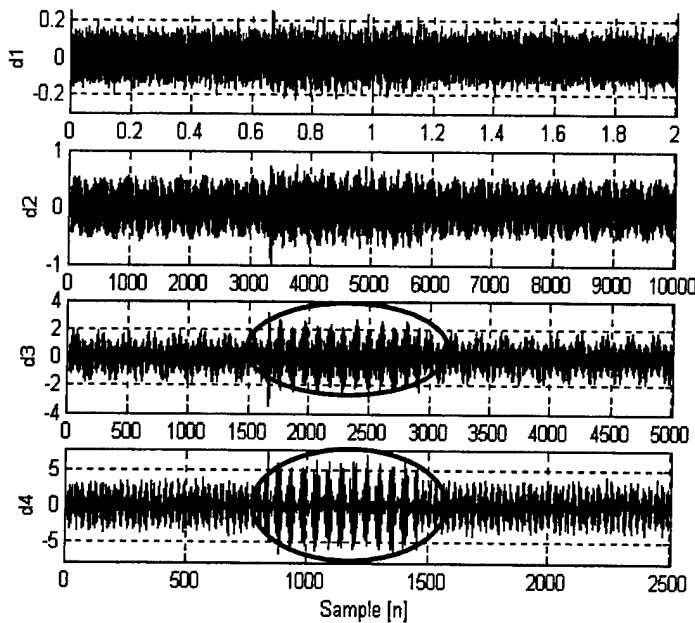


Figure 7.13. Wavelet Decomposition of Phase CA

7.3.1.2 A single line to ground fault on phase B

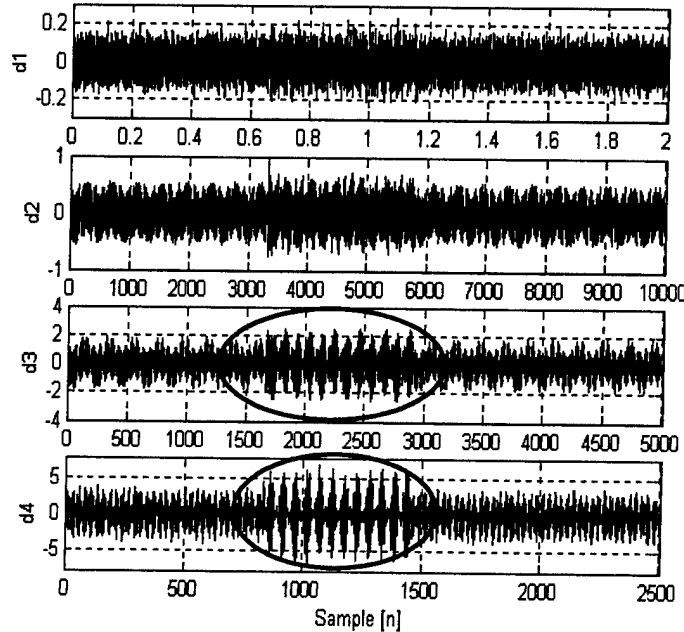


Figure 7.14. Wavelet Decomposition of Phase AB

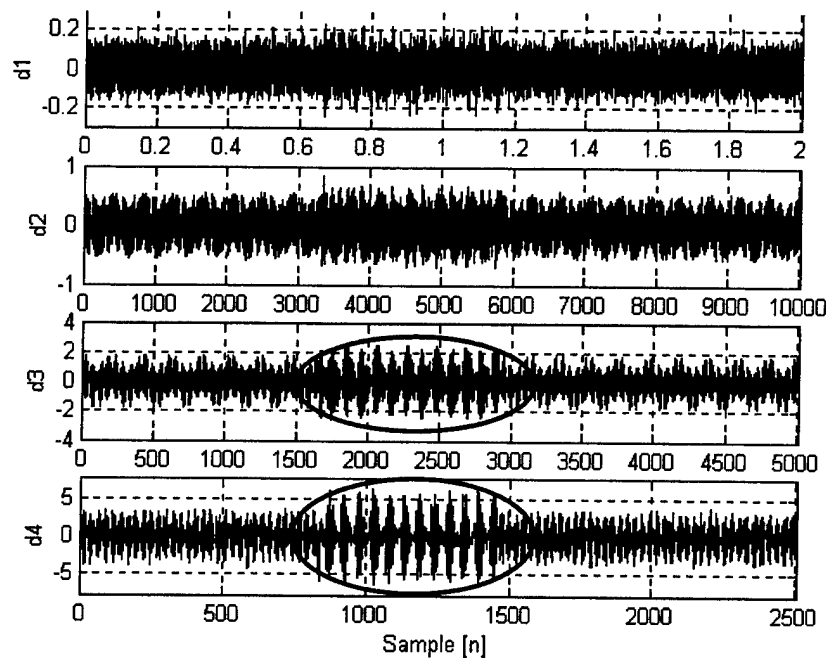


Figure 7.17. Wavelet Decomposition of Phase BC

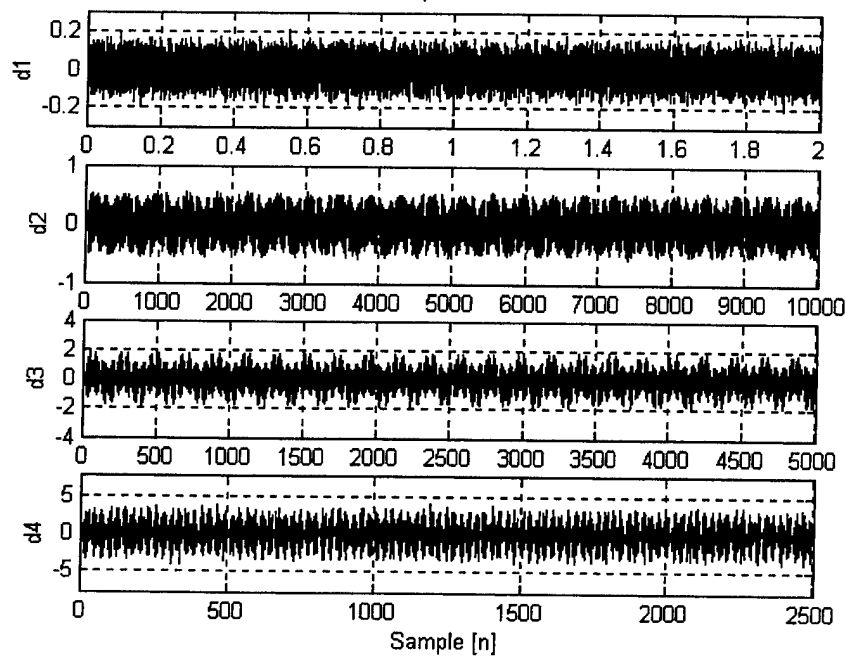


Figure 7.16. Wavelet Decomposition of Phase CA

7.3.1.3 A single line to ground fault on phase C

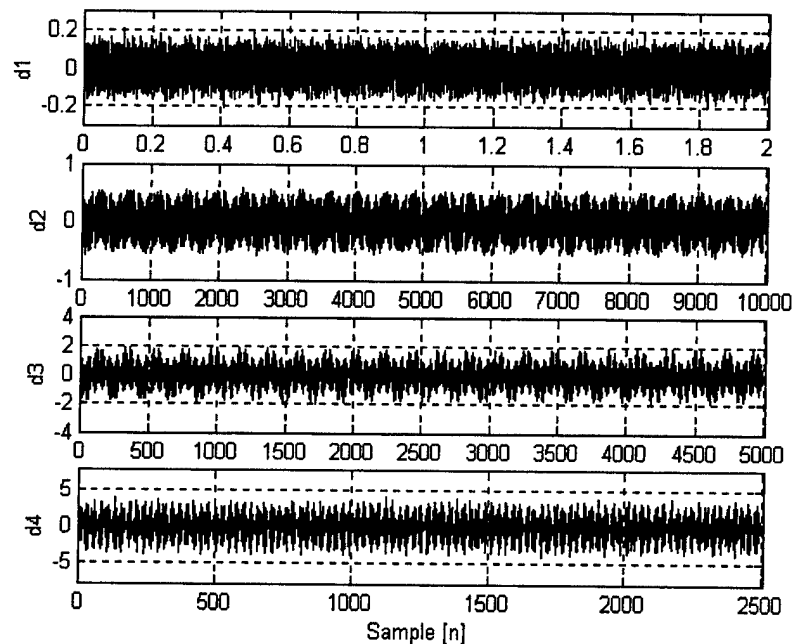


Figure 7.17. Wavelet Decomposition of Phase AB

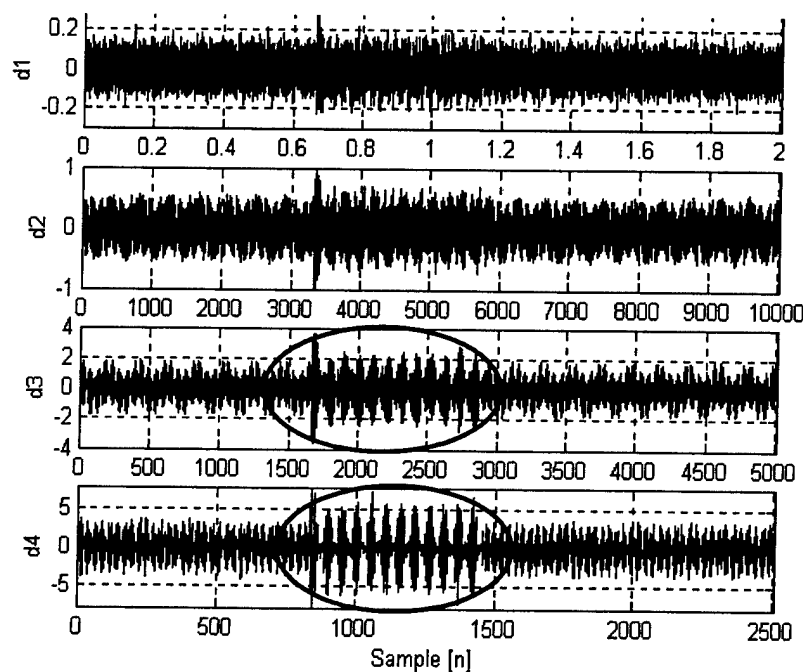


Figure 7.18. Wavelet Decomposition of Phase BC

Table 7.1. Truth table for faulted phase discrimination

Phase AB	Phase BC	Phase CA		Fault on A	Fault on B	Fault on C
0	0	0		U	U	U
0	0	1		U	U	U
0	1	0		U	U	U
0	1	1		U	U	1
1	0	0		U	U	U
1	0	1		1	U	U
1	1	0		U	1	U
1	1	1		U	U	U

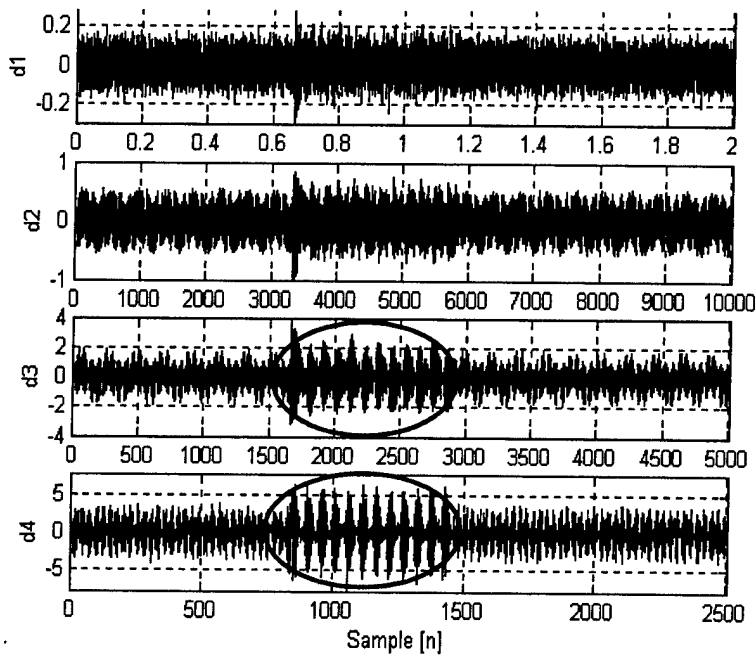


Figure 7.19. Wavelet Decomposition of Phase CA

A distinct trend arises when examining the decompositions of the different faulted conditions. If a fault occurs on phase A then changes can be seen in the wavelet coefficients of line voltages AB and CA but phase BC is unaffected. If a fault occurs on phase B then changes can be seen in the wavelet coefficients of line voltages AB and BC but phase CA is unaffected. Similarly, if a fault occurs on phase C then changes can be seen in the wavelet coefficients of line voltages BC and CA but phase AB is unaffected.

This trend can be used to discriminate between the phases as shown in table 7.1. Changes observed in the coefficients for a phase is represented as a 1 and no change is represented by a 0. The U represents an

unfaulted condition. This logic can be integrated into a fault detection system.

7.3.2 The Detection of Line-Line Faults

A 100ms line to line fault is applied between phases A and B as shown in figure 7.20. In this case there is no need for the algorithm presented here because the detection is done directly using the low frequency line to line voltages. The first four detail levels of the resulting wavelet decomposition are shown in figures 7.21-7.23.

Figure 7.21 shows that the coefficients for line voltage AB are zero during the faulted state for all the detail levels. When observing the decompositions for line voltages BC and CA, it is evident that the coefficients during the faulted state are non-zero. The presence of a line-to-line fault is therefore indicated by zero amplitude coefficients on the faulted phase and non zero coefficients on the other phases. This trend can be used to detect a single line-to-line fault. It does not indicate whether the two lines are faulted to the ship's hull. This fault condition will result in the circuit breakers opening and both lines will be examined. If one line is connected to the ship's hull after the fault has been cleared, it will be detected by the previous detection methodology. A similar trend exists when faults occur between phases B and C, and also between phases C and A.

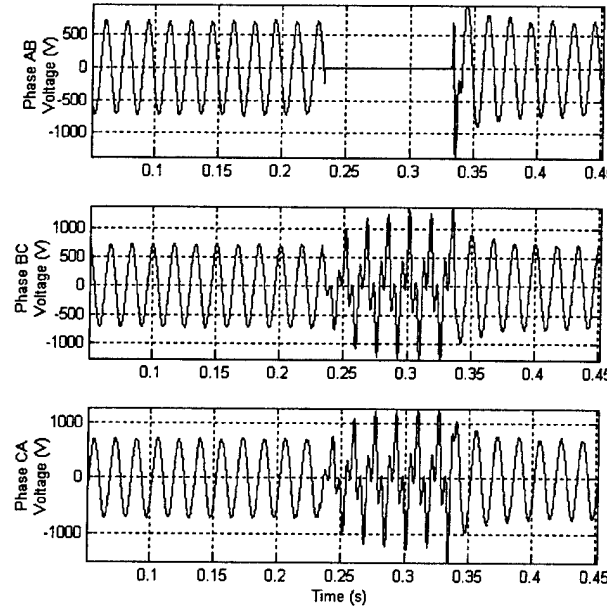


Figure 7.20. The output phase voltages with a 100ms line to line fault between line voltage AB and BC.

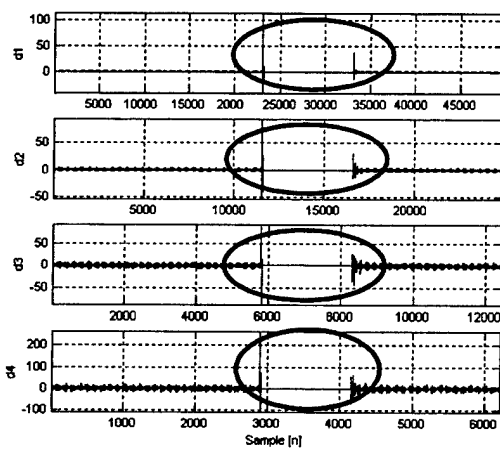


Figure 7.21. Wavelet decomposition for line voltage AB

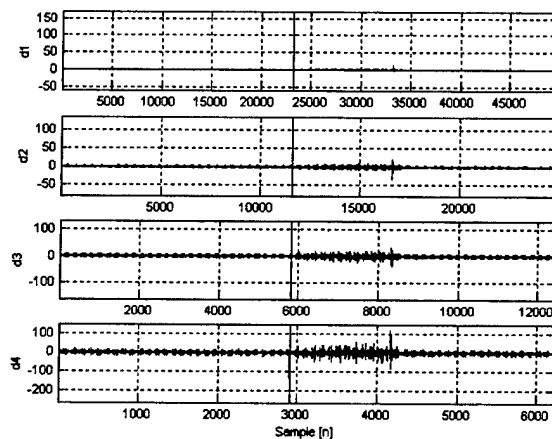


Figure 7.22. Wavelet decomposition for line voltage BC

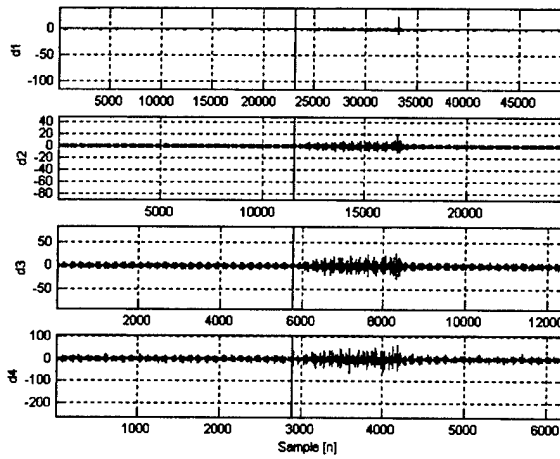


Figure 7.23. Wavelet decomposition for line voltage CA

7.3.3 The Detection of Three Phase Faults

A 100ms three phase fault is applied to the output line to line voltages as shown in figure 7.24. The first four detail levels of the resulting wavelet decomposition are shown in figures 7.25-7.27. By observing the wavelet decompositions of all three phases it is evident that the coefficients are zero during the fault event. This is indicated by the circlements in figures 7.25-7.27.

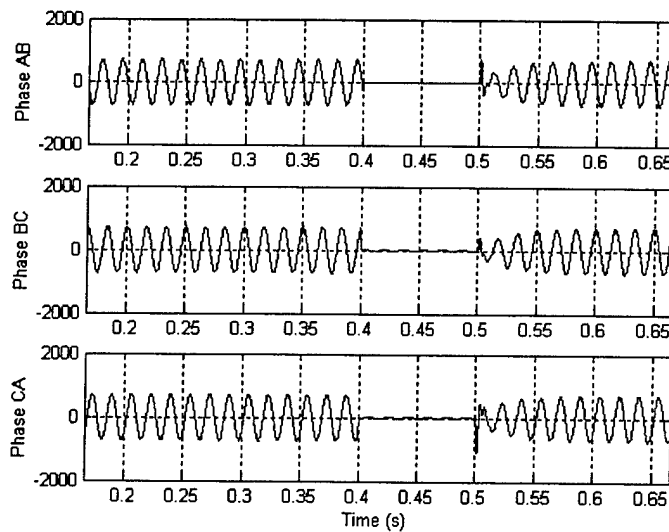


Figure 7.24. The output phase voltages with a 100ms three phase fault.

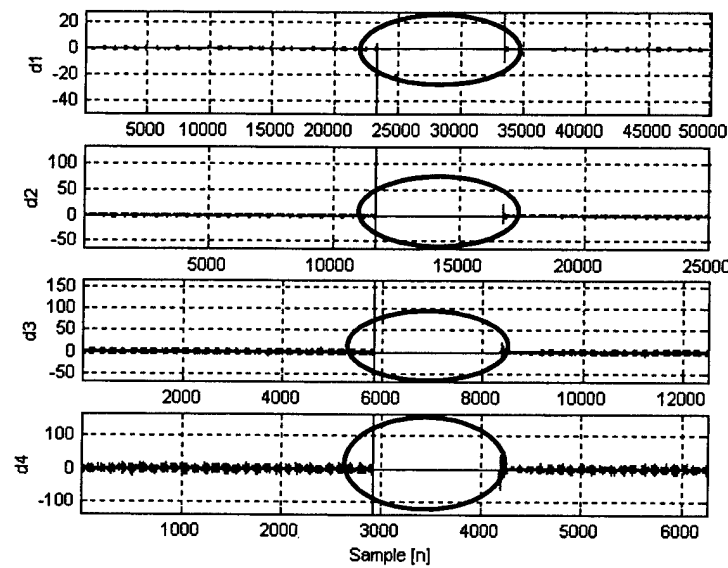


Figure 7.27. Wavelet decomposition for line voltage AB

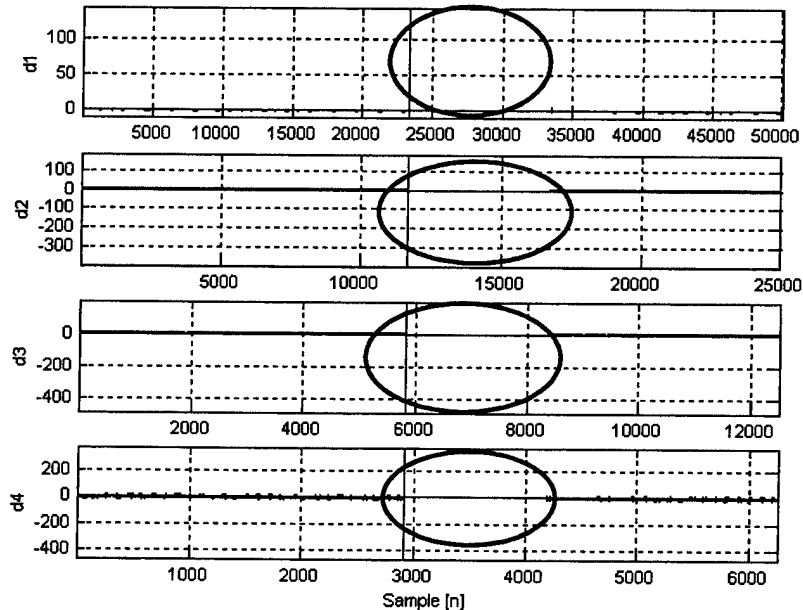


Figure 7.26. Wavelet decomposition for line voltage BC

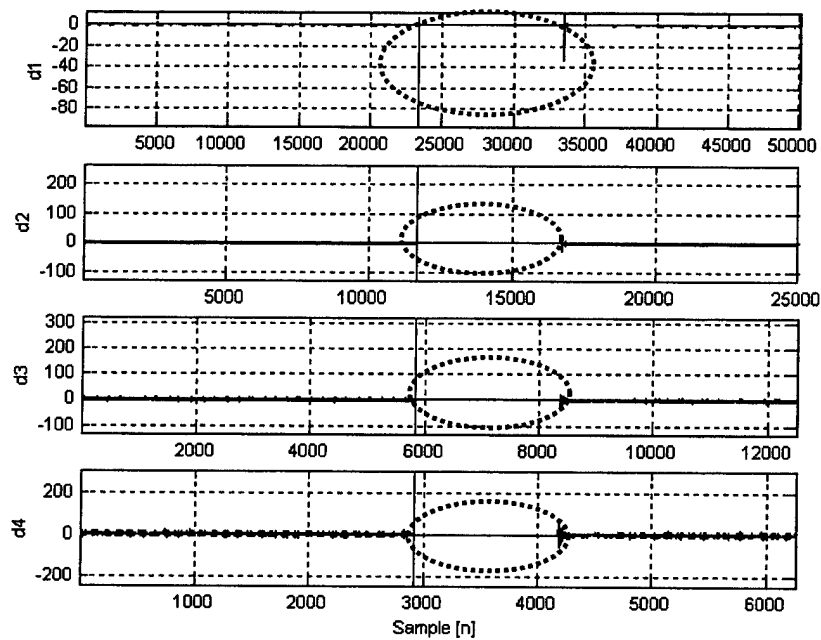


Figure 7.27. Wavelet decomposition for line voltage BC

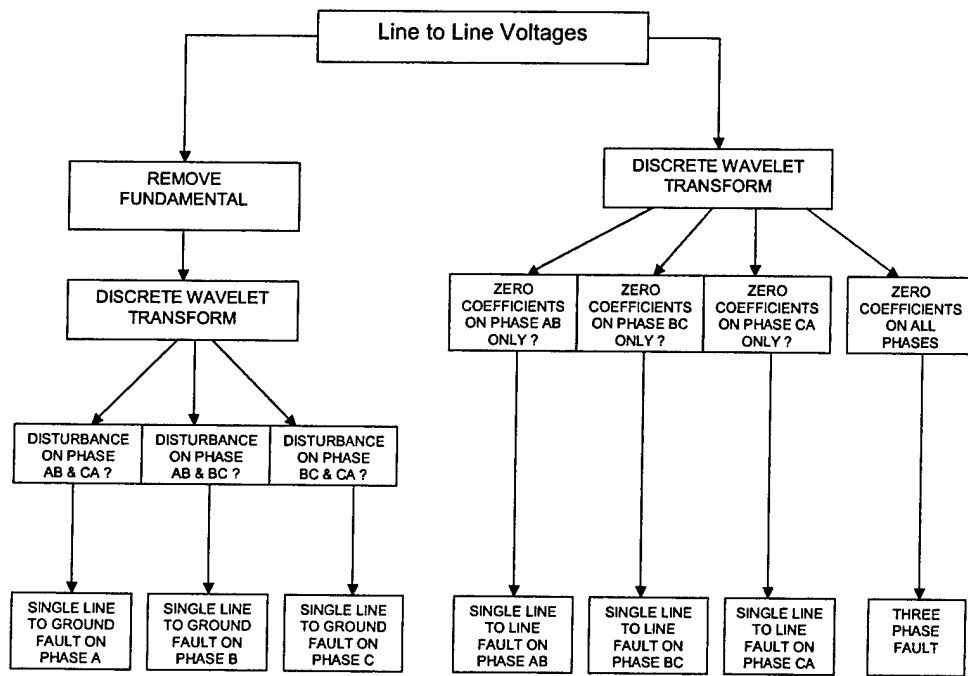


Figure 7.28. Flowchart for fault classification.

Figure 7.28 shows a fault classification flowchart that summarizes the methods used to detect line to ground faults, line to line faults and three phase faults. While the line-line and three phase faults are easy to detect, the contribution here is the fault detection of the line to ground faults in an ungrounded system.

7.4 Conclusions

In this chapter the discrete wavelet transform is applied to the shipboard Integrated Power System for the detection of faults in an ungrounded system. An algorithm for the extraction of the sine wave is used. A method of fault discrimination that determines the faulted phase is presented and applied to the identification of all three single line to ground fault scenarios. A method for detecting both line to line and three phase faults is presented and the results indicate that this detection algorithm can be used in future fault detection systems.

References

- [7.1] Norbert Doerry, James C Davis, : Integrated Power System for Marine Applications," Naval Engineers Journal, May 1994, pp. 77-90.
- [7.2] Norbert Doerry, Henry Robey, John Amy and Chester Petry, "Power the Future with the Integrated Power System," Naval Engineers Journal, May 1996, pp.267-282.
- [7.3] Woodyard, Doug, "Electric propulsion Charges Ahead," Marine Propulsion Journal, April 1995,pp. 29-30.
- [7.4] J Lewis Blackburn, "Protective Relaying: Principles and Applications," Marcel ad Dekker, Inc, New York, 1987
- [7.5] Petry, Chester R, and Jay W. Rumberg, "Zonal Electrical Distribution Systems: An Affordable Architecture for the future," Naval Engineers Journal, V. 105, n 3, May1993, pp45-51.
- [7.6] O. Rioul and M. Vetterli, "Wavelet and Signal Processing" IEEE SP Magazine, October 1991, PP.14-38
- [7.7] S. G. Mallat, "A Wavelet Tour of Signal Processing", Academic Press, 1998.
- [7.8] Gilbert G. Walter, "Wavelets and Other Orthogonal Systems With Applications," CRC Press, 1994.
- [7.9] Yves Meyer, "Wavelets and Operators," Cambridge University Press, 1992.
- [7.10] Yves Meyer, "Wavelets: Algorithms and Applications," Society for Industrial and Applied Mathematics, 1993.
- [7.11] S. Santoso, E. J. Powers, W. M. Grady, and P. Hofmann, "Power quality assessment via wavelet transform analysis," IEEE Trans. on Power Delivery, vol. 11, no. 2, pp. 924-930, Apr. 1996.

- [7.12] P. Pillay and A. Bhattacharjee, "Application of wavelets to model short-term power system disturbances," *IEEE Trans. on Power System*, vol. 11, no. 4, pp. 2031–2037, Nov. 1996.
- [7.13] D. C. Robertson, O. I. Camps, J. S. Mayer, and W. B. Gish, "Wavelets and electromagnetic power system transients," *IEEE Trans. on Power Delivery*, vol. 11, no. 2, pp. 1050–1057, Apr. 1996.
- [7.14] G. T. Heydt and A. W. Galli, "Transient power quality problems analyzed using wavelets," *IEEE Trans. on Power Delivery*, vol. 12, no. 2, pp. 908–915, Apr. 1997.
- [7.15] W. A. Wilkinson and M. D. Cox, "Discrete wavelet analysis of power system transients," *IEEE Trans. on Power System*, vol. 11, no. 4, pp. 2038–2044, Nov. 1996.
- [7.16] Ziarani, A.K.; Konrad, A." A nonlinear adaptive method of elimination of power line interference in ECG signals" *IEEE Transactions on Biomedical Engineering*, Volume: 49, Issue: 6, June 2002

Chapter 8

Investigation of Partial Discharge in Motor Windings

8.1 Introduction

This research evolved into studying the effects of Adjustable Speed Drives, or ASDs, on random wound induction motors. The work is specifically focused on partial discharge type detection. Partial discharge (PD) refers to the small electrical discharges generally found within insulating materials when voltage is applied. PD can also occur on conductor surfaces in free air or other insulating gasses. Of concern for this research is detecting PD within the windings of a common random wound induction motor. These motors are routinely used in industry and are generally the type paired with ASDs. The reason why PD is of concern is because the presence of partial discharges within insulating materials leads to degradation of those materials over time and eventually to motor failure. The usual mechanism for this is actually two fold. First the discharges themselves tend to decompose the insulating material. Decomposition products of typical polymer insulating coatings include short chain hydrocarbons and free carbon. The deposition of carbon over time can cause short circuits between turns, windings, or even to grounded components, ultimately failing the motor. Secondly partial discharges will ionize surrounding gases. For air-cooled machines, oxygen will form ozone, which itself is reactive with the insulation and other motor components, causing further degradation and failure. PD has been studied in detail and many of the causes are well known. Problems can lie in both design and choice of material. Fabrication problems can also arise. Many times when an insulating material is applied to a conductor small voids from the application process are present. Differences in permittivity cause raised voltage stresses to appear across the voids within the material. The electric strength of the gas in the void is significantly less than that of the solid insulation and so a discharge process begins. The shape and size of the voids has a significant effect on the partial discharge inception voltage, discharge severity, and discharge frequency. These voids are also a larger problem within AC systems than DC systems. The reason is that the small voids are capacitively coupled, discharging one or more times per cycle. The DC systems lack this form of cycling and so the voids charge resistively through the insulator, which is extremely slow. Extraneous causes of PD can also be present. Generally these external causes are related to ASDs in some way. If the motor is operating from a sine wave supply directly from the grid, small line transients or overvoltages can cause PD within the motor. These however are of lesser concern because they are short in duration and cause little or no damage to the motor. Alternatively, if large transients reach the motor breakdown can occur directly causing local damage. PD is usually only a factor when it is sustained over long periods of time, continually degrading the system and its components.

8.2 Speed Control

Before ASDs were available there were few ways to adjust the speed of an induction motor. Normally these methods would include altering the resistance of the rotor or possibly the number of stator poles. These methods work but have many disadvantages. The rotor resistance method requires slip rings and caused poor efficiency. The stator pole method requires complicated switching and provides a rather poor speed range adjustment. A new method was introduced with the advent of modern solid-state switches. These switches are used to essentially alter the synchronous frequency of the supply. Generally the sine supply is first converted to DC through various rectifying methods. The DC supply is then switched to create an adjustable frequency AC supply. The switching schemes can vary but Pulse Width Modulation is commonly used. These systems produce a voltage waveform that changes extremely quickly from one DC value to another. However, since the motor is highly inductive, the current waveform is an integration of the voltage waveform or an approximate sine wave of variable frequency.

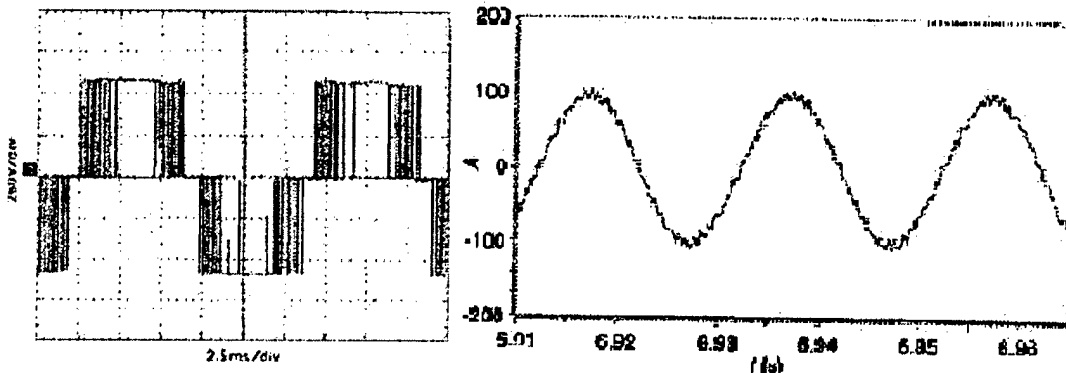


Fig 8.1. Line-to-Line Voltage supplied by PWM Drive During Two Wave Periods

When such a wave is fed to the motor it will then have an adjustable speed. These drive systems have the advantages of being both easy and flexible to implement as well as being efficient. Unfortunately these drives also have some drawbacks, some of which concern PD.

Fig 8.2. Primary Current $I(t)$ Time Waveshape

8.3 External Causes of PD

There are some conditions that can exacerbate PD that are not related to motor design or construction. One such cause appears when an ASD is connected to the motor with long feeder cables. Because the ASD produces a voltage waveform that quickly transitions from one voltage extreme to another, large voltage overshoots can be created at the motor terminals. This is caused by impedance mismatches between the motor and the feeder cables. A steep fronted wave, similar to the ASD waveform, travels down the feeder cable that now acts as a transmission line. Once the wave reaches the end of the cable and the beginning of

the motor terminals it experiences an impedance mismatch, which causes the wave to be reflected. This reflection can cause the voltage wave to double or in some conditions be even larger. The motor now experiences an extremely large voltage across the terminals and overstressing the windings.

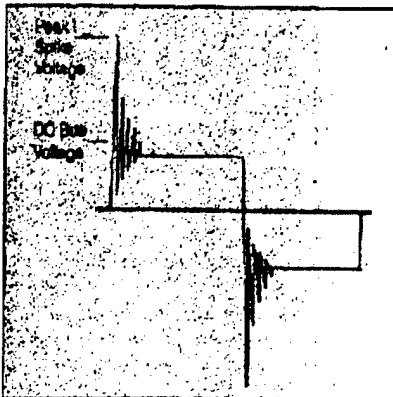


Fig 8.3. Over-Voltage at Motor Terminals

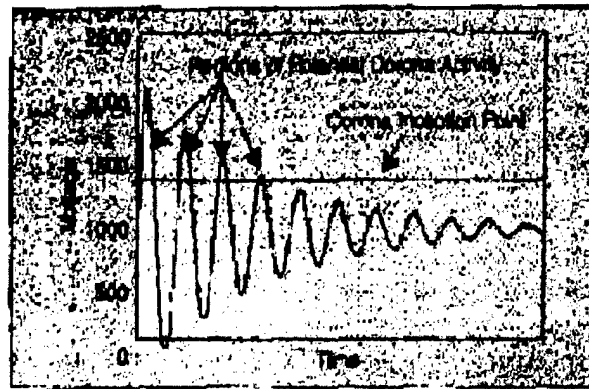


Fig 8.4 Voltage Spike Generating Corona

This problem is more complex than it appears. The impedance mismatch is not directly at the terminals of the motor as is predicted by a simple lumped parameter model. In fact the impedance changes as the wave travels deeper into the motor. As the motor is a relatively large inductor, steep fronted waveforms penetrate only a short distance into the windings. This causes much of the voltage to be dropped across the first few turns of each winding.

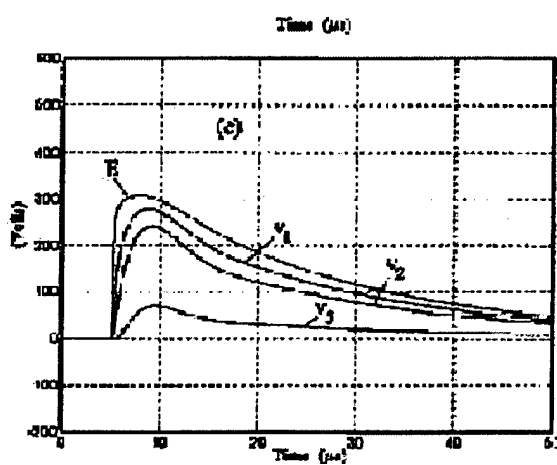


Fig 8.5. Voltage Drop Across the First Three Turns Due to Applied Voltage Waveform E

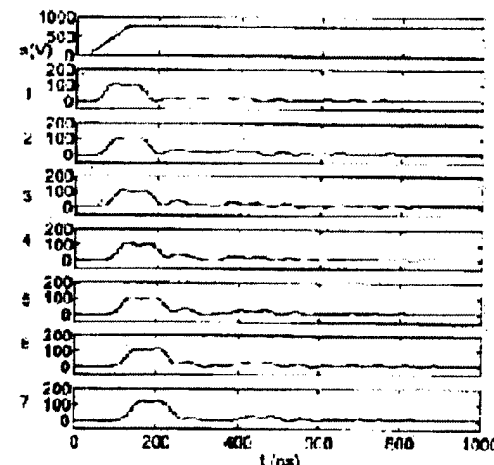


Fig 8.6. Turn-to-Turn Voltage Distribution (100ns Rise Time)

Steep fronted waves can cause the insulation to discharge or possibly even fail at the end of the motor winding. To counter this problem motor manufacturers now make an inverter duty class of some common motors. These motors include thicker insulation on either the first few turns or sometimes on the entire windings of the motor. This helps to compensate for the larger than rated values that appear due to the ASDs. But, unfortunately, even with an inverter duty motor PD may still be present and can lead to drive failure. It would be useful to detect the existence of PD within the motor and take corrective actions before the motor sustains permanent damage. In fact it would be even more useful if the motor could be tested while online instead of removal and testing as required with some methods of gauging insulation degradation.

8.4 Detecting Partial Discharge Signals

A partial discharge signal waveform is a rather small steep fronted pulse that generally occurs randomly in time and only if the voltage stress is above the partial discharge inception voltage. These small PD pulses are very similar in shape to the ASD voltage pulses but several orders of magnitude smaller in amplitude. This makes detecting PD within an online motor extremely difficult. The research discussed here has focused on this problem, with a need to develop a method of detecting the PD while rejecting the ASD pulses that drives the motor.

8.5 Conventional Partial Discharge Quantification

Initial tests were performed to determine the characteristics of some common PD pulses. For this work a conventional 60Hz sine wave PD detection system was used. Basic information about the PD pulses was gathered using this approach. RMS values for PD inception voltage were obtained, which provided an estimate of the inception voltage that should be expected for the ASD cases. Secondly the size of discharges was measured and to provide a target sensitivity for a detection method for ASD operation. An attempt was made to observe the wave shape using a PC with a high-speed analog to digital card. The intent was to match this characteristic waveform to those of the ASD partial discharge. This technique proved less usable because the output of the partial discharge detector produced an integration of the PD voltage pulse. This method resulted in a loss of information as it gave a measure of charge instead of an accurate representation of the voltage waveform itself.

8.6 Preliminary Measuring Circuit

A method was developed that enabled the PD waveform to be viewed. For this a filter with a vacuum tube amplifier circuit was devised. Upon consideration it was decided that PD would most likely be detectable from a phase winding to a grounded surface within the motor. This approach was similar to the functioning of a conventional sine wave PD detector. The motor ground was floated and the filter circuit was connected between the case and ground. The filter circuit allowed the low frequency sine components

to pass to ground, while the high frequency components were passed to the amplifier. A vacuum tube amplifier was chosen for two reasons. Firstly, the tube amplifier provided good protection as a buffer for the data acquisition equipment. Should the motor insulation fail under the high stress of the PD detection test it could short and place that large voltage on the equipment. Secondly the tube amplifier offered a high impedance and high gain needed to detect the small PD pulses. Although this method worked well to collect the wave shape of the PD pulses, there were some impracticalities associated with the circuit configuration. It would be extremely difficult to electrically isolate the motor case in a normal field application. There was also the concern that because the motor case was not solidly grounded the wave shape of the PD may have been altered by stray capacitance. While suitable for the AC case, this method was not applicable for use with ASD type waveforms because of their high frequency components. This method, however, did provide a starting point, and enabled the gathering of small signal waveforms for the motor environment.

8.7 Differential Measurements

The next approach was to devise a method to separate the PD pulses from the ASD pulses. First windowing of the data acquisition samples was considered so that they ignored the ASD pulses. Unfortunately this would limit the data because PD would most likely occur at the beginning of the ASD pulses where the voltage overshoot would be greatest. It was decided to make comparative measurements using different windings in the machine, to enable rejection of the ASD pulses. Many low voltage motors are dual wound to accept either 230V or 460V. This type of construction makes one of the motor star points accessible for outside connection. The motor was opened and a connection was made to the other winding star point. With access to both star points differential measurements could be made between them. The concept of the differential measurement was based on both windings having the same number of turns and therefore comparable characteristics for transient parameters. The ASD waveforms would travel through the separate windings in a similar manner, and therefore appear at the starpoints such that they would cancel one another in a differential measurement. Conversely, a PD pulse appearing in a winding would appear across the differential connections. This is based on the fact that PD occurs randomly in time and location and therefore would not occur in both motor windings simultaneously.

There were, however, some difficulties in measuring signals at the starpoints. Normally if the motor is fed from a normal three phase sine wave supply the star points can be expected to be at ground potential or at least close to it. This would allow a high-sensitivity differential probe to be used. This, however, does not hold for a motor driven by an ASD. When an ASD is driving the motor the starpoints are not at ground potential for a large portion of the operation. Instead, because of the ASD waveform, the starpoints can swing in potential to approx 2/3 of the DC link voltage, which represents a significant common voltage value. For this type of measurement a differential probe is needed that is capable of high-resolution measurements coupled with the ability to tolerate a high voltage level offset. Usually this is opposite of

what is available. If a probe can function at high voltages then it is usually low resolution and vice versa. The probe also is required to measure at high frequencies in order to capture the fast PD pulses. A circuit was developed that had to satisfy these characteristics. The circuit front end used a small high frequency transformer placed across the starpoints with an insulation barrier capable of withstanding the high voltages at the starpoint. The coil ratio was selected to be a 1:10 ratio so that the secondary provided voltage amplification of the differential signals. This was then coupled into a differential amplifier with a high common mode rejection. A single ended output was taken from the differential amplifier to supply the data acquisition hardware. Due to the very large ASD amplitude compared with the PD pulse, it was not possible to remove the entire common mode signal, however, this circuit was able to reduce it to a manageable level.

8.8 Data Extraction and Processing

The developed differential amplifier permitted the acquisition of data in sufficient detail to search for PD. The high-speed data acquisition board was capable of sampling at 5GHz. An extensive custom-built GUI was constructed in LabView that was capable of gathering and presenting the data. This oscilloscope emulation system allowed not only viewing in the time domain but was also able to perform FFT (Fast Fourier Transform), STFT (Short Time Fourier Transform), an averaged Time, and a Wavelet Transform. When the data was gathered it became clear that detecting the PD would take some digital signal processing before it would yield consistent results. At first the FFT was used to find differences in the frequency content of signals known to have PD and those known not to have PD. While the FFT provides a perfect frequency representation of the signal, it provides no time representation. The FFT approach, therefore, was unable to distinguish which components belonged to the ASD pulses and which belonged to the PD pulses since their components were so similar. Another approach was taken, using STFT. While this yielded a significant improvement it still was not capable of separating the signals. Finally Wavelets were chosen due to a unique ability to represent high frequencies well in the time domain but also to represent low frequencies well in the frequency domain.

8.9 Wavelet Transform

The wavelet transform was developed in order to overcome the deficiencies within the FFT and the STFT. It provided both time and frequency information about a waveform at the same time. This permitted a determination of which frequencies occurred, and at what time in the wave. For example, when looking for a specific frequency or frequencies of a certain event such as PD, it is possible to separate the components that contain the pertinent signals and remove the background noise and interference. The time waveform can then be reconstructed without the other unwanted components.

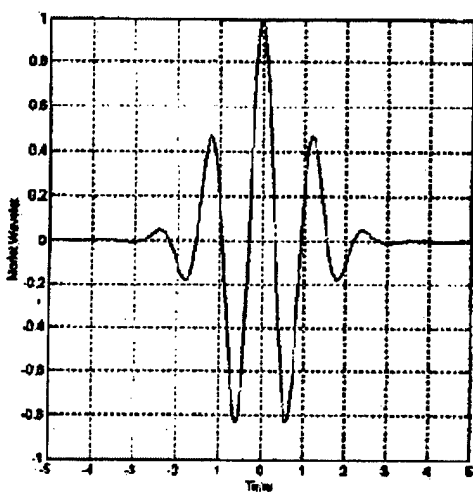


Fig 8.7. Mother Wavelet

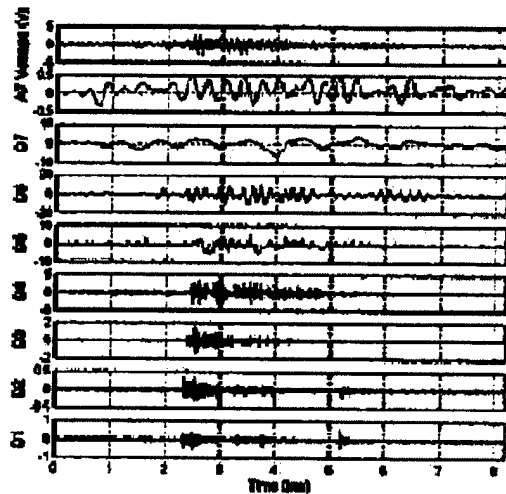


Fig 8.8. Seven Level Wavelet Decomposition

In the wavelet transform a time domain signal is passed through a set of high and low frequency digital filters to separate them into equal spectral ranges. Either of these two signals, but usually only the lower, can be decomposed further to form lower levels of frequency. Usually the lower frequency signals are also down-sampled by two. The Nyquist theorem indicates that there are more samples than needed to completely represent the signal so the redundant data is removed. Once the original waveform has been decomposed to the desired level it is then passed through the wavelet transform. This is a process where the signal is multiplied by a mother wavelet, which is both scaled and translated. The output is a signal that shows how well the scaled and translated mother wavelet matches the base signal. This allows the extraction of signals that are otherwise hidden deep within noise and interference. The caveat is that the mother wavelet must be properly selected. When using wavelets this selection process is of the greatest concern, for if the wavelet is chosen incorrectly the transform will provide little or no information.

8.10 Conclusions

While the analysis in this work is not yet complete there are some general observations that can be made. Using the developed differential circuit measurement method coupled with the data acquisition and wavelet transform system it is apparent that motor load should have less of an effect on this PD detection system than with conventional methods. This will permit a variety of motors to be evaluated with this technique. From the preliminary results obtained with the motors examined here there appears to be a correlation between pulse width and partial discharge inception voltage. It has been observed that as the drive pulse decreases in width the inception voltage rises significantly. Based on observations in this work it should be possible to determine improved methods of driving motors that avoid the damage caused by long-term partial discharge exposure.

Figures taken from the following sources

- Fig 8.1: Electrical stresses applied to stator insulation in low-voltage induction motors fed by PWM drives. A. Mbaye, J. P. Bellomo, T. Lebey, J. M. Oraison, F. Peltier
- Fig 8.2: Harmonic analysis method for traction drives EMI studies. M. Lordache, C. Marchand, S. Berlin and V. Mickiewicz
- Fig 8.3 and Fig 8.4: Using Corona Inception Voltage for Motor Evaluation. Chris Lanier
- Fig 8.5: Transient Voltage Distribution in Inverter Fed Motor Windings: Experimental Study and Modeling. Pierre Bidan, Thierry Lebey, Gerard Montseny, Claudiu Neacsu, and Jacques Saint-Michel
- Fig 8.6: Analysis of Steep-Fronted Voltage Distribution and Turn Insulation Failure in Inverter-Fed Form-Wound AC Motor. Yifan Tang
- Fig 8.7 and Fig 8.8: Application of Wavelet Analysis to Acoustic Emission Pulses Generated by Partial Discharge. Tomasz Boczar and Dariusz Zmarzly

Chapter 9

Project Overview and Conclusions

9.1 Project Overview

The research project “Power Quality Study for the Proposed Integrated Power System”, ONR no. **N00014-01-1-1028**, has addressed a range of shipboard power quality issues. The research has delivered a number of key results, as detailed in the previous seven chapters. In some cases, the results of this research are ready to move on to product implementation. In other areas of this research, the results are intermediate and further research is needed to bring the results to implementation.

The following list contains information on each key aspects of this research, and an assessment of the current status of this work at this point in time.

Generator Grounding Study The research has proposed a method for operating a pair of direct connected generators. The generators are operated with a high impedance grounding system. The study has shown that a pair of these generators can be operated on shipboard systems with a bus tie circuit breaker, so that the units can be operated either with the breaker opened or closed. Detailed simulations of the ground faults on this system show that a protective function can be implemented which would sense the presence of a ground fault on either of the given generators. We believe that such a system could be designed and successfully built at this time.

Novel electric drive with power-regenerating capability. This study has investigated the development of a variable voltage, variable frequency electric propulsion system for application on shipboard systems. It is our position that the current generation of power converters makes this approach practical. The results of this study show that this proposed approach has the potential to provide an attractive shipboard propulsion

system with reduced space, weight, and cost, plus increased fuel efficiency, as compared to the conventional electric propulsion systems. The study included an analysis of using the drive momentum to regenerate power for a pulse power load. There are indications that this could provide increased pulse load capability over conventional designs. As a result of this research, it would be desirable to conduct scaled tests of this proposed system.

Improved Motor Starting Capability of Three Phase UPS Inverters This study has proposed a method to provide improved motor starting capability for fixed frequency inverters supplying general loads. This is an item of concern throughout the industry as more inverters are being applied in this mode. The proposed work has suggested that the inverter capability can be increased through the judicious introduction of voltage sags during motor starting. This work is at the stage where a prototype should be constructed and tested. If the prototype functions as predicted, the resulting inverter could be turned into a marketable product.

The application of wavelets to the detection of broken rotor bars in induction machines This study has proposed a new algorithm that can be used to detect the presence of broken rotor bars in induction machines that operate under transient conditions. The new methodology is immune to loading effects unlike the classical steady-state condition monitoring algorithms. A wavelet analysis of the starting current of an induction motor is presented and the results show that there are clusters of wavelet coefficients that are only found when analyzing a machine with broken rotor bars. It is envisioned that this study could form the foundation of future condition monitoring techniques of machines that operate predominately in the transient such as motor operated valves, launchers and wind generators.

The Application Of Wavelets to Shipboard Power System Protection. In this study, the discrete wavelet transform is applied to the shipboard Integrated Power System for the detection of transient faults in an ungrounded system. An algorithm for the extraction of the fundamental sine wave is used. A method of fault discrimination that

determines which is the faulted phase is presented and applied to the identification of all three single line to ground fault scenarios. A method for detecting both line to line and three phase faults is presented and the results indicate that this detection algorithm can be used in future fault detection systems.

Measurement of surge propagation in induction machines This study contributes to the measurement of machine parameters used to determine surge propagation. A single coil of the machine is divided into regions of differing impedance namely the slot and the overhang regions. Detailed parameter measurements are made of each turn within each region. This includes turn to ground and turn-to-turn capacitances and self and mutual inductances. These parameters are then used to determine the surge impedance of each section. Bewley lattice theory is extended to track surge propagation within the coil. Boundary voltages located at the impedance mismatch are calculated to determine the magnitude of the overvoltages occurring within each turn of a coil. The results produced by this research will give motor designers an insight into designing machines that are resilient to surges.

Investigation of Partial Discharges in Motor Windings. This research has highlighted the need to examine motors controlled by adjustable speed drives for partial discharges. While partial discharges do not immediately cause breakdown their continued presence degrades the material and failure will ultimately occur. Conventional equipment used to detect such pulses operates under steady state ac conditions. However, when an adjustable speed drive is used a pulse waveform is applied to the motor rather than an ac supply. Under these conditions transient voltages are created throughout the windings. Tests have shown that voltage amplitudes are significantly in excess of the normally expected steady state values. The partial discharges that result are in a noisy electrical environment and are impossible to detect with conventional equipment. Using the probing techniques and algorithms presented in this work it has been shown that these pulses can be detected. This approach permits a quantification of partial discharge activity and hence a means of assessing motor life under the pulse conditions presented by adjustable speed drives.

9.2 Conclusions

This document is the final report for the research project “Power Quality Study for the Proposed Integrated Power System.” This research has led to a number of important results, as described in the previous chapters and summarized in Section 9.1. Several of these results are ready to be moved to the development or prototype stage, while others need further research to demonstrate their viability. The continued development of these research thrusts will provide improved power quality to both shipboard systems and power systems in general.